

## **INFORMATION TO USERS**

This manuscript has been reproduced from the microfilm master. UMI films the text directly from the original or copy submitted. Thus, some thesis and dissertation copies are in typewriter face, while others may be from any type of computer printer.

**The quality of this reproduction is dependent upon the quality of the copy submitted.** Broken or indistinct print, colored or poor quality illustrations and photographs, print bleedthrough, substandard margins, and improper alignment can adversely affect reproduction.

In the unlikely event that the author did not send UMI a complete manuscript and there are missing pages, these will be noted. Also, if unauthorized copyright material had to be removed, a note will indicate the deletion.

Oversize materials (e.g., maps, drawings, charts) are reproduced by sectioning the original, beginning at the upper left-hand corner and continuing from left to right in equal sections with small overlaps. Each original is also photographed in one exposure and is included in reduced form at the back of the book.

Photographs included in the original manuscript have been reproduced xerographically in this copy. Higher quality 6" x 9" black and white photographic prints are available for any photographs or illustrations appearing in this copy for an additional charge. Contact UMI directly to order.

# **UMI**

A Bell & Howell Information Company  
300 North Zeeb Road, Ann Arbor MI 48106-1346 USA  
313/761-4700 800/521-0600



**PROJECTOR AUGMENTED WAVE METHOD  
CALCULATION OF  $G_A$  ADATOM DIFFUSION  
AND LOCAL DENSITY OF STATES  
FOR  $G_{AA}$ s AND  $Si$  SURFACES**

**DISSERTATION**

**Presented in Partial Fulfillment of the Requirements for  
the Degree Doctor of Philosophy in the Graduate  
School of The Ohio State University**

by

**Jeffrey Guy LePage, B.S., M.S.**

\* \* \* \* \*

**The Ohio State University**

**1997**

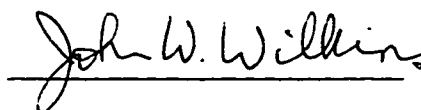
Dissertation Committee:

John W. Wilkins, Adviser

Charles A. Ebner

Jonathon Pelz

Approved by

A handwritten signature in cursive script that reads "John W. Wilkins". The signature is written in black ink and is positioned above a horizontal line.

Adviser

Department of Physics

**UMI Number: 9721126**

---

**UMI Microform 9721126**  
**Copyright 1997, by UMI Company. All rights reserved.**

**This microform edition is protected against unauthorized  
copying under Title 17, United States Code.**

---

**UMI**  
**300 North Zeeb Road**  
**Ann Arbor, MI 48103**

© Jeffrey Guy LePage 1997

**ALL RIGHTS RESERVED**

## ABSTRACT

We have investigated the properties of several surface systems using the newly formulated Projector Augmented Wave (PAW) method. The ground state geometries of the GaAs(100)-c(4x4), GaAs(100)-c(2x2), and Si(001)-(2x1) surfaces are determined using this method and are found to agree well with experiment and previous calculations. For the GaAs(100)-c(4x4) surface, the total energy surface for a lone Ga adatom propagating along the surface is calculated. Based on this data we have identified three relatively stable adsorption sites. In order of increasing energy these sites are (I) the center of the missing dimer position, (II) between the dimer rows and adjacent to a center dimer, and (III) between the dimer rows, adjacent to an edge dimer. The surface diffusion activation energies have also been identified; the smallest activation energy is 0.14 eV while the largest is 0.46 eV. Monte Carlo simulations incorporating these data indicate that diffusion on this surface is essentially isotropic. This isotropy is due to the effect of a deep well at site I, which effectively controls diffusion in both the x- and y-directions. PAW-based calculations of the local density of states (LDOS) for a Si(001)-(2x1) surface are also presented. The up and down atoms of the buckled dimer are plainly evident in the LDOS curves. Finally, the results of the first ever PAW based calculation of optical properties is presented for bulk GaAs and Si. Agreement with experiment is good, and the f-sum rule is satisfied to within a few percent.

Thương tặng Yến Vân, người vợ yêu giầu của tôi

## ACKNOWLEDGMENTS

I wish to thank ...

...My wife for putting up with me during three years of graduate school.

...My parents for putting up with me my whole life.

...Tessa, Riker, Spock, and Dax for just being there and only occasionally piddling on the carpet.

...John Wilkins for his good advice and occasional bursts of abuse.

...Meb Alouani for introducing me to augmentation methods, LMTO, Peter Blöchl and for devoting enormous amounts of time and effort to my thesis.

...Peter Blöchl for inventing PAW and making his program available to me.

...Zürich for a great three weeks.

...Elizabeth Steiner for showing me Zürich by night.

...The United States Air Force for having cool names for their employment programs.

...Don Dorsey for giving me an incredibly difficult thesis topic.

...Pat Hemenger for hiring me.

...Sven Rudin for numerous discussions about physics, coffee, Switzerland, and more physics.

...Carlos Egues Menezes for numerous discussions about physics, coffee, Brazil, and more physics.

...Jian Chen for numerous discussions about physics, China, LAPW, pseudopotentials, and even more physics.

...Jeongnim Kim for being the only surface theorist in my group.



...Wil Aulbur for numerous discussions about physics, Germany, religion, cross-cultural marriages, GW, and even more physics.

...Avik Ghosh for cutting the cake so well.

...Matthew Steiner for numerous discussions about physics, Switzerland, and even more physics.

...Shiwei Zhang for numerous discussions about physics, and occasionally coffee.

...Lars Jönsson for numerous discussions about physics and for having contacts in Sweden.

...Anders Barany, Petras Kundrotas, Mats Jonsson, and Göran Grimvall for helping me out in a time of need despite the fact that they had no idea who I was.

...Michael Reyzer for numerous discussions about physics, for always bringing the vodka, and for being a real pain during my very first talk at OSU.

...Alex Kuznetsov for numerous discussions about physics.

...Herve Castella for numerous discussions about physics.

...Zachary Levine for numerous discussions about physics and for suggesting OSU to me.

...Richard Boyd for getting me through my General Exam despite numerous paperwork errors on my part.

...Sylvia McDorman for knowing everything about the group.

... Shelley Palmer for learning, in a very short time, everything about the group.

... Charles Ebner for agreeing to sit on my committee and for numerous discussions about surfaces and kinetic Monte Carlo. Also for agreeing to hear my defense on December 30th when everyone else in the world is at home and having fun.

... Jon Pelz for agreeing to sit on my committee and for numerous discussions about semiconductor surfaces, STM, and STS. Also for agreeing to hear my defense on December 30th when everyone else in the world is at home and having fun.

... Sheikh Akbar for agreeing to sit on my committee and hear my defense on December 30th when everyone else in the world is at home and having fun.

...Nikolay Piskun for doing all the stuff I didn't have time to do.

...Brad Turpin for doing all the other stuff I didn't have time to do.

... Caffé Fino just for being there.

This research was conducted using the resources of the Cornell Theory Center, which receives major funding from the National Science Foundation (NSF) and New York State, with additional support from Advanced Research Projects (ARPA), the National Center for Research Resources at the National Institutes of Health (NIH), IBM Corporation and other members of the Center's Corporate Partnership Program.

Đời là bể khổ.

## CURRICULUM VITAE

- August 19, 1964 . . . . . Born — Cherry Point, N.C.
- 1988 . . . . . B.S. Physics, University of Colorado,  
Colorado Springs
- 1990 . . . . . M.S., University of Colorado, Colorado Springs
- 1992–1993 . . . . . Researcher, Wright Laboratory, WPAFB
- 1993–present . . . . . Research Assistant, Dept. of Physics,  
Ohio State University, Columbus, Ohio

### PUBLICATIONS

J.G. LePage and R.E. Camley, “Spin-wave spectrum of a superlattice with antiferromagnetic interfacial coupling”, *Physical Review B*, **40**, 9113 (1989).

J.G. LePage and R.E. Camley, “Surface phase transitions and spin-wave modes in semi-infinite magnetic superlattices with antiferromagnetic interfacial coupling”, *Physical Review Letters*, **65**, 1152 (1990).

### FIELD OF STUDY

Major Field: Physics

Subfield: Theory of Semiconductor Surfaces

## TABLE OF CONTENTS

Abstract . . . . .	ii
Dedication . . . . .	iii
Acknowledgements . . . . .	iv
Vita . . . . .	vii
Table of Contents . . . . .	viii
List of Tables . . . . .	x
List of Figures . . . . .	xii

<u>Chapter</u>	<u>Page</u>
1. Introduction . . . . .	1
1.0 Advertisement . . . . .	1
1.1 Overview of the Thesis . . . . .	2
1.2 The PAW Method . . . . .	4
1.3 Practical Motivation: MBE . . . . .	4
1.4 Practical Motivation: Surface Characterization . . . . .	6
2. An Introduction to the Projector Augmented Wave Method . . . . .	7
2.0 Advertisement . . . . .	7
2.1 Foreshadowing . . . . .	8
2.2 The One-Electron Equation: DFT-LDA . . . . .	9
2.3 The Kohn-Sham Equations: Self-Consistency Loop . . . . .	12
2.4 The Generalized Matrix Eigenvalue Problem . . . . .	14
2.5 The PAW Wave Function: Motivation . . . . .	16
2.6 The PAW Basis Set . . . . .	18
2.7 Construction of $ \phi^{(ps-at)}\rangle$ , $ \phi^{(ps-at)}\rangle$ , and $ \tilde{p}\rangle$ . . . . .	26
2.8 Operators in PAW . . . . .	37
2.9 Electron Density, Total Energy and Hamiltonian . . . . .	41
3. Reconstruction Geometries . . . . .	47

3.0 Advertisement	47
3.1 Repeated Slab Model and Surface Termination	48
3.2 Details of the Calculation	50
3.3 Electron Counting Model	53
4. Diffusion of Ga Adatoms on GaAs(100)-c(4x4)	63
4.0 Introduction	63
4.1 Computational Strategy: PAW Investigation of Diffusion	64
4.2 Results: Ga Adatom Energy Surface	67
4.3 Computational Strategy: Monte Carlo Analysis of PAW Data	74
4.4 Results: Monte Carlo Results	76
5. PAW and the Local Density of States	78
5.0 Introduction	78
5.1 LDOS, STM, and STS	78
5.2 PAW and LDOS	79
5.3 LDOS: Results	80
6. PAW and Dielectric Functions	84
6.0 Introduction	84
6.1 PAW Optics	84
7. Conclusions and Future Research	88
7.0 Advertisement	88
7.1 Summary of Dissertation Results	88
7.2 Possible Future Research: Molecular Dynamics	89
7.3 Possible Future Research: Multiple Adatoms	90
7.4 Possible Future Research: Surface Optics	90
Appendix: Convergence Data	92

## Bibliography

Bibliography	108
--------------	-----

## LIST OF TABLES

<u>Table</u>	<u>Page</u>
2.1: Summary of the properties of $ \phi_{l,m,\eta}^{(at)}\rangle$ and $ \phi_{l,m,\eta}^{(ps-at)}\rangle$ and their relationships with each other as well as with the total wave function $ \Psi\rangle$ and the plane wave part $ \psi^{(PW)}\rangle$ . . . . .	23
2.2: Summary of the properties of $ \phi_{l,m,\eta}^{(at)}\rangle$ , $ \phi_{l,m,\eta}^{(ps-at)}\rangle$ , and $ \tilde{p}_{l,m,\eta}\rangle$ and their relationships with each other as well as with the total wave function $ \Psi\rangle$ and the plane wave part $ \psi^{(PW)}\rangle$ . . . . .	27
4.1: The activation energies for the transitions from bonding site to bonding site. . . . .	73
A.1: Raw data for the GaAs(100)-c(4x4) system at a plane wave cutoff of 5 Hartrees. . . . .	94-95
A.2: Table of $\Delta_{a,b}(\Gamma, 4k)$ for the GaAs(100)-c(4x4) system. The “difference of the differences” $\Delta_{\Delta}^{a,b}(\Gamma, 4k) = (\delta_a(\Gamma, 4k) - \delta_b(\Gamma, 4k))$ for a given set of adatom positions $a$ and $b$ is found at the $a$ th row and $b$ th column. . . . .	96-99
A.3: The total energies of the {GaAs(100)-c(4x4) + Ga adatom} system for Brillouin zone integration schemes using $\Gamma$ -point, 4 special k-points, and 16 special k-points. . . . .	100
A.4: Raw data for the GaAs(100)-c(4x4) system at plane wave cutoffs of 5 and 10 Hartrees. This data was calculated using $\Gamma$ -point sampling of the Brillouin zone. . . . .	101

A.5: Table of $\Delta_{a,b}(5E_H, 10E_H)$ for the {GaAs(100)-c(4x4) + Ga adatom} system. The “difference of the differences” $\Delta_{\Delta}^{a,b}(5E_H, 10E_H) = (\Delta_a(5E_H, 10E_H) - \delta_b(5E_H, 10E_H))$ for a given set of adatom positions $a$ and $b$ is found at the $a$ th row and $b$ th column. . . .	102-104
A.6: Raw data for the GaAs(100)-c(4x4) system at plane wave cutoffs of 5 and 10 Hartrees. This data was calculated using 4 k-point sampling of the Brillouin zone. . . . .	105
A.7: Raw data for the GaAs(100)-c(4x4) system for vacuum interface thicknesses of $13 a_0$ and $18 a_0$ . The data was calculated using 4 k-point sampling of the Brillouin zone and a plane wave cutoff of 5 Hartrees. . . . .	106
A.8: Raw data for the GaAs(100)-c(4x4) system for different slab thicknesses. The thinner slab (the one used for most of the calculations in this study) consisted of a terminating GaAs(001)-c(2x2) reconstruction, four “bulk” layers, and a dimer layer of As. The thicker slab had eight “bulk” layers. . . . .	107

## LIST OF FIGURES

<u>Figure</u>	<u>Page</u>
2.1: Complete self-consistent potential (lower surface) and PAW “interstitial” potential (upper surface). The lower surface in this figure is the complete self-consistent potential $V_{eff}(x, y, z = 0)$ of Si in the plane of one of the faces of the conventional cubic unit cell, as calculated by PAW. The upper surface is the PAW “interstitial” potential. . . . .	17
2.2: All-electron potential $V_{eff}^{(at)}$ , local potential $V_{eff}^{(ps-local)}$ , and nonlocal $w_{l,\eta}$ pseudopotentials for the PAW gallium atomic setup used in the calculations. . . . .	31
2.3: All-electron potential $V_{eff}^{(at)}$ , local potential $V_{eff}^{(ps-local)}$ , and nonlocal $w_{l,\eta}$ pseudopotentials for the PAW arsenic atomic setup used in the calculations. . . . .	32
2.4: All-electron atomic wave functions $ \phi_{l,m,\eta,\vec{R}}^{(at)}\rangle$ , the pseudo-atomic wave functions $ \phi_{l,m,\eta,\vec{R}}^{(ps-at)}\rangle$ , and the projector functions $ \tilde{p}_{l,m,\eta,\vec{R}}\rangle$ in the PAW atomic setup for Ga. This particular PAW basis has only one projector per $l$ . The $l = 0$ (s) wave functions are plotted in the top graph, the $l = 1$ (p) wave functions in the middle and the $l = 2$ (d) wave functions at the bottom. . . . .	35



2.5: All-electron atomic wave functions $ \phi_{l,m,\eta,\vec{R}}^{(at)}\rangle$ , the pseudo-atomic wave functions $ \phi_{l,m,\eta,\vec{R}}^{(ps-at)}\rangle$ , and the projector functions $ \tilde{p}_{l,m,\eta,\vec{R}}\rangle$ in the PAW atomic setup for As. This particular PAW basis has only one projector per $l$ . The $l = 0$ (s) wave functions are plotted in the top graph, the $l = 1$ (p) wave functions in the middle and the $l = 2$ (d) wave functions at the bottom. . . . .	36
2.6: The logarithmic derivative function $D_l(\epsilon) = r\partial \ln(\phi_l(r, \epsilon))/\partial r$ for the PAW gallium atomic setup used in the ground state calculations. . . . .	38
2.7: The logarithmic derivative function $D_l(\epsilon) = r\partial \ln(\phi_l(r, \epsilon))/\partial r$ for the PAW arsenic atomic setup used in the ground state calculations. . . . .	39
3.1: Perspective drawing showing the calculated geometry of the Si(001)-(2x1) surface. The slab is terminated on both sides by the same reconstruction . . . . .	54
3.2: Detailed diagram showing the calculated geometry of the Si(001)-(2x1) surface. . . . .	55
3.3: Perspective drawing showing the calculated geometry of the GaAs(001)- c(4x4) surface. The surface is terminated on the bottom by the GaAs(001)- c(2x2) reconstructed surface. . . . .	56
3.4: Detailed diagram showing the calculated geometry of the GaAs(001)-c(2x2) reconstructed surface. This surface was used to terminate the non-interesting side of the GaAs slab. . . . .	57
3.5: Top (above) and Side (below) views of the GaAs(001)-c(4x4) reconstructed surface. . . . .	58

3.6: Large scale schematic diagram of the GaAs(001)-c(4x4) reconstructed surface (top view). . . . .	59
3.7: Large scale diagram of the GaAs(001)-c(4x4) reconstructed surface (side view). . . . .	60
3.8: Explanation of the electron counting rule. . . . .	61
4.1: Large scale schematic diagram of the GaAs(001)-c(4x4) reconstructed surface (top view) showing the positions of the sampling points at which $E_{adatom}(x, y)$ was evaluated. . . . .	66
4.2: The calculated potential energy surface $E_{adatom}(x, y)$ for Ga adatom diffusion on the GaAs(001)-c(4x4) surface. . . . .	68
4.3: The calculated potential energy surface $E_{adatom}(x, y)$ for Ga adatom diffusion on the GaAs(001)-c(4x4) surface. A 2-dimensional contour map corresponding to the 3-dimensional surface is shown on the plane below. . . . .	69
4.4: Perspective drawing of the GaAs(001)-c(4x4) system with a Ga adatom at bonding site I. . . . .	70
4.5: Perspective drawing of the GaAs(001)-c(4x4) system with a Ga adatom at bonding site II. . . . .	71
4.6: Perspective drawing of the GaAs(001)-c(4x4) system with a Ga adatom at bonding site III. . . . .	72
5.1: Contour plot of the local density of states (LDOS) above the Si(001)-(2x1) surface evaluated at an energy of -0.82 eV with respect to the highest occupied state. At this energy the up atom in the buckled dimer shows up in the LDOS but the down atom does not. . . . .	82

5.2: Contour plot of the local density of states (LDOS) above the Si(001)-(2x1) surface evaluated at an energy of 0.4 eV with respect to the highest occupied state. At this energy both up and down atoms in the buckled dimer show up in the LDOS.	83
6.1: The imaginary part of the dielectric function for Si as calculated by PAW, full potential LMTO and as measured by experiment.	86
6.2: The imaginary part of the dielectric function for GaAs as calculated by PAW, full potential LMTO and as measured by experiment.	87

# **CHAPTER 1**

## **INTRODUCTION**

### **1.0 Advertisement**

The focus of this work is the exploration of the physics of semiconductor surfaces via theoretical means. More specifically, we have conducted a series of *ab-initio* theoretical investigations into the electronic properties, structural aspects, and diffusion mechanisms of three such surfaces.

We began our study with a determination of the ground state geometries of the GaAs(100)-c(4x4), GaAs(100)-c(2x2), and Si(001)-(2x1) surfaces. Next, for the GaAs(100)-c(4x4) surface an intensive and computationally demanding calculation of the diffusion characteristics of a lone Ga adatom was conducted. This calculation gives us a unique glimpse of the microscopic processes that govern the motion of atoms on a surface. For the Si(001)-(2x1) surface, a calculation of the local density of states was performed. The results of such calculations have special promise in the field of surface physics in that they can be used to interpret<sup>1</sup> scanning tunneling microscopy data and thereby increase the utility of STM.

The rationale for conducting this research is two-fold. First, as the dimensions

of semiconductor devices continually decrease, the need for a better understanding of the processes that occur on surfaces during the growth of such devices becomes increasingly acute. Second, from a basic science perspective, the complex and little understood physics seen on semiconductor surfaces offer the researcher an irresistible target. With this in mind, we have employed the newly developed Projector Augmented Wave (PAW) method<sup>2</sup> to probe these surfaces. The PAW method is a powerful new technique that combines the best features of the pseudopotential<sup>3</sup> and LAPW methods<sup>4,5</sup> with none of their disadvantages. Implemented in terms of the highly efficient Car-Parrinello<sup>6,7</sup> molecular dynamics algorithm, the PAW method is capable of the high speed that is required to handle the large and unwieldy structures dealt with in this study.

Due to the large size and complicated physics of surface systems, the computational demands of these calculations are severe. However, the payoff is well worth the cost. Theoretical techniques like the ones used here can probe surfaces in ways that are well beyond the capabilities of even the best experimental techniques.

In addition to all this, we have expanded the utility of PAW beyond ground state calculations by implementing the first ever PAW optical code. As yet, no surface calculations have been performed using this new code. However, the results of our test calculations on bulk GaAs and bulk Si are extremely promising.

## 1.1 Overview of the Thesis

Chapter 1 introduces the theoretical techniques and physical systems that appear in this work. Additionally, the connection between this work and the growth and characterization of thin films is made explicit.

Chapter 2 gives a detailed discussion of the Projector Augmented Wave method.<sup>2</sup> The first five sections are devoted to a low-level explanation of density functional theory (DFT)<sup>8</sup> and the related local density approximation (LDA).<sup>9,10</sup> The remaining four sections introduce the PAW formalism. After a motivational explanation for the form of the PAW wave function ansatz is given, the PAW forms for the total energy  $E_T$ , the electron density  $n(\vec{r})$ , and the Hamiltonian and overlap operators are derived.

Chapter 3 gives the specifics of the calculations of the ground state geometries of the GaAs(100)-c(4x4), GaAs(100)-c(2x2), and Si(100)-(2x1) surfaces. Detailed diagrams of the geometries along with 3-dimensional perspective drawings of the systems are given.

Chapter 4 presents the calculated diffusion data for a Ga adatom on a GaAs(100)-c(4x4) surface. This data is in the form of a potential energy surface for an isolated Ga adatom as a function of x-y position. Similar calculations have been performed by other groups for reconstructions on Si(001)<sup>11</sup> and GaAs(100)<sup>12,13</sup> In principle, this energy surface contains all the essential physics of Ga adatom diffusion *for this surface*. The bonding sites and activation barriers are identified, and the results of a lattice Monte-Carlo<sup>14</sup> simulation are presented.

Chapter 5 begins with a derivation of the Tersoff-Hamann<sup>1</sup> approximation of the scanning tunneling microscope (STM) tunneling current. In this approximation the local density of states is trivially related to the STM tunneling current. The relationship between the local density of states and scanning tunneling spectroscopy is also given. The chapter ends with the presentation of the local density of states data for the Si(100)-(2x1) surface as calculated using PAW.

Chapter 6 begins with a derivation of the PAW form of the optical transition matrix and ends with a presentation of the calculated optical data for bulk GaAs and bulk Si.

Chapter 7 presents the conclusions and suggests possible directions for new research.

## 1.2 The PAW Method

In this work we used the newly formulated Car-Parrinello Projector Augmented Wave (CP-PAW) molecular dynamics method to investigate the properties of several physical systems. This method combines the best aspects of the leading *ab-initio* electronic structure methods such as the pseudopotential<sup>3</sup> and the linear augmented plane wave<sup>4,5</sup> methods (LAPW) with none of their disadvantages. Like the LAPW method, the PAW method is capable of treating all elements, even those with d- or f- orbitals in the outer shell. Further, since PAW is an all-electron method (like LAPW), the core wave functions are naturally included in the calculations. Like the pseudopotential method, forces are easily calculated. Thus, PAW has all the capabilities of LAPW and the pseudopotential methods. Indeed, PAW can be viewed as the natural generalization (and improvement) of the two previous methods. This method has previously been tested and used to study a number of physical systems.<sup>15,16</sup>

## 1.3 Practical Motivation: MBE

To guide the development of thin film growth technology, a number of groups

have made theoretical studies of vapor phase epitaxy.<sup>17,18</sup> Sadly, most of the models require the knowledge of a large number of input parameters whose precise values are difficult to determine via experiment. For example, lattice Monte Carlo simulations typically require that the desorption, adsorption, and surface diffusion energetics be fairly well understood at the atomic level. However, the exact values of the relevant activation energies are generally not known accurately. In the absence of good experimental data, Monte Carlo theorists often resort to rough approximations designed to produce a final simulation which is in reasonable agreement with the known growth morphology. As a result, current lattice Monte Carlo simulation programs are entirely incapable of producing quantitative predictions and are only useful as qualitative guides.<sup>19</sup> On the other hand, such techniques are quite capable of modeling, however imprecisely, the MBE deposition of several complete monolayers.

One of the purposes of this study is to improve the state-of-the-art of simulations of MBE growth by using *ab-initio* techniques to generate diffusion parameters. Hopefully, improvements in MBE *simulations* will eventually translate into improvements in MBE growth techniques. Unfortunately, *ab-initio* simulations, while capable of high accuracy, are so computationally demanding that only very small systems can feasibly be studied. Therefore, rather than attempt an actual simulation of growth via these techniques, we will adopt a more cautious strategy and merely calculate the self-consistent potential energy surface for a single isolated adatom. An analysis of this data will yield the diffusion characteristics in the dilute case. More ambitious calculations involving multiple adatoms can always come later.



#### **1.4 Practical Motivation: Surface Characterization**

In addition to improving MBE simulations, PAW has the potential to aid in the interpretation of surface characterization data. In particular, we have used PAW to generate the surface local density of states, which can be used to interpret STM data. Based on early bulk tests, PAW also shows promise as an optical probe.

## CHAPTER 2

### AN INTRODUCTION TO THE PROJECTOR AUGMENTED WAVE METHOD

#### 2.0 Advertisement

The PAW method is designed to allow easy calculation of the electronic structure of molecules and solid state systems. Additionally, PAW can be used to find inter-atomic forces and perform molecular dynamics simulations. PAW, like LMTO<sup>20,21</sup> and LAPW,<sup>4,5</sup> is an all-electron method and, as such, accurately calculates the electronic wave functions in all regions, including the core region. In this chapter we will outline the basics of the this method.<sup>†</sup> The first four sections will deal with the basics of density functional theory, upon which PAW is based, while the remaining sections will give the specifics of the PAW method. Since this chapter is intended for the widest possible audience, some may find the treatment

---

<sup>†</sup> Here and throughout the thesis, we will use atomic units. In this unit system  $\hbar = m_e = e = 1$  and the kinetic energy operator is simply  $-\frac{1}{2}\nabla^2$  rather than the usual  $-\frac{\hbar^2}{2m_e}\nabla^2$ . The unit of energy is the Hartree :  $1 E_H = m_e e^2 / \hbar \approx 27.2116$  eV. The unit of distance is the Bohr :  $a_0 = (\hbar/e)^2 / m_e = 0.529177$  Å. The unit of time is the (nameless) constant  $\tau_0 = \hbar / E_H = 2.418 \times 10^{-17}$  sec. The unit of mass is the mass of the electron :  $m_e = 9.1094 \times 10^{-31}$  kg.

a little elementary. Readers familiar with *ab-initio* calculations may wish to skip ahead to section 2.5.

## 2.1 Foreshadowing

In principle, an investigation of the electronic properties of a solid state system should begin with the Schrödinger equation for the N-particle wave function<sup>†</sup>  $|\Psi(\vec{r}_1, \vec{r}_2, \dots, \vec{r}_N)\rangle$ :

$$H|\Psi\rangle = \sum_{i=1}^N \left( -\frac{1}{2} \nabla_i^2 |\Psi\rangle - \sum_{\vec{R}} \frac{Z_{\vec{R}}}{|\vec{r}_i - \vec{R}|} |\Psi\rangle \right) + \frac{1}{2} \sum_{i \neq j} \frac{1}{|\vec{r}_i - \vec{r}_j|} |\Psi\rangle = E|\Psi\rangle. \quad (2.1)$$

However, through a series of approximations and simplifications we will reduce this many-electron equation to a much simpler form. First, we will use density functional theory (DFT)<sup>8</sup> to formally transform the many-electron equation to a one-electron equation. Within the DFT formalism, the local density approximation (LDA)<sup>9,10</sup> will be used to simulate the effects of exchange and correlation in a computationally feasible way. Next, we will expand our wave function in terms of a set of non-orthogonal basis functions and thereby transform the differential Schrödinger equation into a system of linear algebraic equations. This set of equations can then be solved using any one of a number of different techniques (matrix diagonalization,<sup>‡</sup> steepest descents, conjugate-gradient,<sup>22</sup> etc.). In the present implementation, the Car-Parrinello<sup>6,7</sup> method is used to find the self-consistent ground state while

<sup>†</sup> Here and throughout the thesis we shall make extensive use of the Dirac bra-ket notation. In this notation, a wave function in real space is written as  $\Psi(\vec{r}) = \langle \vec{r} | \Psi \rangle$  and its complex conjugate as  $\langle \Psi | \vec{r} \rangle$ . The ket version of a plane wave  $e^{i\vec{k} \cdot \vec{r}}$  is simply  $|\vec{k}\rangle$  and an expansion of  $|\Psi\rangle$  in terms of plane waves is written as  $|\Psi\rangle = \sum_{\vec{G}} |\vec{G}\rangle \langle \vec{G} | \Psi \rangle$ .

<sup>‡</sup> If the basis set is orthogonal, then the problem reduces to the standard matrix

standard matrix diagonalization is used during the calculation of the density of states, the local density of states and the dielectric function.

After discussing the general form of DFT-LDA calculations and the special complications introduced by a non-orthogonal basis set, we will proceed to a discussion of the specific features of PAW. First, a rationale for the general form of the PAW wave function will be presented. Next, the PAW forms for the electron density  $n(\vec{r})$ , the effective potential  $V_{eff}(\vec{r})$ , the Hamiltonian  $H$ , and the total energy  $E_T$  will be derived.

## 2.2 The One-Electron Equation: DFT-LDA

Like many other *ab-initio* methods, PAW is defined within the context of density functional theory (DFT) and uses the local density approximation (LDA). Density functional theory rigorously maps the ground state of an interacting electron gas onto the corresponding ground state of a system of non-interacting electrons moving through an effective potential  $V_{eff}(\vec{r})$ . In principle, if  $V_{eff}(\vec{r})$  is known to arbitrary precision, then it is possible to calculate the correct total energy, including the exchange and correlation energies, via the one-electron Hamiltonian  $H = \frac{1}{2}\nabla^2 + V_{eff}(\vec{r})$ .

The potential  $V_{eff}(\vec{r})$  can be divided into three parts. The first part, usually referred to as the external potential<sup>22</sup> is merely the potential  $V_{ion}(\vec{r})$  felt by an

---

eigenvalue problem  $\hat{H}\vec{c} = E\vec{c}$ . In the non-orthogonal case, the generalized matrix eigenvalue problem results:  $\hat{H}\vec{c} = E\hat{O}\vec{c}$ . Here  $\hat{O}$  is the overlap matrix. This equation can be transformed via Cholesky decomposition into the standard problem. Once this transformation is done, the solution can be found using any convenient eigenvalue subroutine package.

electron due to the presence of the lattice ions<sup>†</sup> located at the atomic coordinates  $\{\vec{R}\}$ . Generally,  $V_{ion}(\vec{r})$  manifests itself as an equation of the form

$$V_{ion}(\vec{r}) = \sum_{\vec{R}} v_{atomic}(\vec{r} - \vec{R}) = \sum_{\vec{R}, l, m} v_{atomic}(|\vec{r} - \vec{R}|) Y_l^m(\hat{r}_{\vec{R}}), \quad (2.2)$$

where

$$\hat{r}_{\vec{R}} = \frac{\vec{r} - \vec{R}}{|\vec{r} - \vec{R}|}. \quad (2.3)$$

With certain modifications, this is how the term appears in the PAW formalism.

The second part of  $V_{eff}(\vec{r})$  is the electrostatic potential (the Hartree potential) due to the electrons. If  $n(\vec{r})$  is the total electron density at point  $(\vec{r})$  given by

$$n(\vec{r}) = \sum_{\text{states } i} f_i |\Psi_i(\vec{r})|^2, \quad (2.4)$$

where  $f_i$  is the occupation of the state with the one-electron wave function  $\Psi_i(\vec{r})$ , then this potential is given by

$$V_{Hartree}(\vec{r}) = \int_V \frac{n(\vec{r}')}{|\vec{r} - \vec{r}'|} d^3r'. \quad (2.5)$$

The final part of the complete potential, and the most difficult to calculate exactly, is the exchange-correlation potential. This quantity is defined formally as the functional derivative of the exchange-correlation energy  $E_{XC}[n(\vec{r})]$ :

$$V_{XC}(\vec{r}) = \frac{\delta E_{XC}[n(\vec{r})]}{\delta n(\vec{r})}. \quad (2.6)$$

The exchange-correlation energy functional is in turn defined formally as the difference between the true total energy and the Hartree energy. We can implicitly define the exchange-correlation energy per electron  $\epsilon_{XC}(\vec{r})$ :

$$\frac{\delta E_{XC}[n(\vec{r})]}{\delta n(\vec{r})} = \frac{\partial [n(\vec{r}) \epsilon_{XC}(\vec{r})]}{\partial n(\vec{r})}. \quad (2.7)$$

---

<sup>†</sup> Actually, the external potential contains any static term that cannot be written as a function of the electron density.

The main point of density functional theory is that the total energy of an electron gas including the exchange and correlation energies is a unique functional of the total electron density. Having introduced the various potentials as well as the exchange-correlation energy, we are now in a position to write down the full total-energy functional:

$$\begin{aligned}
E_T[\{\Psi_i; \vec{R}\}] = & \sum_{\text{occupied states}} \int \Psi_i^* \left[ -\frac{1}{2} \nabla^2 \right] \Psi_i d^3r + \int V_{ion}(\vec{r}) n(\vec{r}) d^3r \\
& + \frac{1}{2} \int \frac{n(\vec{r}) n(\vec{r}')}{|\vec{r} - \vec{r}'|} d^3r d^3r' + E_{XC}[n(\vec{r})] + E_{ion-ion}(\{\vec{R}\}).
\end{aligned} \tag{2.8}$$

The term  $E_{ion-ion}(\{\vec{R}\})$  in this equation is simply the energy of interaction between the lattice ions.

In principle, density functional theory will always yield the true ground state as long as  $V_{eff}(\vec{r})$  is known exactly. In practice however, the determination of  $V_{XC}(\vec{r})$  is usually beyond our capabilities, and we must resort to approximations such as the local density approximation (LDA). In the local density approximation, it is assumed that the exchange-correlation potential at a point  $\vec{r}$  depends only on the electron density  $n(\vec{r})$  at that point. To elaborate, if the electron density at point  $\vec{r}$  within an *inhomogeneous* electron gas is  $n(\vec{r})$ , and  $\epsilon_{XC}(\vec{r})$  is the corresponding exact exchange-correlation energy per electron, then the exact exchange-correlation energy for the entire system is simply

$$E_{XC}[n(\vec{r})] = \int \epsilon_{XC}(\vec{r}) n(\vec{r}) d^3r. \tag{2.9}$$

If we now substitute the exchange-correlation energy per electron for a *homogeneous* electron gas  $\epsilon_{XC}^{hom}(n)$  for the corresponding term  $\epsilon_{XC}(\vec{r})$  for an *inhomogeneous* gas, we arrive at the local density approximation (LDA) for the exchange-correlation

energy:

$$E_{XC}^{LDA}[n(\vec{r})] \equiv \int \epsilon_{XC}^{hom}(n(\vec{r}))n(\vec{r})d^3r. \quad (2.10)$$

Hereafter, the superscript ‘‘LDA’’ in  $E_{XC}^{LDA}[n(\vec{r})]$  will be omitted.

### 2.3 The Kohn-Sham Equations: Self-Consistency Loop

The Hamiltonian  $H$ , the effective potential  $V_{eff}(\vec{r})$ , and the electron density  $n(\vec{r})$  are related by the Kohn-Sham equations:

$$H = -\frac{1}{2}\nabla^2 + V_{eff}(\vec{r}) \quad (2.11)$$

$$\begin{aligned} V_{eff}(\vec{r}) &= V_{ion}(\vec{r}) + V_{Hartree}(\vec{r}) + V_{XC}(\vec{r}) \\ &= V_{ion}(\vec{r}) + \int_V \frac{n(\vec{r}')}{|\vec{r} - \vec{r}'|} d^3r' + V_{XC}(n(\vec{r})), \end{aligned} \quad (2.12)$$

$$n(\vec{r}) = \sum_{i \text{ occ states}} |\Psi_i(\vec{r})|^2. \quad (2.13)$$

Given these relationships, the solution of the system must be determined via a self-consistency loop. Since the computational demands of the solution of the Hamiltonian are severe, the method used to reach self-consistency must be both swift and robust. Over the years, a great deal of effort has been expended in the search for better and faster methods of getting to the self-consistent ground state.<sup>22</sup> In the current implementation of PAW, the ground state is found using the Car-Parrinello method.<sup>7,23</sup> In this method, the physical system is described in terms of a **fictitious** Lagrangian:

$$\begin{aligned} L_{CP} &= \mu \sum_{states i} \langle \dot{\Psi}_i | \dot{\Psi}_i \rangle + \frac{1}{2} \sum_{\vec{R}} M_{\vec{R}} \dot{\vec{R}}^2 - E_T[\{\Psi_i; \vec{R}\}] \\ &+ \sum_{states i,j} \Lambda_{i,j} (\langle \Psi_i | \Psi_i \rangle - \delta_{i,j}), \end{aligned} \quad (2.14)$$

In the equation above, the wave functions  $\Psi_i$  are considered to be classical fields and  $\dot{\Psi}_i$  is simply the time derivative of  $\Psi_i$ . The  $\Lambda_{ij}$  in the last term of (2.14) are the Lagrange multipliers which insure that the  $\Psi_i$  remain orthonormal. Given this Lagrangian, the equation of motion for the occupied electronic wavefunctions is

$$\mu \ddot{\Psi}_i(\vec{r}, t) = -H\Psi_i(\vec{r}, t) + \sum_j \Lambda_{ij}\Psi_j(\vec{r}, t). \quad (2.15)$$

The corresponding equation of motion for the nuclei at  $\vec{R}_I$  is

$$M_{\vec{R}_I} \ddot{\vec{R}}_I = -\frac{\partial E_T}{\partial \vec{R}_I} = F_{\vec{R}_I}, \quad (2.16)$$

where the  $F_{\vec{R}_I}$  is the force acting on the nuclei. The associated equation of constraint (due to orthogonality) is

$$\int \Psi_i^*(\vec{r}, t)\Psi_j(\vec{r}, t)d^3r = \delta_{ij}. \quad (2.17)$$

The equations of motion (2.15) and (2.16) are integrated numerically using the Verlet algorithm. Specifically, if  $\Delta$  is the integration time step, the position of the  $I$ th ion at time  $t$  is

$$\vec{R}_I(t) = 2\vec{R}_I(t - \Delta) - \vec{R}_I(t - 2\Delta) - F_{\vec{R}_I}(t - \Delta)\frac{\Delta^2}{M_{\vec{R}_I}}. \quad (2.18)$$

The corresponding equation for the  $i$ th wavefunction at time  $t$  is

$$|\Psi_i(t)\rangle = 2|\Psi_i(t - \Delta)\rangle - |\Psi_i(t - 2\Delta)\rangle - \left( -H|\Psi_i(t - \Delta)\rangle + \sum_j \Lambda_{ij}|\Psi_j(t - \Delta)\rangle \right) \frac{\Delta^2}{M_{\vec{R}_I}}. \quad (2.19)$$

The principal advantage of the Car-Parrinello method is that it can simultaneously optimize both the ionic and electronic coordinates.



## 2.4 The Generalized Matrix Eigenvalue Problem

Through the use of DFT-LDA, we reduce the complicated many-body Hamiltonian to a simple one-electron Hamiltonian operator:

$$H = -\frac{1}{2}\nabla^2 + V_{\text{eff}}(\vec{r}) = -\frac{1}{2}\nabla^2 + V_{\text{ion}}(\vec{r}) + V_{\text{Hartree}}(\vec{r}) + V_{\text{XC}}(\vec{r}). \quad (2.20)$$

Once DFT-LDA has been invoked and we have created our one-electron Hamiltonian operator, we are ready to transform our differential operator  $H$  into the form of a matrix operator  $\hat{H}$ . We do this by introducing an ansatz for the wave function  $\Psi(\vec{r})$  in the form of a simple expansion in terms of a (currently unspecified) basis function set  $\{a_j(\vec{r}); j = 1 \dots \infty\}$ :

$$|\Psi_n\rangle = \sum_j c_{j,n} |a_j\rangle. \quad (2.21)$$

Notice that these basis functions need not be orthogonal. There is really only one constraint on the choice of the basis functions: it must be possible to represent the complete wave functions well using only a small subset  $\{a_j(\vec{r}); j = 1 \dots N\}$  of the original infinite set  $\{a_j(\vec{r}); j = 1 \dots \infty\}$ . Of course, the definition of “small” depends mostly on the capabilities of the computer on which the calculation will be performed. In our case, a simulation of bulk Si or GaAs will involve a basis set containing a few hundred elements. Written in terms of the truncated non-orthogonal basis set  $\{a_j(\vec{r}); j = 1 \dots N\}$ , the Schrödinger equation reduces to a *generalized* matrix eigenvalue problem: sequentially,

$$H|\Psi_n\rangle = E_n|\Psi_n\rangle, \quad (2.22)$$

$$H \sum_j c_{j,n} |a_j\rangle = E_n \sum_j c_{j,n} |a_j\rangle, \quad (2.23)$$

$$\langle a_i | H [\sum_j c_{j,n} |a_j\rangle] = E_n \sum_j c_{j,n} \langle a_i | a_j \rangle, \quad (2.24)$$

$$\sum_j c_{j,n} \langle a_i | H | a_j \rangle = E_n \sum_j c_{j,n} \langle a_i | a_j \rangle. \quad (2.25)$$

Denoting an element of the Hamiltonian matrix as  $\hat{H}_{ij} = \langle a_i | H | a_j \rangle$ , an element of the overlap matrix as  $\hat{O}_{ij} = \langle a_i | a_j \rangle$ , and  $\vec{c}_n(j) = c_{j,n}$ , we can write the Schrödinger equation in matrix notation:

$$\hat{H} \vec{c}_n = E_n \hat{O} \vec{c}_n. \quad (2.26)$$

This equation can be transformed into the standard symmetric eigenvalue problem via the Cholesky decomposition:

$$\hat{O} = \hat{L} \hat{L}^\dagger, \quad (2.27)$$

where  $\hat{L}$  is a lower triangular matrix and  $\hat{L}^\dagger$  is its Hermitian adjoint. Replacing  $\hat{O}$  by its Cholesky decomposition and multiplying by  $\hat{L}^{-1}$ , we get

$$\hat{L}^{-1} \hat{H} \vec{c}_n = E_n \hat{L}^\dagger \vec{c}_n. \quad (2.28)$$

If we then insert identity in the form of  $\hat{L}^{-1} \hat{L}$  and regroup the terms, we get

$$\left( \hat{L}^{-1} \hat{H} \hat{L}^\dagger \right) \left( \hat{L}^\dagger \vec{c}_n \right) = E_n \left( \hat{L}^\dagger \vec{c}_n \right). \quad (2.29)$$

Equation (2.29) now has the same form as equation (2.26) and can be solved using any standard eigenvalue subroutine package.

Notice that if the set  $\{a_j(\vec{r}); j = 1..N\}$  were orthogonal the  $\hat{O}$  matrix would be unity and the usual symmetric eigenvalue equation would result. However, as we shall soon see, the PAW basis set is generally non-orthogonal.

## 2.5 The PAW Wave Function: Motivation

To summarize the previous three sections, first we used density functional theory together with the local density approximation in order to map the intrinsically many-body solid state problem onto the much simpler one-electron problem. Second, we approximated the eigenfunctions of the system as expansions in terms of a truncated basis set. The final result should be a generalized matrix eigenvalue problem of reasonable size. However, if the set  $\{a_j(\vec{r}); j = 1..N\}$  is not well chosen, then a large basis set will be required and the size of the Hamiltonian and overlap matrices will grow beyond manageable proportions. Obviously, the key to an efficient calculation of the electronic structure lies in finding a good basis set.

From a naive point of view, the solution of the one-electron problem should be fairly simple. Unfortunately, this is not so. The basic problem with calculating the electronic structure of real systems is not the complexity of the Schrödinger equation, which really isn't that complex. Neither is it that the Coulomb divergence at the atomic nuclei is intrinsically difficult to handle; in the proper coordinate system (spherical) the solution is simple. The real problem is that the potential (or conversely, the wave function) has radically different character in different regions.

As shown in Fig. 2.1, near the core the potential  $V_{eff}(\vec{r})$  is distinctly atomic-like, exhibiting pronounced spherical symmetry and possessing a Coulomb divergence at the nucleus. Away from the nucleus, in the chemically active bonding region, the potential is much smoother and mirrors the symmetry of the complete system. If not for the presence of the deep atomic potentials near the core regions, the wave functions could be conveniently expressed in terms of plane waves. Since the

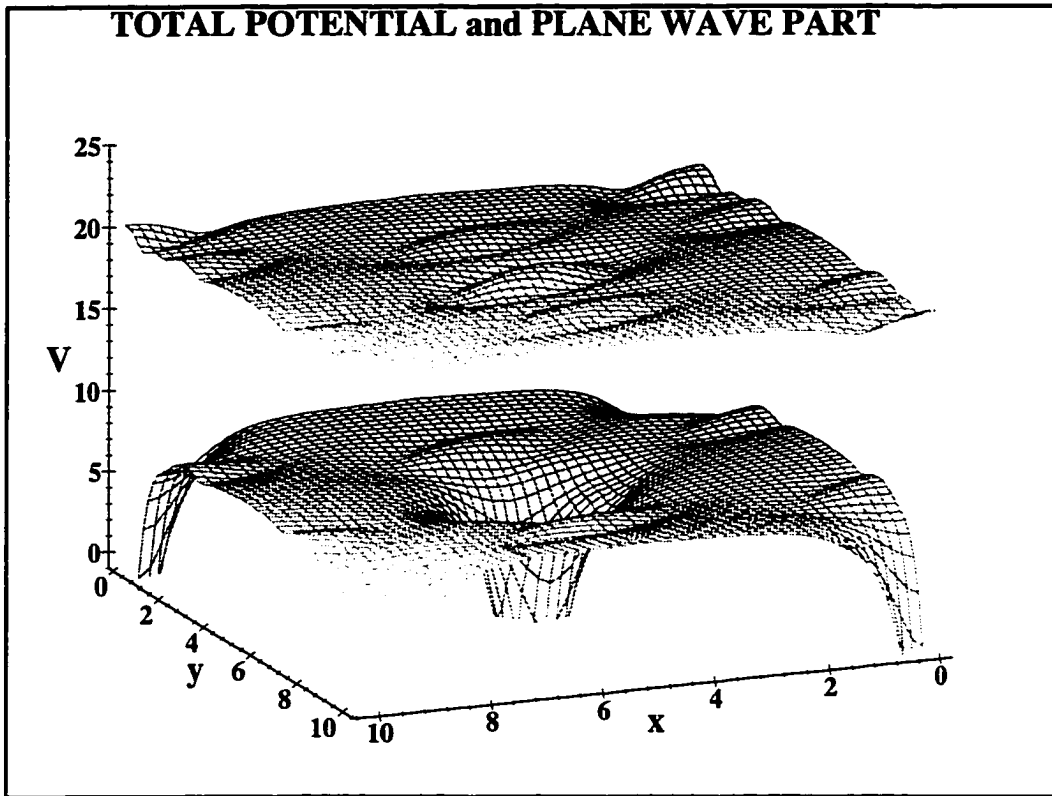


**FIGURE 2.1** Complete self-consistent potential (lower surface) and PAW “interstitial” potential (upper surface). The lower surface in this figure is the complete self-consistent potential  $V_{eff}(x, y, z = 0)$  of Si in the plane of one of the faces of the conventional cubic unit cell, as calculated by PAW. The  $x$ - and  $y$ -positions are given in units of Bohr. The potential is in units of Hartrees. There are atoms at positions  $(0,0)$ ,  $(10.26,0)$ ,  $(0,10.26)$ ,  $(10.26,10.26)$ , and  $(5.13,5.13)$ . The presence of these atoms is made obvious by the deep potential wells at these positions. These deep wells are in sharp contrast to the relatively smooth interstitial region between the atoms. The upper surface is the PAW “interstitial” potential. For clarity, this potential has been shifted upward by 20 Hartrees. The complete potential is formed by a superposition of the PAW interstitial potential and the PAW atomic and pseudo-atomic potentials. Outside the augmentation spheres, which have a radius of 2 Bohr in this case, these potential surfaces are identical.

symmetry of the potential is so different in these two regions, no single coordinate system (or conversely, no single type of basis function) can reasonably be used in all regions. Two basic strategies have been employed to get around this problem.

In the first strategy, known as the pseudopotential method,<sup>3,24</sup> the actual atomic potential is replaced with a “pseudopotential” which is designed to have the same electron scattering properties as the original potential but lacks the inconvenient coulomb divergence of the original. A Hamiltonian formed using these pseudopotentials in place of the true potentials will have wave function solutions that can be easily expressed in terms of a relatively small plane waves basis set. Of course, this “pseudo” wave function differs markedly from the true wave function in the region near the atomic center.

The second strategy is usually referred to as “augmentation.” PAW, like LMTO<sup>25</sup> and LAPW,<sup>4,5</sup> is constructed in the spirit of the augmentation strategy. In these methods, the complete wave function  $\Psi$  is formed from a piecewise continuous and differentiable combination of atomic-like wave functions, which accurately represent the wave function in the region near the atomic center, and smooth “interstitial” functions, which are suited to the behavior of the wave function in the region between the ionic cores. The resulting wave function accurately represents the behavior of the true wave function, even in the core region.

## 2.6 The PAW Basis Set

Peter Blöchl, the inventor of PAW,<sup>2</sup> conceives of his method as a means by which the original Hamiltonian  $H$  is mapped, via a linear transformation  $T$ , onto

a more easily solved pseudo-Hamiltonian  $H^{(ps)}$ :

$$T^\dagger H T = H^{(ps)}. \quad (2.30)$$

In the seminal paper on the method<sup>2</sup>, PAW is introduced and explained using this transformation  $T$  as a starting point. While such a derivation may have certain formal advantages, it lacks an intuitive feel. Therefore, we will introduce the method via a consideration of the PAW wave function ansatz.

PAW begins by dividing up space into two separate regions. The first region (for historical reasons, known as the “augmentation” region) basically consists of the core regions of all the atoms in the system. The second region (the “interstitial” region) consists of the remainder of the system.

#### Augmentation region: detailed definition

Each atom in the system is enclosed within its own nucleus-centered augmentation sphere, and these spheres taken together are referred to as the augmentation region. While there is no precise numerical formula for the radii of these spheres, there are some broad guidelines. At the very least, the radii of these spheres are chosen small enough so that no overlap between neighboring spheres occurs. In addition, the radii should be small enough that the wave functions enclosed retain a pronounced atomic-like quality. Further, the effective potential within these regions should possess a high degree of spherical symmetry. On the other hand, the augmentation radii must not be made so small that the deep potential found within the core region begins to seep out into the interstitial region. In practice most atoms have augmentation regions with radii that are slightly smaller ( $r_{\text{augmentation}} \approx .9r_{\text{covalent}}$ ) than their covalent radii.<sup>†</sup> For Ga and As, this means

<sup>†</sup> As for the covalent radii themselves, the values listed in any standard table

the augmentation radii are on the order of 2 Bohr ( $\approx 1.06 \text{ \AA}$ ). It should be noted that the PAW augmentation region corresponds closely to its LMTO and LAPW namesakes, as well as to the “core” region mentioned in pseudopotential theory.

### Interstitial region: detailed definition

The interstitial region simply consists of all points outside the atomic augmentation regions. The potential within this region should be smooth and should possess the symmetry of the complete system. In PAW, the potential and wave functions in this region are represented in terms of plane waves. In this context, a “smooth” potential may be defined as one having Fourier components with spatial frequencies no greater than around  $5.5 \text{ Bohr}^{-1}$ , corresponding to a plane wave with kinetic energy  $\frac{1}{2}k^2 \leq 15 \text{ Hartrees}$ .

### Preliminary ansatz

Once we have divided our system into augmentation and interstitial regions, we are ready to formulate a preliminary ansatz. Within the augmentation spheres, the natural choice for the basis functions is the set of atomic eigenfunctions  $\phi_{l,m,\eta}^{(at)}(\vec{r}) = \phi_{l,\eta}^{(at)}(r)Y_l^m(\hat{r})$ . These functions satisfy the standard DFT-LDA version of the Schrödinger equation for an isolated atom at the origin:

$$H^{(at)}|\phi_{l,m,\eta}^{(at)}\rangle = [-\frac{1}{2}\nabla^2 + V_{eff}^{(at)}(\vec{r})]|\phi_{l,m,\eta}^{(at)}\rangle = E_{\eta}|\phi_{l,m,\eta}^{(at)}\rangle. \quad (2.31)$$

---

(Sargent-Welch, etc.) can generally be used with good results. After subsequent test calculations, it may be discovered that the original  $r_{aug}$  is not workable. In that event, a new  $r_{aug}$  is chosen and a new set of test calculations is run to test the new  $r_{aug}$ . This process repeats until a reasonable value of  $r_{aug}$  is found. The same is true of any other parameter used in the PAW basis set. The point is that the prescription given in this section should not be followed too rigidly. Rather, the researcher should treat these rules merely as a set of broad guidelines.

Here all operators and wave functions<sup>†</sup> are written in terms of spherical coordinates, and the self-consistent atomic potential  $V_{eff}^{(at)}(\vec{r})$  is calculated within DFT-LDA. Note that the energy  $E_\eta$  need not correspond to a bound state of the atom.<sup>‡</sup> Explicitly, we expand the complete wave function  $|\Psi_{n,\vec{k}}\rangle$  for band  $n$  and wave vector  $\vec{k}$  within the augmentation region centered on an atom at  $\vec{R}$  as:

$$\begin{aligned} |\Psi_{n,\vec{k}}\rangle^{(augmentation)} &= |\Psi_{n,\vec{k}}\rangle^{(aug)} \\ &= \sum_{l,m,\eta} a_{l,m,\eta,\vec{R}}^{n,\vec{k}} |\phi_{l,m,\eta}^{(at)}(\vec{r} - \vec{R})\rangle \\ &= \sum_{l,m,\eta} a_{l,m,\eta,\vec{R}}^{n,\vec{k}} |\phi_{l,\eta}^{(at)}(|\vec{r} - \vec{R}|) Y_l^m(\hat{r}_{\vec{R}})\rangle. \end{aligned} \quad (2.32)$$

In the interstitial region, the wave function is expanded in terms of plane waves:

$$|\Psi_{n,\vec{k}}\rangle^{(interstitial)} = |\psi_{n,\vec{k}}^{(PW)}\rangle = \sum_{\vec{G}} c_{n,\vec{k}+\vec{G}} \bar{e}^{i(\vec{k}+\vec{G})\cdot\vec{r}}. \quad (2.33)$$

Plane waves aren't the only choice possible, but it is the choice used in the current implementation of PAW. The complete wave function for a multiple atom system can be written as

$$|\Psi_{n,\vec{k}}\rangle = \begin{cases} \sum_{\vec{G}} c_{n,\vec{k}+\vec{G}} \bar{e}^{i(\vec{k}+\vec{G})\cdot\vec{r}} & \text{inside interstitial region} \\ \sum_{l,m,\eta,\vec{R}} a_{l,m,\eta,\vec{R}}^{n,\vec{k}} |\phi_{l,m,\eta}^{(at)}(\vec{r} - \vec{R})\rangle & \text{inside augmentation spheres} \end{cases} \quad (2.34)$$

<sup>†</sup> Occasionally the rather cumbersome set of wave function indices  $\{l, m, \eta\}$  will be represented by a collective index, usually denoted as  $i$  or  $j$ . Where space permits and clarity is unhindered the full set  $\{l, m, \eta\}$  will be used.

<sup>‡</sup> In fact, in some cases it may be necessary to calculate a number of  $\phi_{l,\eta}^{(at)}(r)$  at several different energies  $E_\eta$  for a given  $l$ . In this way, we can insure the completeness of the basis set in the augmentation region. However, often one  $\phi_{l,\eta}^{(at)}(r)$  per  $l$  suffices, at least for ground state calculations. In any case we adjust the  $E_\eta$ 's so that the resultant  $\phi_{l,\eta}^{(at)}$ 's form a complete and swiftly convergent basis set in the augmentation region.



At first glance, this ansatz seems fairly reasonable. However, we need to make some modifications before we arrive at something that can be used in a practical scheme. First of all, we need to insure that the complete wave function is continuous and differentiable across the augmentation-interstitial boundary. Second, we need to find a clever way of making the plane wave part of the wave function identically zero inside the augmentation spheres. PAW accomplishes these tasks via the introduction of two new classes of functions: the pseudo-atomic wave functions  $\{|\phi_{l,m,\eta,\vec{R}}^{(ps-at)}\rangle\}$  and the projector functions  $\{|\tilde{p}_{l,m,\eta,\vec{R}}\rangle\}$ . The combined set  $\{|\phi_{l,m,\eta,\vec{R}}^{(at)}\rangle, |\phi_{l,m,\eta,\vec{R}}^{(ps-at)}\rangle, |\tilde{p}_{l,m,\eta,\vec{R}}\rangle\}$  forms the PAW “atomic setup”.

Pseudo-atomic wave functions  $|\phi_{l,m,\eta,\vec{R}}^{(ps-at)}\rangle$

The pseudo-atomic wave functions must satisfy certain conditions. First, they must satisfy the standard DFT-LDA version of the Schrödinger equation for an isolated pseudo-atom: †

$$H^{(ps-at)}|\phi_{l,m,\eta}^{(ps-at)}\rangle = \left[-\frac{1}{2}\nabla^2 + V_{eff}^{(ps-at)}(\vec{r})\right]|\phi_{l,m,\eta}^{(ps-at)}\rangle = E_\eta|\phi_{l,m,\eta}^{(ps-at)}\rangle. \quad (2.35)$$

Second, inside the augmentation spheres, it must be possible to represent the plane wave expansion in terms of the pseudo-atomic wave functions:

$$|\psi_{n,\vec{k}}^{(PW)}\rangle = \sum_{l,m,\eta,\vec{R}} a_{l,m,\eta,\vec{R}}^{n,\vec{k}} |\phi_{l,m,\eta,\vec{R}}^{(ps-at)}\rangle \quad (\text{inside augmentation}). \quad (2.36)$$

Third, for each  $|\phi_{l,m,\eta,\vec{R}}^{(at)}\rangle$  with eigenenergy  $E_\eta$  there must be a corresponding

---

† The pseudopotential  $V_{eff}^{(ps-at)}(\vec{r})$  differs from the true  $V_{eff}^{(at)}(\vec{r})$  used in (2.31) only inside the augmentation sphere. At the boundary,  $V_{eff}^{(ps-at)}(\vec{r})$  and  $V_{eff}^{(at)}(\vec{r})$  match continuously and differentiably. Inside the augmentation sphere,  $V_{eff}^{(ps-at)}(\vec{r})$  is much smoother than  $V_{eff}^{(at)}$  and lacks the Coulombic divergence at the nucleus.

$|\phi_{l,m,\eta,\vec{R}}^{(ps-at)}\rangle$  with the same  $E_\eta$ . Fourth, outside the augmentation sphere

$$|\phi_{l,m,\eta,\vec{R}}^{(ps-at)}\rangle = |\phi_{l,m,\eta,\vec{R}}^{(at)}\rangle \quad (\text{outside augmentation}). \quad (2.37)$$

Table 2.1 summarizes the properties of the atomic and pseudo-atomic wave functions.

	$ \phi_{l,m,\eta,\vec{R}}^{(at)}\rangle$	$ \phi_{l,m,\eta,\vec{R}}^{(ps-at)}\rangle$
satisfies...	$H^{(at)} \phi_{l,m,\eta,\vec{R}}^{(at)}\rangle = E_\eta \phi_{l,m,\eta,\vec{R}}^{(at)}\rangle$	$H^{(ps-at)} \phi_{l,m,\eta,\vec{R}}^{(ps-at)}\rangle = E_\eta \phi_{l,m,\eta,\vec{R}}^{(ps-at)}\rangle$
augmentation:	$\sum_{l,m,\eta,\vec{R}} a_{l,m,\eta,\vec{R}}^{n,\vec{k}}  \phi_{l,m,\eta,\vec{R}}^{(at)}\rangle =  \Psi_{n,\vec{k}}\rangle$	$\sum_{l,m,\eta,\vec{R}} a_{l,m,\eta,\vec{R}}^{n,\vec{k}}  \phi_{l,m,\eta,\vec{R}}^{(ps-at)}\rangle =  \psi_{n,\vec{k}}^{(PW)}\rangle$
interstitial:	$ \phi_{l,m,\eta,\vec{R}}^{(at)}\rangle =  \phi_{l,m,\eta,\vec{R}}^{(ps-at)}\rangle$	$ \phi_{l,m,\eta,\vec{R}}^{(ps-at)}\rangle =  \phi_{l,m,\eta,\vec{R}}^{(at)}\rangle$

**TABLE 2.1** Summary of the properties of  $|\phi_{l,m,\eta,\vec{R}}^{(at)}\rangle$  and  $|\phi_{l,m,\eta,\vec{R}}^{(ps-at)}\rangle$  and their relationships with each other as well as with the total wave function  $|\Psi_{n,\vec{k}}\rangle$  and the plane wave part  $|\psi_{n,\vec{k}}^{(PW)}\rangle$ . The equations listed in the left column (from top to bottom) are equations (2.31), (2.32), and (2.37). The equations listed in the right column (from top to bottom) are equations (2.35), (2.36), and (2.37).

Armed with this new set of functions  $\{|\phi_{l,m,\eta,\vec{R}}^{(ps-at)}\rangle\}$ , we can now write the PAW ansatz as

$$|\Psi_{n,\vec{k}}\rangle = \sum_{\vec{G}} c_{n,\vec{k}+\vec{G}} |\vec{k} + \vec{G}\rangle + \sum_{l,m,\eta,\vec{R}} a_{l,m,\eta,\vec{R}}^{n,\vec{k}} \left( |\phi_{l,m,\eta,\vec{R}}^{(at)}\rangle - |\phi_{l,m,\eta,\vec{R}}^{(ps-at)}\rangle \right). \quad (2.38)$$

In the interstitial region  $|\phi_{l,m,\eta,\vec{R}}^{(ps-at)}\rangle = |\phi_{l,m,\eta,\vec{R}}^{(at)}\rangle$  and, therefore, the complete wave function reduces to

$$|\Psi_{n,\vec{k}}\rangle = \sum_{\vec{G}} c_{n,\vec{k}+\vec{G}} e^{i(\vec{k}+\vec{G})\cdot(\vec{r})} = |\psi_{n,\vec{k}}^{(PW)}\rangle. \quad (2.39)$$

Likewise, in the augmentation regions,

$$|\psi_{n,\vec{k}}^{(PW)}\rangle = \sum_{l,m,\eta,\vec{R}} a_{l,m,\eta,\vec{R}}^{n,\vec{k}} |\phi_{l,m,\eta,\vec{R}}^{(ps-at)}\rangle \quad (\text{in augmentation region}) \quad (2.40)$$

and so here the total wave function reduces to

$$|\Psi_{n,\vec{k}}\rangle = \sum_{l,m,\eta,\vec{R}} a_{l,m,\eta,\vec{R}}^{n,\vec{k}} |\phi_{l,m,\eta,\vec{R}}^{(at)}\rangle. \quad (2.41)$$

To summarize, a simple superposition of the plane wave function  $|\psi_{n,\vec{k}}^{(PW)}\rangle$ , and the set of pseudo-atomic and atomic wave functions  $\{|\phi_{l,m,\eta,\vec{R}}^{(ps-at)}\rangle, |\phi_{l,m,\eta,\vec{R}}^{(at)}\rangle\}$  yields a complete wave function  $|\Psi_{n,\vec{k}}\rangle$  which is composed exclusively of plane waves in the interstitial region and exclusively of atomic wave functions in the augmentation (core) region.

#### Projector functions $|\tilde{p}_{l,m,\eta,\vec{R}}\rangle$

In order to use the PAW ansatz we must construct a practical method for determining the coefficients  $a_{l,m,\eta,\vec{R}}^{n,\vec{k}}$ . In “augmentation” methods, such as LMTO and LAPW, a similar problem occurs. In these methods, the wave function inside the augmentation region is expanded, just as in PAW, in terms of atomic (or atomic-like) orbitals. In these methods the coefficients in this expansion are found by matching value and derivative of the augmentation and interstitial wave functions at the augmentation-interstitial boundary. The result is a continuous and differentiable wave function which satisfies the Schrödinger equation in all regions. Unfortunately, the mathematical machinery involved in insuring that the total wave function be properly formed is rather involved. PAW uses an alternative method that is formally simpler and avoids some of the pitfalls of the LMTO and LAPW methods. In PAW, there is no explicit matching of wave functions at

the augmentation-interstitial boundary. Instead, the expansion coefficients  $a_{l,m,\eta,\bar{R}}^{n,\bar{k}}$  are found by evaluating the overlap integral between the interstitial wave function  $|\psi_{n,\bar{k}}^{(PW)}\rangle$  and the “projector” function  $|\tilde{p}_{l,m,\eta,\bar{R}}\rangle$ :

$$a_{l,m,\eta,\bar{R}}^{n,\bar{k}} = \langle \tilde{p}_{l,m,\eta,\bar{R}} | \psi_{n,\bar{k}}^{(PW)} \rangle. \quad (2.42)$$

The projector functions are essentially mathematical constructs which form a convenient bridge between the augmentation and interstitial regions. Unlike the atomic and pseudo-atomic wave functions  $|\phi_{l,m,\eta,\bar{R}}^{(at)}\rangle$  and  $|\phi_{l,m,\eta,\bar{R}}^{(ps-at)}\rangle$ , the projector functions have no obvious physical interpretation and so are difficult to motivate. However, their place in the PAW formalism should become clearer in the discussion that follows.

The projector functions are defined to satisfy three conditions. First, for each pair  $\{|\phi_{l,m,\eta,\bar{R}}^{(at)}\rangle, |\phi_{l,m,\eta,\bar{R}}^{(ps-at)}\rangle\}$  there must be a corresponding projector function  $|\tilde{p}_{l,m,\eta,\bar{R}}\rangle$ . Second, the pseudo-atomic and projector functions must together satisfy the PAW “completeness” relation:

$$\sum_{l,m,\eta} |\phi_{l,m,\eta,\bar{R}}^{(ps-at)}\rangle \langle \tilde{p}_{l,m,\eta,\bar{R}}| = 1. \quad (2.43)$$

Finally, these functions must satisfy the PAW “orthogonality” relation:

$$\langle \tilde{p}_{l,m,\eta} | \phi_{l',m',\eta'}^{(ps-at)} \rangle = \delta_{l,m,\eta;l',m',\eta'}. \quad (2.44)$$

If we expand the plane wave part of the wave function  $|\psi_{n,\bar{k}}^{(PW)}\rangle$  in the augmentation region using (2.43), the result is

$$|\psi_{n,\bar{k}}^{(PW)}\rangle = \sum_{l,m,\eta,\bar{R}} \left[ |\phi_{l,m,\eta,\bar{R}}^{(ps-at)}\rangle \langle \tilde{p}_{l,m,\eta,\bar{R}}| \right] |\psi_{n,\bar{k}}^{(PW)}\rangle = \sum_{l,m,\eta,\bar{R}} \langle \tilde{p}_{l,m,\eta,\bar{R}} | \psi_{n,\bar{k}}^{(PW)} \rangle |\phi_{l,m,\eta,\bar{R}}^{(ps-at)}\rangle. \quad (2.45)$$

Now recall equation (2.36):

$$|\psi_{n,\vec{k}}^{(PW)}\rangle = \sum_{l,m,\eta,\vec{R}} a_{l,m,\eta,\vec{R}}^{n,\vec{k}} |\phi_{l,m,\eta,\vec{R}}^{(ps-at)}\rangle \quad (\text{inside augmentation}), \quad (2.36)$$

If we compare the two equations (2.45) and (2.36), then it becomes obvious that the expansion coefficients  $a_{l,m,\eta,\vec{R}}^{n,\vec{k}}$  are given by the overlap integrals between the interstitial wave function  $|\psi_{n,\vec{k}}^{(PW)}\rangle$  and the “projector” functions  $|\tilde{p}_{l,m,\eta,\vec{R}}\rangle$ :

$$a_{l,m,\eta,\vec{R}}^{n,\vec{k}} = \langle \tilde{p}_{l,m,\eta,\vec{R}} | \psi_{n,\vec{k}}^{(PW)} \rangle. \quad (2.42)$$

Finally, we can write down the complete PAW wave function:

$$|\Psi_{n,\vec{k}}\rangle = |\psi_{n,\vec{k}}^{(PW)}\rangle + \sum_{l,m,\eta,\vec{R}} \langle \tilde{p}_{l,m,\eta,\vec{R}} | \psi_{n,\vec{k}}^{(PW)} \rangle \left[ |\phi_{l,m,\eta,\vec{R}}^{(at)}\rangle - |\phi_{l,m,\eta,\vec{R}}^{(ps-at)}\rangle \right]. \quad (2.46)$$

The structure of the PAW basis set is summarized in Table 2.2.

## 2.7 Construction of $|\phi^{(ps-at)}\rangle$ , $|\phi^{(ps-at)}\rangle$ , and $|\tilde{p}\rangle$

Before we move on to the derivations of the PAW formulas for the electron density, total energy, etc., we briefly specify the construction of the PAW basis set.

In this section, all atoms are assumed to be at the origin and so we will omit the position vector  $\vec{R}$  in the set of wave function indices:  $\{l, m, \eta, \vec{R}\} \rightarrow \{l, m, \eta\}$ .

$ \tilde{p}_{l,m,\eta,\bar{R}}\rangle$ satisfies ...	$\sum_{l,m,\eta}  \phi_{l,m,\eta,\bar{R}}^{(ps-at)}\rangle \langle \tilde{p}_{l,m,\eta,\bar{R}}  = 1 \quad (2.43)$
	$\langle \tilde{p}_{l,m,\eta,\bar{R}}   \phi_{l',m',\eta',\bar{R}}^{(ps-at)} \rangle = \delta_{l,m,\eta;l',m',\eta'} \quad (2.44)$
augmentation:	$ \Psi_{n,\bar{k}}\rangle = \sum_{l,m,\eta,\bar{R}} \langle \tilde{p}_{l,m,\eta,\bar{R}}   \psi_{n,\bar{k}}^{(PW)} \rangle  \phi_{l,m,\eta,\bar{R}}^{(at)}\rangle \quad (2.41)$
	$ \psi_{n,\bar{k}}^{(PW)}\rangle = \sum_{l,m,\eta,\bar{R}} \langle \tilde{p}_{l,m,\eta,\bar{R}}   \psi_{n,\bar{k}}^{(PW)} \rangle  \phi_{l,m,\eta,\bar{R}}^{(ps-at)}\rangle \quad (2.45)$
interstitial:	$ \Psi_{n,\bar{k}}\rangle =  \psi_{n,\bar{k}}^{(PW)}\rangle \quad (2.39)$
	$ \phi_{l,m,\eta,\bar{R}}^{(at)}\rangle =  \phi_{l,m,\eta,\bar{R}}^{(ps-at)}\rangle \quad (2.37)$
everywhere:	$ \Psi_{n,\bar{k}}\rangle =  \psi_{n,\bar{k}}^{(PW)}\rangle$
	$+ \sum_{l,m,\eta,\bar{R}} \langle \tilde{p}_{l,m,\eta,\bar{R}}   \psi_{n,\bar{k}}^{(PW)} \rangle  \phi_{l,m,\eta,\bar{R}}^{(at)}\rangle \quad (2.46)$
	$- \sum_{l,m,\eta,\bar{R}} \langle \tilde{p}_{l,m,\eta,\bar{R}}   \psi_{n,\bar{k}}^{(PW)} \rangle  \phi_{l,m,\eta,\bar{R}}^{(ps-at)}\rangle$

**TABLE 2.2** Summary of the properties of  $|\phi_{l,m,\eta,\bar{R}}^{(at)}\rangle$ ,  $|\phi_{l,m,\eta,\bar{R}}^{(ps-at)}\rangle$ , and  $|\tilde{p}_{l,m,\eta,\bar{R}}\rangle$  and their relationships with each other as well as with the total wave function  $|\Psi_{n,\bar{k}}\rangle$  and the plane wave part  $|\psi_{n,\bar{k}}^{(PW)}\rangle$ .

Formation of the initial atomic wave functions  $|\phi_{init;l,m,\eta}^{(at)}\rangle$

The first step in the construction of the basis set is the calculation of the atomic wave functions:  $|\phi_{l,m,\eta}^{(at)}\rangle$ . We do this by solving the Schrödinger equation for an isolated DFT-LDA atom in its ground state:

$$\left[-\frac{1}{2}\nabla^2 + V_{eff}^{(at)}(\vec{r})\right]|\phi_{l,m,\eta}^{(at)}\rangle = E_{\eta}|\phi_{l,m,\eta}^{(ps-at)}\rangle. \quad (2.35)$$

In the current implementation, only valence states are retained in the basis set; in the spirit of the “frozen core” approximation, core states enter the PAW calculation only as a core electron density  $\hat{n}^{(at)}$ .<sup>†</sup> At this stage, the initial set  $\{|\phi_{l,m,\eta}^{(at)}\rangle\}$  includes only the bound valence states. Later on, if test calculations indicate that the basis set formed from just the bound states is incapable of accurately reproducing the physics of the real atom, then additional states may be added to the initial set.

#### Formation of initial pseudo-atomic wave functions $|\phi_{init;l,m,\eta}^{(ps-at)}\rangle$

The DFT-LDA atom is used to construct the local pseudopotential  $V_{eff}^{(ps-local)}(r)$ . In the current implementation, a rather simple method for pseudopotential generation is employed. For atoms with d-electrons, we fit an even polynomial of fourth order to the self-consistent atomic potential  $V_{eff}^{(at)}$  such that outside the augmentation radius  $V_{eff}^{(ps-local)}$  differs from  $V_{eff}^{(at)}$  by less than  $10^{-6}$  Hartrees. The value  $V_{eff}^{(ps-local)}(r=0)$  is set by hand.<sup>‡</sup> For atoms without d-electrons, the local pseudopotential is given by

$$V_{eff}^{(ps-local)}(r) = V_{eff}^{(ps-local)}(0)e^{-(r/r_k)^\lambda} + [1 - e^{-(r/r_k)^\lambda}]V_{eff}^{(at)}(r). \quad (2.47)$$

The values of  $r_k$  and  $\lambda$  are chosen so that in the interstitial region  $V_{eff}^{(ps-local)}$  differs from  $V_{eff}^{(at)}$  by less than  $10^{-6}$  Hartrees. Typically the value of  $\lambda$  is in the range 3-6.

For atoms which have a small HOMO-LUMO gap\* and for which pseudopotentials

<sup>†</sup> Of course, a “soft core” complete with self-consistently calculated core wave functions could be used in the PAW method without any formal changes to the theory. However, such changes would require significant programming effort and typically produce only small changes on the order of 1 meV per atom<sup>20</sup> in the final result.

<sup>‡</sup> Small optimizations of the scattering properties and/or elimination of ghost states can be accomplished by adjusting  $V_{eff}^{(ps-local)}(r=0)$ .

\* The difference between the energy of the highest occupied molecular orbital (HOMO) and the lowest unoccupied molecular orbital (LUMO).

work well, a low value of  $\lambda$  works well.<sup>26</sup> For Ga, which falls into this category, we use a value for  $\lambda$  of 2.5. For As, we use a value for  $\lambda$  of 6. Once a value of  $\lambda$  has been chosen, the value  $r_k$  can be determined. Typically, a value of 95% of the covalent radius is a good first choice. If  $V_{eff}^{(ps-local)}$  and  $V_{eff}^{(at)}$  do not agree outside the augmentation region, this value can always be decreased. Everything else being equal, using a smaller value of  $\lambda$  tends to force  $r_k$  towards smaller values.

Next we form the nonlocal pseudopotentials

$$w_{l,\eta}(r) = V_{eff}^{(ps-local)}(r) + b_{l,\eta} e^{-(r/r_{kl\eta})^\lambda}. \quad (2.48)$$

The initial pseudo-atomic wave functions  $|\phi_{init;l,m,\eta}^{(ps-at)}\rangle$  are the solutions of the equation

$$\left[-\frac{1}{2}\nabla^2 + w_{l,\eta}(r)\right]|\phi_{init;l,m,\eta}^{(ps-at)}\rangle = E_\eta|\phi_{init;l,m,\eta}^{(ps-at)}\rangle. \quad (2.49)$$

The values of  $b_{l,\eta}$  and  $r_{kl\eta}$  in equation (2.48) are chosen such that the logarithmic derivatives of the wave functions, defined as

$$D_{l,\eta}(\epsilon) = r \left. \frac{[\partial\phi_{l,\eta}(r, \epsilon)/\partial r]}{\phi_{l,\eta}(r, \epsilon)} \right|_{r_0}, \quad (2.50)$$

differ by less than 0.001% at points outside the augmentation region. The cutoff radii  $r_{kl\eta}$  are particular to each pair  $\{l, \eta\}$  and provide a useful extra degree of freedom which can be exploited to optimize the pseudopotential. A value of 75% of the covalent radius usually works well for the  $r_{kl\eta}$ 's. In general, we try to use the same value for all the  $r_{kl\eta}$ 's for a given atom. However, particular wave functions sometimes require special treatment. This was the case for the  $s$  wave function of As. Initially, a value of  $r_{ks} = 1.3$  Bohr was tried for the As atomic setup. Unfortunately, this choice resulted in insufficient agreement between  $\phi_{l=0,\eta}^{(ps-at)}$  and  $\phi_{l=0,\eta}^{(at)}$  outside



the augmentation region and so  $r_{ks}$  was reduced to 1.2 Bohr. However, the choice  $r_{kp} = r_{kd} = 1.3 \text{ Bohr}$  was found to be appropriate for the  $p$  and  $d$  states (see figure 2.5).

One final point should be emphasized. Everything else being equal, a large augmentation region tends to reduce the size of the Hamiltonian matrix used in actual PAW calculations. On the other hand, smaller augmentation regions result in a PAW atom that more accurately reflects the physics of the original atom. The construction of the pseudopotential used to create PAW atomic setups is a complex balancing act between these two competing priorities.

Examples of the local and nonlocal pseudopotentials for Ga and As are shown in figures 2.2 and 2.3.

#### Formation of initial projector functions $|\tilde{p}_{init;l,m,\eta}\rangle$

Apart from satisfying the conditions expressed in equations (2.43) and (2.44), the form of the projector functions is completely arbitrary. The particular method we used to construct the projector functions results in functions which are localized to the augmentation regions. We begin by forming an initial projector function:

$$|\tilde{p}_{init;l,m,\eta}\rangle = \left[-\frac{1}{2}\nabla^2 + V_{eff}^{(at)}(\vec{r}) - E_\eta\right]|\phi_{init;l,m,\eta}^{(at)}\rangle. \quad (2.51)$$

If the resultant  $|\tilde{p}_{init;l,m,\eta}\rangle = 0$ , then we use

$$|\tilde{p}_{init;l,m,\eta}\rangle = e^{-(r/r_k)^\lambda}. \quad (2.52)$$

Next, we must modify these  $|\tilde{p}_{init;l,m,\eta}\rangle$ 's so that the resultant  $|\tilde{p}_{l,m,\eta}\rangle$ 's satisfy

$$\langle \tilde{p}_{l,m,\eta} | \phi_{l',m',\eta'}^{(ps-at)} \rangle = \delta_{l,m,\eta;l',m',\eta'}. \quad (2.44)$$

### All-electron potential and pseudopotential of Ga

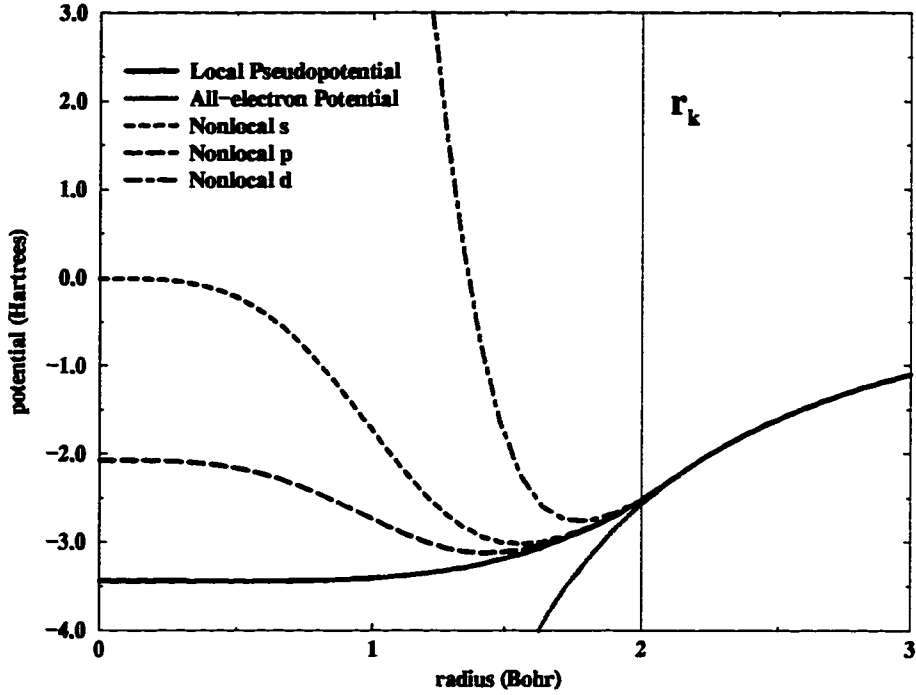


**FIGURE 2.2** All-electron potential  $V_{eff}^{(at)}$ , local potential  $V_{eff}^{(ps-local)}$ , and nonlocal  $w_{l,\eta}$  pseudopotentials for the PAW gallium atomic setup used in the calculations. The cutoff parameter  $r_k$  is 2 Bohr and is indicated by the light vertical line. The value of  $\lambda$  is set to 3.5. The value of  $V_{eff}^{(ps-local)}$  at the origin is -3.44. The non-local d-pseudopotential rises to a plateau at around 23 Hartrees and has a flat slope at the origin.

### All-electron potential and pseudopotential for As

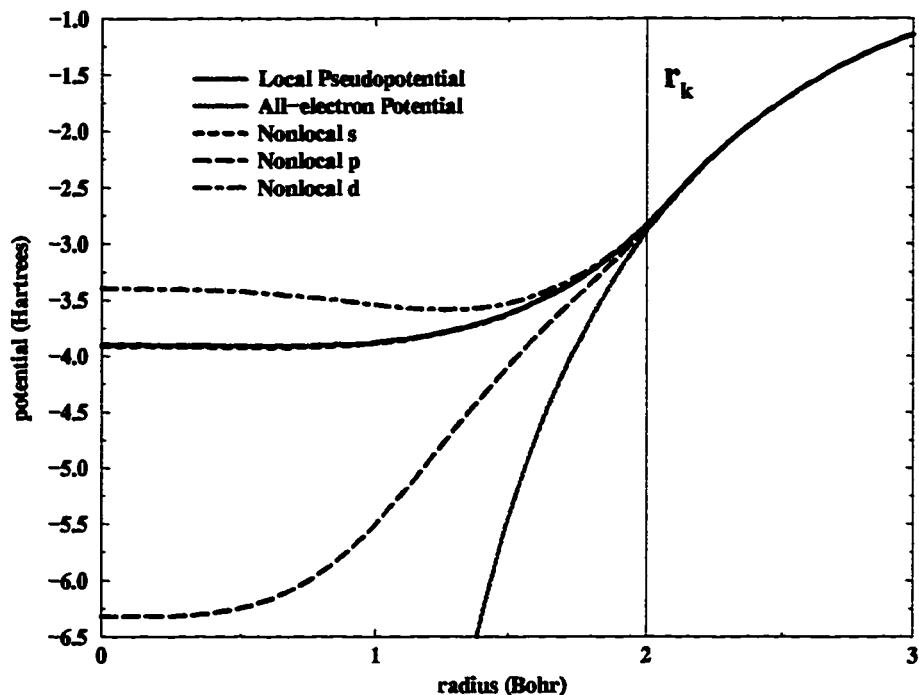


**FIGURE 2.3** All-electron potential  $V_{eff}^{(at)}$ , local pseudopotential  $V_{eff}^{(ps-local)}$ , and nonlocal  $w_{l,\eta}$  pseudopotentials for the PAW arsenic atomic setup used in the ground state calculations. The cutoff parameter  $r_k$  is 2 Bohr and is indicated by the light vertical line. The value of  $V_{eff}^{(ps-local)}$  at the origin is -3.90.

Since the  $|\phi^{(at)}\rangle$ 's,  $|\phi^{(ps-at)}\rangle$ 's, and  $|\tilde{p}\rangle$ 's are related by equations (2.37), (2.43), and (2.44), a modification of the  $|\tilde{p}\rangle$ 's necessitates a corresponding modification of the  $|\phi^{(at)}\rangle$ 's and  $|\phi^{(ps-at)}\rangle$ 's. A simple iterative technique is used to perform these transformations. In the following, the index set  $\{l, m, \eta\}$  is replaced by a single index:  $\{l, m, \eta\} \rightarrow i$ . We begin with the first elements in the basis set. These functions need no modification beyond insuring that the condition  $\langle \tilde{p}_i | \phi_i^{(ps-at)} \rangle = 1$  is satisfied:

$$|\tilde{p}_1\rangle = \frac{1}{\sqrt{\langle \tilde{p}_{init;1} | \phi_1^{(ps-at)} \rangle}} |\tilde{p}_{init;1}\rangle, \quad (2.53)$$

$$|\phi_1^{(ps-at)}\rangle = \frac{1}{\sqrt{\langle \tilde{p}_{init;1} | \phi_1^{(ps-at)} \rangle}} |\phi_{init;1}^{(ps-at)}\rangle, \quad (2.54)$$

$$|\phi_1^{(at)}\rangle = \frac{1}{\sqrt{\langle \tilde{p}_{init;1} | \phi_1^{(ps-at)} \rangle}} |\phi_{init;1}^{(at)}\rangle. \quad (2.55)$$

The second projector is formed by simply subtracting out that part of  $|\tilde{p}_1\rangle$  which is not orthogonal to the original  $|\tilde{p}_{init;2}\rangle$ :

$$|\tilde{p}_2\rangle = |\tilde{p}_{init;2}\rangle - |\tilde{p}_1\rangle \langle \phi_1^{(ps-at)} | \tilde{p}_1 \rangle, \quad (2.56)$$

and then normalizing as in equation (2.53). Likewise,  $|\phi_2^{(ps-at)}\rangle$ , and  $|\phi_2^{(at)}\rangle$  are formed via

$$|\phi_2^{(ps-at)}\rangle = |\phi_{init;2}^{(ps-at)}\rangle - \langle \phi_1^{(ps-at)} | \tilde{p}_1 \rangle |\phi_1^{(ps-at)}\rangle, \quad (2.57)$$

$$|\phi_2^{(at)}\rangle = |\phi_{init;2}^{(at)}\rangle - \langle \phi_1^{(at)} | \tilde{p}_1 \rangle |\phi_1^{(at)}\rangle, \quad (2.58)$$

followed by normalization as in equations (2.53), (2.54), and (2.55), respectively. Each succeeding set  $\{|\phi_i^{(at)}\rangle, |\phi_i^{(ps-at)}\rangle, |\tilde{p}_i\rangle\}$  is formed via

$$|\tilde{p}_i\rangle = |\tilde{p}_{init;i}\rangle - \sum_{j=1}^{j=i-1} |\tilde{p}_j\rangle \langle \phi_j^{(ps-at)} | \tilde{p}_j \rangle, \quad (2.59)$$

$$|\phi_i^{(ps-at)}\rangle = |\phi_{init;i}^{(ps-at)}\rangle - \sum_{j=1}^{j=i-1} \langle \phi_j^{(ps-at)} | \tilde{p}_j \rangle |\phi_j^{(ps-at)}\rangle, \quad (2.60)$$

$$|\phi_i^{(at)}\rangle = |\phi_{init;i}^{(at)}\rangle - \sum_{j=1}^{j=i-1} \langle \phi_j^{(at)} | \tilde{p}_j \rangle |\phi_j^{(at)}\rangle, \quad (2.61)$$

followed by normalization as in equations (2.53), (2.54), and (2.55), respectively. Examples of the atomic, pseudo-atomic, and projector functions for gallium and arsenic are shown in figures 2.4 and 2.5. These graphs show the distinctive features of the various functions. First note that the atomic wave functions  $|\phi^{(at)}\rangle$  exhibit high frequency spatial oscillations in the augmentation region. In contrast, the pseudo-atomic wave functions  $|\phi^{(ps-at)}\rangle$  are smoothly varying, even in the vicinity of the nucleus. The projector functions shown here exhibit two interesting properties. First, they decay rapidly to zero outside the augmentation region; this simplifies the division of the total wave function into augmentation and interstitial parts. Second, they are fairly smooth, resulting in a Fourier expansion

$$\tilde{p}(\vec{r}) = \sum_{\vec{G}} \langle \vec{G} | \tilde{p} \rangle e^{i\vec{G}\cdot\vec{r}}, \quad (2.62)$$

whose high frequency components are small. This in turn results in low plane wave cutoff for the full PAW calculation. While not a feature of all PAW atomic setups, this low plane wave cutoff *is* a feature of the PAW setups used in this work.

### Checking the basis set: logarithmic derivatives

Once an initial basis set has been formed, a quick calculation is performed to check the electron scattering properties of the resultant PAW atom. If the basis set formed from just the bound states is found to be incapable of accurately reproducing the electron scattering properties of the real atom, then additional states are added

### Partial waves and projectors for Ga

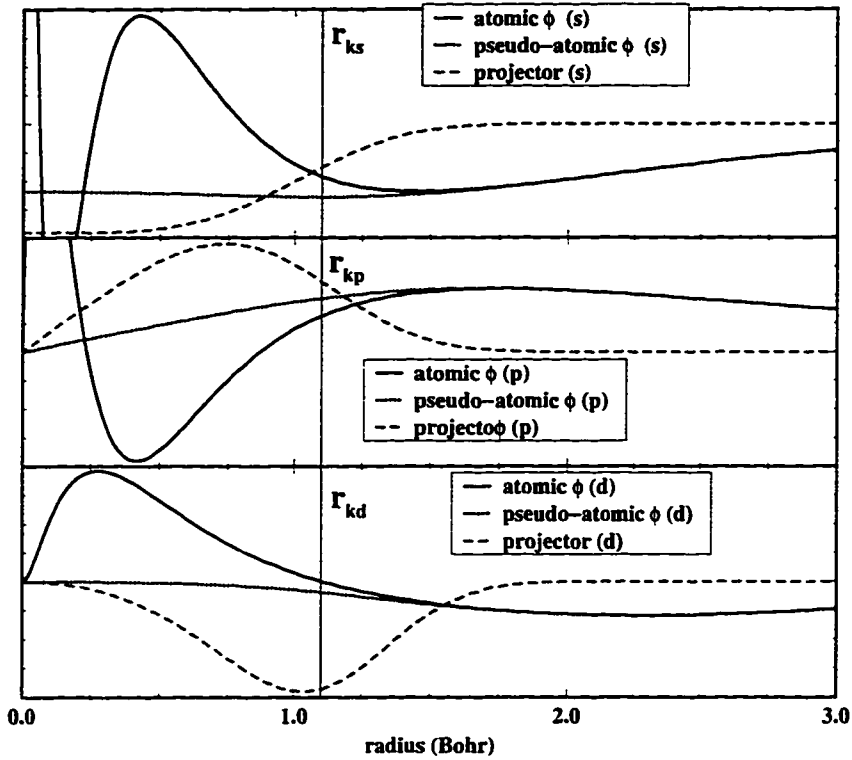


**FIGURE 2.4** All-electron atomic wave functions  $|\phi_{l,m,\eta,\vec{R}}^{(at)}\rangle$ , the pseudo-atomic wave functions  $|\phi_{l,m,\eta,\vec{R}}^{(ps-at)}\rangle$ , and the projector functions  $|\tilde{p}_{l,m,\eta,\vec{R}}\rangle$  in the PAW atomic setup for Ga. This particular PAW basis has only one projector per  $l$ . The  $l = 0$  ( $s$ ) wave functions are plotted in the top graph, the  $l = 1$  ( $p$ ) wave functions in the middle and the  $l = 2$  ( $d$ ) wave functions at the bottom. The cutoff parameters for each angular momentum  $r_{kl}$  are shown on the graph for reference. Note that outside 2 Bohr the atomic and pseudo-atomic wave functions coincide and the projector functions are zero. Finally, observe that the pseudo-atomic wave functions are slowly varying and have no nodes while the atomic wave functions are rapidly varying and have several nodes.

### Partial waves and projectors for As

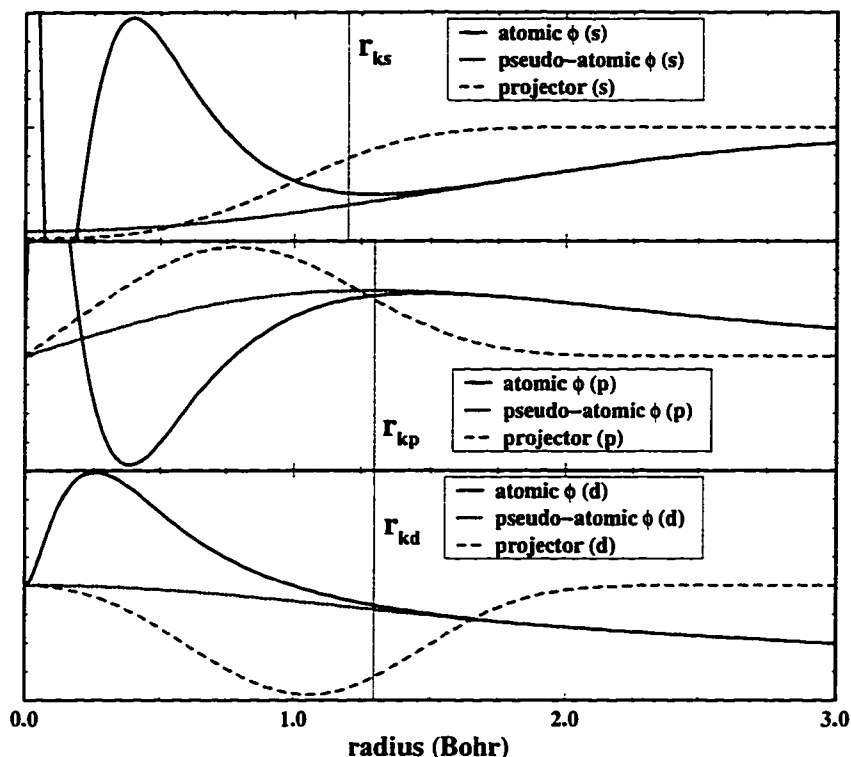


**FIGURE 2.5** All-electron atomic wave functions  $|\phi_{l,m,\eta,\vec{R}}^{(at)}\rangle$ , the pseudo-atomic wave functions,  $|\phi_{l,m,\eta,\vec{R}}^{(ps-at)}\rangle$ , and the projector functions  $|\tilde{p}_{l,m,\eta,\vec{R}}\rangle$  in the PAW atomic setup for As. This particular PAW basis has only one projector per  $l$ . The  $l = 0$  ( $s$ ) wave functions are plotted in the top graph, the  $l = 1$  ( $p$ ) wave functions in the middle and the  $l = 2$  ( $d$ ) wave functions at the bottom. The cutoff parameters for each angular momentum  $r_{kl}$  are shown on the graph for reference. Note that outside 2 Bohr the atomic and pseudo-atomic wave functions coincide and the projector functions are zero. Finally, observe the differences between the pseudo-atomic and atomic wave functions: the pseudo-atomic wave functions are slowly varying and have no nodes while the atomic wave functions are rapidly varying and have several nodes.

to the initial set. A good measure of the electron scattering properties is the logarithmic derivative, defined as

$$D_l(\epsilon) = r \left. \frac{[\partial \phi_l(r, \epsilon) / \partial r]}{\phi_l(r, \epsilon)} \right|_{r_0}. \quad (2.50)$$

The point  $r_0$  at which the log derivative is calculated is usually chosen to be a small distance outside the augmentation sphere. If, for a given  $l$  state, an additional wave function is needed, the energy  $E_{l,\eta'}$  of this new state is taken to be the energy at which  $D_l$ , calculated within the PAW formalism, begins to significantly depart from the correct behavior. Figs. 2.6 and 2.7 show the logarithmic derivatives for the gallium and arsenic atomic setups used in the ground state calculations in this thesis. Note that agreement is very good over a nearly 2 Hartree range.

## 2.8 Operators in PAW

The PAW wave function (equation (2.46)) can be rewritten in the operator form

$$|\Psi_{n,\vec{k}}\rangle = \left[ 1 + \sum_{l,m,\eta,\vec{R}} \left( |\phi_{l,m,\eta,\vec{R}}^{(at)}\rangle - |\phi_{l,m,\eta,\vec{R}}^{(ps-at)}\rangle \right) \langle \bar{p}_{l,m,\eta,\vec{R}} | \right] |\psi_{n,\vec{k}}^{(PW)}\rangle = T |\psi_{n,\vec{k}}^{(PW)}\rangle. \quad (2.63)$$

The operator  $T$  essentially forms a bridge between the “physical” Hilbert space spanned by the true wave functions  $|\Psi\rangle$  and the “PAW” Hilbert space spanned by the plane wave part of the PAW wave function  $|\psi^{(PW)}\rangle$ . An operator in the PAW



Logarithmic derivative of Ga  
PAW versus direct calculation

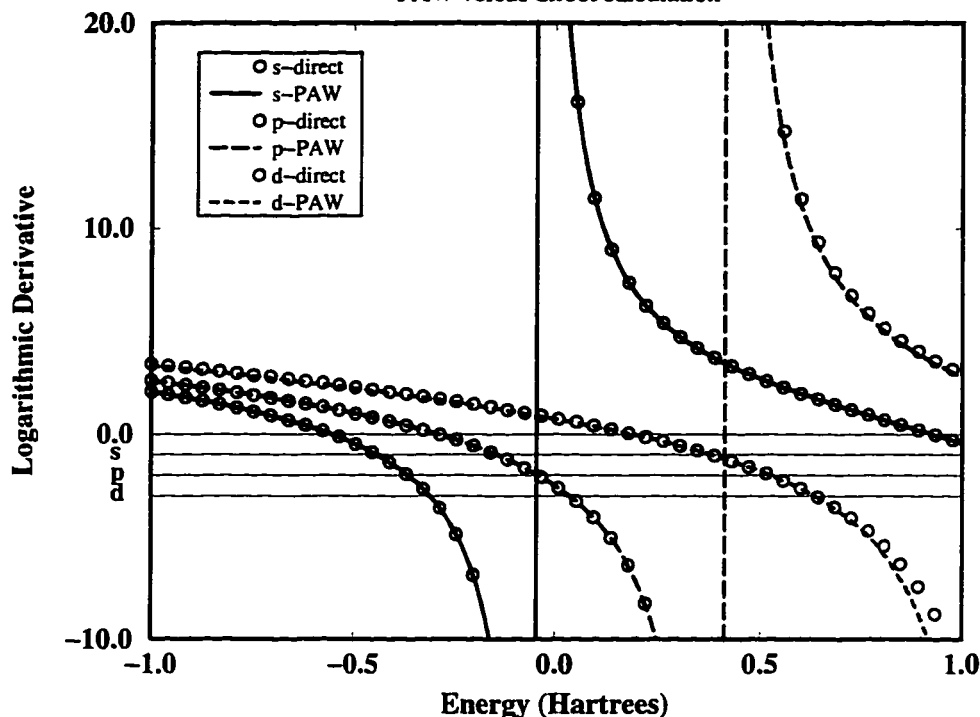


**FIGURE 2.6** The logarithmic derivative function  $D_l(\epsilon) = r\partial \ln(\phi_l(r, \epsilon))/\partial r$  for the PAW gallium atomic setup used in the ground state calculations. The circles denote the all-electron values for  $D_l(\epsilon)$  while the curves represent  $D_l(\epsilon)$  as calculated using the PAW atomic wave function basis set. The  $E_\eta$  for the  $s$ - and  $p$ -states are the bound state values:  $-0.3349$  Hartrees and  $-0.1000$  Hartrees. The  $E_\eta$  for the (unoccupied)  $d$ -state is chosen to be  $0.5$  Hartrees. This value was chosen rather than the bound state value of  $0.01718$  Hartrees in order to improve performance at higher energies. Tests confirmed that performance at low energies was unaffected. The logarithmic derivative was evaluated at  $r_0 = 3$  Bohr. The horizontal lines at  $D_l = -1, -2, -3$  (labeled on the graph by the letters  $s, p,$  and  $d$ ) are the positions of the centers of the unhybridized  $s$ -,  $p$ -, and  $d$ -bands.

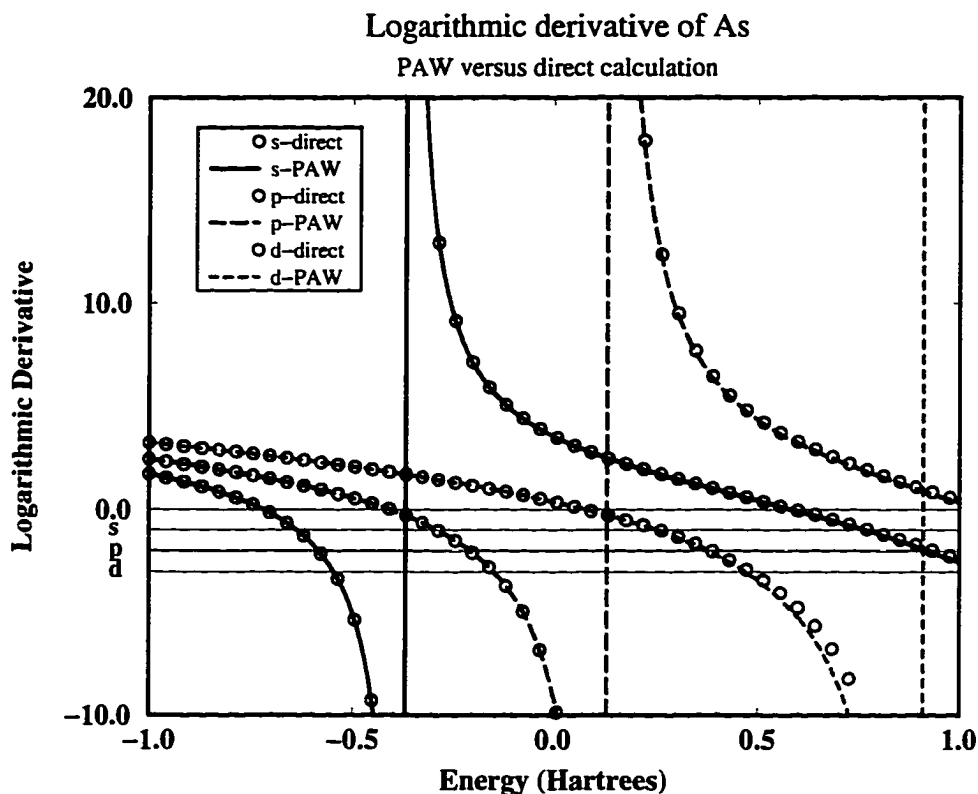


**FIGURE 2.7** The logarithmic derivatives  $D_l(\epsilon) = r \partial \ln(\phi_l(r, \epsilon)) / \partial r$  for the PAW arsenic atomic setup used in the ground state calculations. The circles denote the all-electron values for  $D_l(\epsilon)$  while the curves represent  $D_l(\epsilon)$  as calculated using the PAW atomic wave function basis set. The  $E_\eta$  for the  $s$ - and  $p$ -states are the bound state values:  $-0.5380$  Hartrees and  $-0.1955$  Hartrees. The  $E_\eta$  for the (unoccupied)  $d$ -state was chosen to be  $-0.1$  Hartrees; this value was chosen rather than the ground state value of  $0.0446$  Hartrees because the resulting PAW atomic setup had a marginally lower plane wave cutoff. The logarithmic derivative was evaluated at  $r_0 = 3$  Bohr. The horizontal lines at  $D_l = -1, -2, -3$  (labeled on the graph by the the letters  $s, p,$  and  $d$ ) are the positions of the centers of the unhybridized  $s$ -,  $p$ -, and  $d$ -bands.

space is related to the equivalent operator in the physical Hilbert space:

$$\begin{aligned}
A^{(PAW)} &= T^\dagger A T \\
&= \left[ 1 + \sum_{l,m,\eta,\bar{R}} |\tilde{p}_{l,m,\eta,\bar{R}}\rangle \left( \langle \phi_{l,m,\eta,\bar{R}}^{(at)} | - \langle \phi_{l,m,\eta,\bar{R}}^{(ps-at)} | \right) \right] A \\
&\quad \times \left[ 1 + \sum_{l',m',\eta',\bar{R}'} \left( |\phi_{l',m',\eta',\bar{R}'}^{(at)}\rangle - |\phi_{l',m',\eta',\bar{R}'}^{(ps-at)}\rangle \right) \langle \tilde{p}_{l',m',\eta',\bar{R}'} | \right].
\end{aligned} \tag{2.64}$$

Using the properties of the PAW basis set, this equation can be simplified. First, since

$$|\phi_{l,m,\eta,\bar{R}}^{(ps-at)}\rangle = |\phi_{l,m,\eta,\bar{R}}^{(at)}\rangle \quad (\text{outside augmentation}), \tag{2.37}$$

we need consider only on-site terms. Multiplying out and using the collective indices  $i$  and  $j$  in place of  $\{l, m, \eta\}$  and  $\{l', m', \eta'\}$ , we get

$$\begin{aligned}
A^{(PAW)} &= A \\
&+ \sum_{\bar{R}} \sum_j A \left( |\phi_{j,\bar{R}}^{(at)}\rangle - |\phi_{j,\bar{R}}^{(ps-at)}\rangle \right) \langle \tilde{p}_{j,\bar{R}} | \\
&+ \sum_{\bar{R}} \sum_i |\tilde{p}_{i,\bar{R}}\rangle \left( \langle \phi_{i,\bar{R}}^{(at)} | - \langle \phi_{i,\bar{R}}^{(ps-at)} | \right) A \\
&- \sum_{\bar{R}} \sum_{i,j} |\tilde{p}_{i,\bar{R}}\rangle \left( \langle \phi_{i,\bar{R}}^{(at)} | A | \phi_{j,\bar{R}}^{(ps-at)} \rangle + \langle \phi_{i,\bar{R}}^{(ps-at)} | A | \phi_{j,\bar{R}}^{(at)} \rangle \right) \langle \tilde{p}_{j,\bar{R}} | \\
&+ \sum_{\bar{R}} \sum_{i,j} |\tilde{p}_{i,\bar{R}}\rangle \left( \langle \phi_{i,\bar{R}}^{(at)} | A | \phi_{j,\bar{R}}^{(at)} \rangle + \langle \phi_{i,\bar{R}}^{(ps-at)} | A | \phi_{j,\bar{R}}^{(ps-at)} \rangle \right) \langle \tilde{p}_{j,\bar{R}} |.
\end{aligned} \tag{2.65}$$

After applying the condition

$$\sum_{l,m,\eta} |\phi_{l,m,\eta,\bar{R}}^{(ps-at)}\rangle \langle \tilde{p}_{l,m,\eta,\bar{R}} | = 1. \tag{2.43}$$

in lines 2 and 3 of the equation (2.65), we get

$$\begin{aligned}
A^{(PAW)} &= A \\
&+ \sum_{\vec{R}} \sum_{i,j} |\tilde{p}_{i,\vec{R}}\rangle \left( \langle \phi_{i,\vec{R}}^{(ps-at)} | A | \phi_{j,\vec{R}}^{(at)} \rangle - \langle \phi_{i,\vec{R}}^{(ps-at)} | A | \phi_{j,\vec{R}}^{(ps-at)} \rangle \right) \langle \tilde{p}_{j,\vec{R}} | \\
&+ \sum_{\vec{R}} \sum_{i,j} |\tilde{p}_{i,\vec{R}}\rangle \left( \langle \phi_{i,\vec{R}}^{(at)} | A | \phi_{j,\vec{R}}^{(ps-at)} \rangle - \langle \phi_{i,\vec{R}}^{(ps-at)} | A | \phi_{j,\vec{R}}^{(ps-at)} \rangle \right) \langle \tilde{p}_{j,\vec{R}} | \\
&- \sum_{\vec{R}} \sum_{i,j} |\tilde{p}_{i,\vec{R}}\rangle \left( \langle \phi_{i,\vec{R}}^{(at)} | A | \phi_{j,\vec{R}}^{(ps-at)} \rangle + \langle \phi_{i,\vec{R}}^{(ps-at)} | A | \phi_{j,\vec{R}}^{(at)} \rangle \right) \langle \tilde{p}_{j,\vec{R}} | \\
&+ \sum_{\vec{R}} \sum_{i,j} |\tilde{p}_{i,\vec{R}}\rangle \left( \langle \phi_{i,\vec{R}}^{(at)} | A | \phi_{j,\vec{R}}^{(at)} \rangle + \langle \phi_{i,\vec{R}}^{(ps-at)} | A | \phi_{j,\vec{R}}^{(ps-at)} \rangle \right) \langle \tilde{p}_{j,\vec{R}} |.
\end{aligned} \tag{2.66}$$

Canceling like terms we get the final formula for operators in the PAW formalism:

$$A^{(PAW)} = A + \sum_{\vec{R}} \sum_{i,j} |\tilde{p}_{i,\vec{R}}\rangle \left( \langle \phi_{i,\vec{R}}^{(at)} | A | \phi_{j,\vec{R}}^{(at)} \rangle - \langle \phi_{i,\vec{R}}^{(ps-at)} | A | \phi_{j,\vec{R}}^{(ps-at)} \rangle \right) \langle \tilde{p}_{j,\vec{R}} |. \tag{2.67}$$

## 2.9 Electron Density, Total Energy and Hamiltonian

Given equation (2.67), we can now derive the equations for the electron density  $n(\vec{r})$ , the total energy  $E[\{\Psi_i; \vec{R}\}]$ , and the Hamiltonian and overlap operators,  $H$  and  $O$ . In this section, the index set  $\{l, m, \eta, \vec{R}\}$  will be replaced by the collective index  $i$  (or  $j$ ).

Since the total electron density is merely

$$n(r) = \sum_{n,\vec{k}} \langle \Psi_{n,\vec{k}} | r \rangle f_n \langle r | \Psi_{n,\vec{k}} \rangle, \tag{2.68}$$

to find the correct formula for the electron density we just need to substitute the

operator  $|r\rangle f_n \langle r|$  for  $A$  in equation (2.65):

$$\begin{aligned}
n(r) = \sum_{n, \vec{k}} f_n \langle \Psi_{n, \vec{k}} | r \rangle \langle r | \Psi_{n, \vec{k}} \rangle &= \overbrace{\sum f_n \langle \psi_{n, \vec{k}}^{(PW)} | r \rangle \langle r | \psi_{n, \vec{k}}^{(PW)} \rangle}^{n^{(PW)}} \\
&+ \overbrace{\sum_{n, \vec{k}, i, j} f_n \langle \psi_{n, \vec{k}}^{(PW)} | \tilde{p}_i \rangle \langle \phi_i^{(at)} | r \rangle \langle r | \phi_j^{(at)} \rangle \langle \tilde{p}_j | \psi_{n, \vec{k}}^{(PW)} \rangle}^{n^{(at)}} \\
&- \overbrace{\sum_{n, \vec{k}, i, j} f_n \langle \psi_{n, \vec{k}}^{(PW)} | \tilde{p}_i \rangle \langle \phi_i^{(ps-at)} | r \rangle \langle r | \phi_j^{(ps-at)} \rangle \langle \tilde{p}_j | \psi_{n, \vec{k}}^{(PW)} \rangle}^{n^{(ps-at)}}.
\end{aligned} \tag{2.69}$$

Note that the electron density neatly divides into three components: plane wave, atomic and pseudo-atomic. These components are related in much the same way that the the components of the wave function are related:

$$n^{(PW)} = n^{(ps-at)} \quad (\text{inside augmentation}), \tag{2.70}$$

$$n^{(at)} = n^{(ps-at)} \quad (\text{outside augmentation}), \tag{2.71}$$

$$n = n^{(at)} \quad (\text{inside augmentation}). \tag{2.72}$$

The derivation of the total energy is somewhat more involved but is conceptually no different. The kinetic energy part is formed by substituting the standard kinetic energy operator  $-\frac{1}{2}\nabla^2$  for  $A$  in equation (2.65):

$$\begin{aligned}
\text{K.E.} &= \overbrace{\sum_n f_n \langle \psi_n^{(PW)} | -\frac{1}{2}\nabla^2 | \psi_n^{(PW)} \rangle}^{(PW)} \\
&+ \overbrace{\sum_{n, i, j} f_n \langle \psi_n^{(PW)} | \tilde{p}_i \rangle \langle \phi_i^{(atom)} | -\frac{1}{2}\nabla^2 | \phi_j^{(atom)} \rangle \langle \tilde{p}_j | \psi_n^{(PW)} \rangle}^{(at)} \\
&- \overbrace{\sum_{n, i, j} f_n \langle \psi_n^{(PW)} | \tilde{p}_i \rangle \langle \phi_i^{(ps-atom)} | -\frac{1}{2}\nabla^2 | \phi_j^{(ps-atom)} \rangle \langle \tilde{p}_j | \psi_n^{(PW)} \rangle}^{(ps-at)}.
\end{aligned} \tag{2.73}$$

The Hartree potential part of the total energy functional can be written as

$$E_{Hartree} = \frac{1}{2} \int d^3r \int d^3r' \frac{[n^{(PW)} + n^{(at)} - n^{(ps-at)} + n^Z][n^{(PW)} + n^{(at)} - n^{(ps-at)} + n^Z]}{|\vec{r} - \vec{r}'|}, \quad (2.74)$$

where  $n^Z$  is the potential due to the atomic nuclei. Ideally, we would like to write  $E_{Hartree}$  as a sum of three separate terms:  $E_{Hartree}^{(PW)}$ ,  $E_{Hartree}^{(at)}$ , and  $E_{Hartree}^{(ps-at)}$ . Unfortunately, this is difficult to do since the charge inside the augmentation spheres interacts with the charge in the interstitial region. We can get around this problem by introducing the ‘‘compensation charge density’’  $\hat{n}$ , which is simply an expansion of  $(n^{(at)} + n^Z - n^{(ps-at)})$  inside the augmentation spheres. After adding  $\hat{n}$  to both  $n^{(PW)}$  and  $(n^{(at)} + n^Z)$  and regrouping terms, the result is

$$\begin{aligned} n &= n^{(PW)} + (n^{(at)} + n^Z) + n^{(ps-at)} \\ &= (n^{(PW)} + \hat{n}) + (n^{(at)} + n^Z) - (n^{(ps-at)} + \hat{n}). \end{aligned} \quad (2.75)$$

Since the difference  $[(n^{(at)} + n^Z) - (n^{(ps-at)} + \hat{n})]$  is exactly zero by the definition of  $\hat{n}$ , it is no longer necessary to explicitly include the augmentation-interstitial interaction in the integration in equation (2.74). The result is

$$\begin{aligned} E_{Hartree} &= \frac{1}{2} \int_{aug} d^3r \int_{aug} d^3r' \frac{[(n^{(at)} + n^Z) - (n^{(ps-at)} + \hat{n})][(n^{(at)} + n^Z) - (n^{(ps-at)} + \hat{n})]}{|\vec{r} - \vec{r}'|} \\ &\quad + \frac{1}{2} \int_{total V} d^3r \int_{total V} d^3r' \frac{[n^{(PW)} + \hat{n}][n^{(PW)} + \hat{n}]}{|\vec{r} - \vec{r}'|}. \end{aligned} \quad (2.76)$$

After separating the atomic and pseudo-atomic parts, we get the final answer

$$\begin{aligned}
E_{Hartree} &= E_{Hartree}^{(PW)} + E_{Hartree}^{(at)} - E_{Hartree}^{(ps-at)} \\
&= \frac{1}{2} \int_{total V} d^3r \int_{total V} d^3r' \frac{[n^{(PW)} + \hat{n}][n^{(PW)} + \hat{n}]}{|\vec{r} - \vec{r}'|} \\
&\quad + \frac{1}{2} \int_{aug} d^3r \int_{aug} d^3r' \frac{[n^{(at)} + n^Z][n^{(at)} + n^Z]}{|\vec{r} - \vec{r}'|} \\
&\quad - \frac{1}{2} \int_{aug} d^3r \int_{aug} d^3r' \frac{[n^{(ps-at)}][n^{(ps-at)}]}{|\vec{r} - \vec{r}'|}.
\end{aligned} \tag{2.77}$$

The PAW version of the total exchange-correlation energy can be derived from the standard form ( equation (2.10)), using only the properties of the components of the electron density expressed in equations (2.70), (2.71), and (2.72):

$$\begin{aligned}
E_{XC} &= E_{XC}^{(PW)} + E_{XC}^{(at)} - E_{XC}^{(ps-at)} \\
&= \int_{Total V} d^3r \epsilon_{XC}^{hom}(n^{(PW)}(\vec{r}))n^{(PW)}(\vec{r}) \\
&\quad + \int_{aug} d^3r \epsilon_{XC}^{hom}(n^{(at)}(\vec{r}))n^{(at)}(\vec{r}) \\
&\quad - \int_{aug} d^3r \epsilon_{XC}^{hom}(n^{(ps-at)}(\vec{r}))n^{(ps-at)}(\vec{r}).
\end{aligned} \tag{2.78}$$

Putting this all together, the final formula for the total energy is

$$E = E^{(PW)} + E^{(at)} - E^{(ps-at)}, \tag{2.79}$$

where the separate components are given by

$$\begin{aligned}
E^{(PW)} &= \sum_n f_n \langle \psi_n^{(PW)} | -\frac{1}{2} \nabla^2 | \psi_n^{(PW)} \rangle \\
&\quad + \frac{1}{2} \int dV \int dV' \frac{[n^{(PW)} + \hat{n}][n^{(PW)} + \hat{n}]}{|\vec{r} - \vec{r}'|} \\
&\quad + \int dV n^{(PW)}(\vec{r}) \epsilon_{XC}(n^{(PW)}(\vec{r})),
\end{aligned} \tag{2.80}$$

$$\begin{aligned}
E^{(ps-at)} &= \sum_{n,i,j} f_n \langle \psi_n^{(PW)} | \tilde{p}_i \rangle \langle \phi_i^{(ps-at)} | -\frac{1}{2} \nabla^2 | \phi_j^{(ps-at)} \rangle \langle \tilde{p}_j | \psi_n^{(ps)} \rangle \\
&\quad + \frac{1}{2} \int dV \int dV' \frac{[n^{(ps-at)} + \hat{n}][n^{(ps-at)} + \hat{n}]}{|\vec{r} - \vec{r}'|} \\
&\quad + \int dV n^{(ps-at)}(\vec{r}) \epsilon_{XC}(n^{(ps-at)}(\vec{r})),
\end{aligned} \tag{2.81}$$

$$\begin{aligned}
E^{(at)} &= \sum_{n,i,j} f_n \langle \psi_n^{(PW)} | \tilde{p}_i \rangle \langle \phi_i^{(at)} | -\frac{1}{2} \nabla^2 | \phi_j^{(at)} \rangle \langle \tilde{p}_j | \psi_n^{(PW)} \rangle \\
&\quad + \frac{1}{2} \int dV \int dV' \frac{[n^{(at)} + n^Z][n^{(at)} + n^Z]}{|\vec{r} - \vec{r}'|} \\
&\quad + \int dV n^{(at)}(\vec{r}) \epsilon_{XC}(n^{(at)}(\vec{r})).
\end{aligned} \tag{2.82}$$

The derivation of the overlap operator  $O$  is trivial. We simply replace  $A$  in equation (2.65) with identity:

$$O^{(PAW)} = 1 + \sum_i \sum_j |\tilde{p}_i\rangle \left( \langle \phi_i^{(at)} | \phi_j^{(ps-at)} \rangle - \langle \phi_i^{(ps-at)} | \phi_j^{(ps-at)} \rangle \right) \langle \tilde{p}_j|. \tag{2.83}$$

The kinetic energy part of the Hamiltonian follows from equation (2.65):

$$\begin{aligned}
\hat{T} &= -\frac{1}{2} \nabla^2 \\
&\quad + \sum_i \sum_j |\tilde{p}_i\rangle \left( \langle \phi_i^{(at)} | -\frac{1}{2} \nabla^2 | \phi_j^{(ps-at)} \rangle - \langle \phi_i^{(ps-at)} | -\frac{1}{2} \nabla^2 | \phi_j^{(ps-at)} \rangle \right) \langle \tilde{p}_j|.
\end{aligned} \tag{2.84}$$

The potential part of the Hamiltonian is tedious but straightforward to derive. We merely need to recognize that the potential operator is

$$\hat{V}_{eff} = |r\rangle \frac{\partial E_V}{\partial n(\vec{r})} \langle r|, \tag{2.85}$$

where  $E_V$  is just the potential part of the total energy. Inserting this operator in equation (2.65) and adding in the kinetic energy term, the result is

$$\begin{aligned}
H &= -\frac{1}{2} \nabla^2 + V_{eff}^{(PW)} + \sum_i \sum_j |\tilde{p}_i\rangle \left( \langle \phi_i^{(at)} | -\frac{1}{2} \nabla^2 + V_{eff}^{(at)} | \phi_j^{(ps-at)} \rangle \right. \\
&\quad \left. - \langle \phi_i^{(ps-at)} | -\frac{1}{2} \nabla^2 + V_{eff}^{(ps-at)} | \phi_j^{(ps-at)} \rangle \right) \langle \tilde{p}_j|.
\end{aligned} \tag{2.86}$$



where the various potential terms  $V_{eff}^{(PW)}$ ,  $V_{eff}^{(at)}$ , and  $V_{eff}^{(ps-at)}$  are related via

$$V_{eff}^{(PW)} = V_{eff}^{(ps-at)} \quad (\text{inside augmentation}), \quad (2.87)$$

$$V_{eff}^{(at)} = V_{eff}^{(ps-at)} \quad (\text{outside augmentation}), \quad (2.88)$$

$$V_{eff} = V_{eff}^{(at)} \quad (\text{inside augmentation}). \quad (2.89)$$

## CHAPTER 3

### RECONSTRUCTION GEOMETRIES

#### 3.0 Advertisement

This chapter begins with a discussion of the techniques we used to calculate the reconstructed geometries of the GaAs(001)-c(4x4), the GaAs(001)-c(2x2), and the Si(001)-(2x1) surfaces. Due to the large size and complicated physics of surface structures, the computational demands of *ab-initio* calculations of these systems are severe.† As a result, a number of specialized techniques, such as the repeated slab model, have been developed over the years. Some of these techniques will be discussed, with special emphasis on the ones used in this work.

After the discussion of technique, the specifics of the reconstructed geometries will be given in the form of detailed diagrams of the structures as well as 3-dimensional perspective drawings. In all cases, our geometries agree well with

---

† This study required 50,000 node hours on the IBM SP2 parallel supercomputer at The Cornell Theory Center. A node hour is simply an hour on a single processor; a job that uses 8 nodes and runs for 24 hours (wall clock time) would consume  $8 \times 24 = 192$  node hours. In addition, thousands of node hours were consumed on the SP2's at the Maui High Performance Computing Center and at the Ohio Supercomputer Center (OSC). Exact figures for Maui OSC are unavailable as neither site uses CPU accounting.

the published experimental and theoretical data.

The chapter will end with a brief explanation of Pashley's electron counting rule.<sup>27</sup> This rule will be used to explain the stability of our calculated GaAs geometries.

### 3.1 Repeated Slab Model and Surface Termination

For both the GaAs and Si systems the physical semi-infinite surface system was modeled using a unit cell consisting of a thin slab of material, oriented such that the surface plane is parallel to the x-y plane, plus a thin vacuum layer above. Since we used a plane wave based formalism, we must repeat this unit cell periodically in all directions. The result is an infinite superlattice system composed of alternating layers of material and vacuum. For obvious reasons, this approach is known as the repeated slab model (sometimes referred to as the superslab model).<sup>22</sup> The periodic conditions in the x- and y-directions insure that the system does not deform outwards (that is, in the x- and y-directions). The system is free to relax in the z-direction.

The precise implementation of the repeated slab method varies considerably from researcher to researcher; however, there are some common threads. Typically, a few layers of the unit cell are held fixed at the bulk lattice positions in order to impose the bulk geometry on the system. There are basically two choices for the placement of these fixed atoms. First, the fixed layers can be placed at the center of the slab. In this case, the reconstruction under study is usually duplicated on each side of the slab. To increase computational speed, such a two-sided unit cell is usually constructed to take advantage of symmetry considerations.<sup>28</sup> This type

of slab has the advantage that possible electrostatic interactions between slabs are lessened or eliminated. However, if symmetry considerations cannot be used to limit the size of the calculation then the use of a two-sided slab results in a duplication of computational effort.† As the current implementation of PAW does not take advantage of symmetry, a two-sided slab was rejected for the GaAs calculations detailed in this work. On the other hand, our Si unit cell is much smaller than the GaAs unit cell and so we used a two-sided slab for the Si calculations.

The second choice for the placement of the stationary layers is to put them on one side of the slab. In order for this method to work well this “bottom” surface must not interact strongly with the “top” side of the slab where the reconstruction of interest is found. This condition can usually be met if the surface has the following characteristics. First, the surface should contain no partially filled bonding orbitals, which might result in hard to predict effects on the electronic structure of the complete structure. Second, the surface must be non-polar in order to eliminate electrostatic interactions between surfaces. A number of candidates for this bottom termination surface have been suggested over the years. One particularly novel technique has been put forward by Shiraishi;<sup>12,29</sup> He terminates his bottom surface with fictional fractionally charged H atoms. These are non-physical atoms with fractional nuclear charges. The nuclear charge is tailored so that these atoms form perfect covalent bonds with their neighbors, even when their neighbors can only contribute a non-integer number of electrons to a bond. We briefly investigated this option for our GaAs calculations but abandoned it when it became clear that implementing a fictional atom approach would involve large scale modifications of

---

† Actually, depending on the computational method, a cell with an extraneous surface can result in as much as an eight-fold increase in computing time.

PAW. There were also concerns about the unphysical nature of fractionally charged nuclei.

Kaxiras *et al.*<sup>30</sup> has used a method involving fractionally charged Ga atoms which is similar to the Shiraishi fictitious H method. In this method, known as the “skillful slab” technique, the two central layers of a two-sided slab are composed of fictitious Ga atoms whose positions are held fixed. The nuclear charge of these atoms is tailored so that they can form perfect covalent bonds with each other as well as with neighboring As atoms. As a result of this construction, this geometry has inversion symmetry and so there are no artificial electrostatic fields in the vacuum region. This method was rejected for our calculations for the same reasons as for the Shiraishi fictitious H method.

In the end we chose to terminate our surface using the GaAs(001)-c(2x2) reconstruction. This choice was pioneered by Froyen and Zunger<sup>31</sup> and has given them good results in the past. The GaAs(100)-c(2x1) reconstruction has a few properties which make it useful as a terminating surface. First, it is semiconducting with no partially filled bonding orbitals. Second, it is non-polar<sup>32</sup>. Finally, it has the added feature that it is a fairly flat reconstruction, which results in an effective increase in the vacuum region.

### 3.2 Details of Calculation

The geometries of all three structures are shown in figures 3.1-3.7. In all cases, the plane wave cutoff for the wave functions was 5 Hartrees while the k-point integration was performed using 4 k-points in the plane of the surface. Detailed convergence tests were performed with respect to vacuum spacing, slab thickness.

plane wave cutoff, and number of k-points for the GaAs(001)-c(4x4) structure. The details of these tests are given in the appendix. Convergence data from the GaAs(001)-c(4x4) system was extrapolated to the GaAs(001)-c(2x2) system. A smaller series of tests were performed for the Si(001)-(2x1) system. On the basis of these tests, we estimate the error in the difference between total energies of different structures to be no more than 25 meV.

The initial geometry was taken from the available experimental or theoretical data. In the case of the GaAs(001)-c(2x2) reconstruction, initial coordinates were supplied by Froyen.<sup>33</sup> In an additional test, we started from the unrelaxed surface configuration and then optimized the geometry. The two PAW simulations (one starting from Froyen's coordinates and the other starting from the unrelaxed system) agreed well with each other and with Froyen's data. For the Si(001)-(2x1) simulations, a rough guess for the coordinates of a symmetric dimer was used as the initial geometry. For the GaAs(001)-c(2x2) reconstruction, the STM data of Biegelsen *et al.*<sup>34</sup> was used as the initial geometry.

The optimization of the geometry proceeded via the Car-Parrinello method. After the electronic structure for the initial geometry was calculated, the atoms are allowed to move. Initially, an automatic annealing routine is used to optimize the geometry. As the total energy of the system evolves this annealing routine turns on a large effective friction if the total energy increases. If the total energy decreases, a small friction amount of friction is applied and this amount decreases with each successive iteration during which the total energy decreases. The simulation ends automatically when the total energy changes by no more than  $10^{-5}$  Hartrees for 100 atomic time units. After the automatic annealing procedure has finished, a

zero friction simulation is run for a total of 1000 atomic time units. If at the end of this simulation, the total energy shows a variation of less than 0.001 Hartrees then the total energy is considered to be converged. However, the automatic annealing procedure often fails to find the true ground state and further simulations must be run. Typically, a small constant value of friction is used and the simulation is run until the fluctuations in the total energy settle down to less than 0.001 Hartrees. After that a further zero friction run is done. This procedure repeats until convergence is confirmed. In some especially difficult cases, the total simulation time has exceeded  $10^4$  atomic time units.

The geometry of the GaAs(001)-c(2x2) system was calculated using a two-sided seven layer slab (5 full atomic layers capped on both sides by a half-monolayer of Ga). The total height of the (slab)+(vacuum layer) was 26.692392 Bohr (14.125 Å). The lattice constant in the (x-y) plane is taken to be the bulk lattice constant. All atoms in this system were allowed to relax.

The geometry of the GaAs(001)-c(4x4) system was calculated using a slab composed of a terminating GaAs(001)-c(2x2) reconstruction ( a half-monolayer of Ga and a full monolayer of As) followed by 4 atomic layers of GaAs (2 monolayers of Ga and two monolayers of As). The geometry for this layer was taken from the calculation of the GaAs(001)-c(2x2) reconstruction discussed above. The final layer consisted of the six As atoms that form the set of three dimers found in the GaAs(001)-c(4x4). The total height of the (slab)+(vacuum layer) was 32.030871 Bohr (16.95 Å). The lattice constant in the (x-y) plane is taken to be the bulk lattice constant. Only the  $\frac{1}{2}$  layers in the terminating GaAs(001)-c(2x2) reconstruction were held fixed.

The geometry of the Si(001)-(2x1) system was calculated using a two-sided eight layer slab (counting the dimer layers). The total height of the (slab)+(vacuum layer) was 28.218347 Bohr (14.9325 Å). The lattice constant in the (x-y) plane is taken to be the bulk lattice constant. The two central layers were fixed.

### 3.3 Electron Counting Model

Using Pashley's electron counting model,<sup>27</sup> we can decide if a proposed GaAs surface reconstruction should be stable. Pashley's model also allows us to predict if a surface is semiconducting.

The electron counting model is based on a simple chemical analysis of the bonding in a covalent solid. Inside bulk GaAs, the original single  $s$  and three  $p$  orbitals from each Ga and As atom recombine into a set of four hybridized  $sp^3$  orbitals. A bond is formed when one hybridized  $sp^3$  orbital from a Ga atom combines with a hybridized  $sp^3$  orbital from an As atom. In the bulk it is possible to fill completely all the bonding orbitals. However, at the surface some orbitals may be unable to form bonds. The energies of these "dangling" orbitals can be estimated from the energies of the original unhybridized  $s$  and  $p$  orbitals. The reasoning is illustrated in figure 3.8. The energy of the Ga  $sp^3$  orbital is intermediate between the energies of the original unhybridized orbitals. The final result is that the energy of the Ga  $sp^3$  orbital lies in the conduction band of GaAs. Similar reasoning leads to the conclusion that the energy of the As  $sp^3$  orbital lies in the valence band.

Since physical systems always seek their configuration of lowest energy, the surface of GaAs will tend to reconstruct so that all the Ga dangling bonds are empty and all the As dangling bonds are filled. If this condition is satisfied then



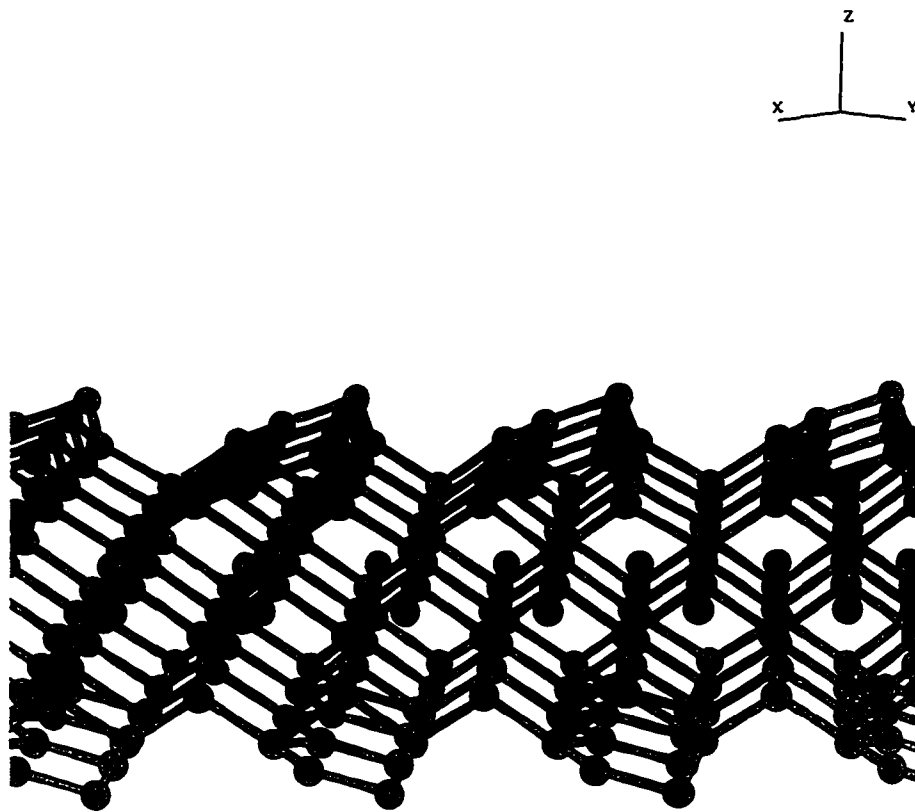


**FIGURE 3.1** Perspective drawing showing the calculated geometry of the Si(001)-(2x1) surface. The slab is terminated on both sides by the same reconstruction. Even though no symmetry constraints were used in the calculation, the reconstructions on either side agree extremely well.

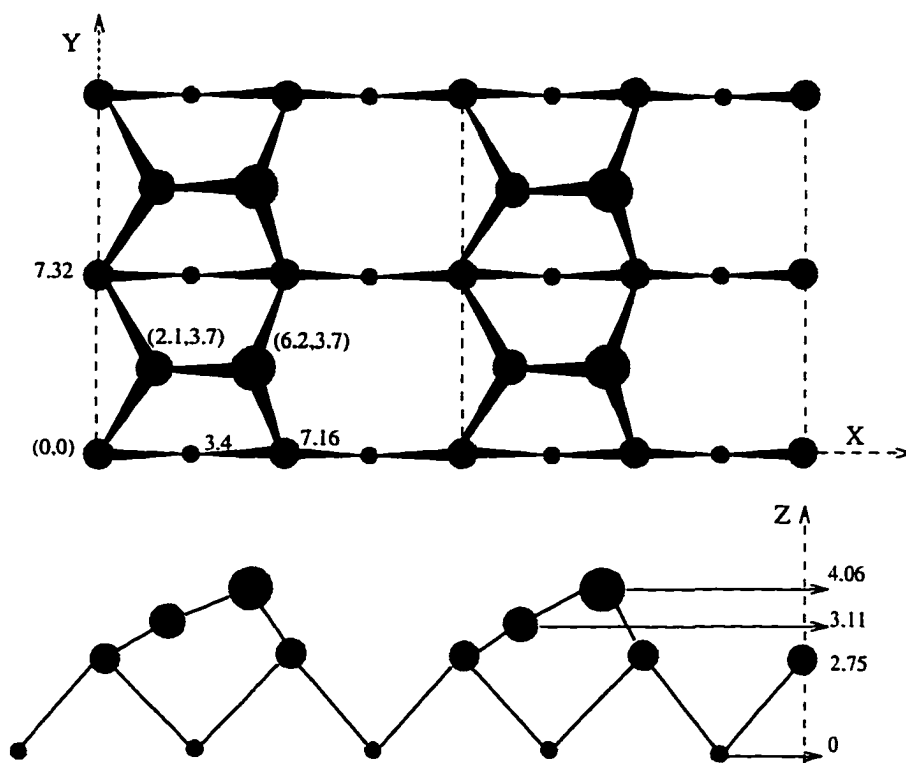


**FIGURE 3.2** Detailed diagram showing the calculated geometry of Si(001)-(2x1) reconstruction. The coordinates are given in Bohr.

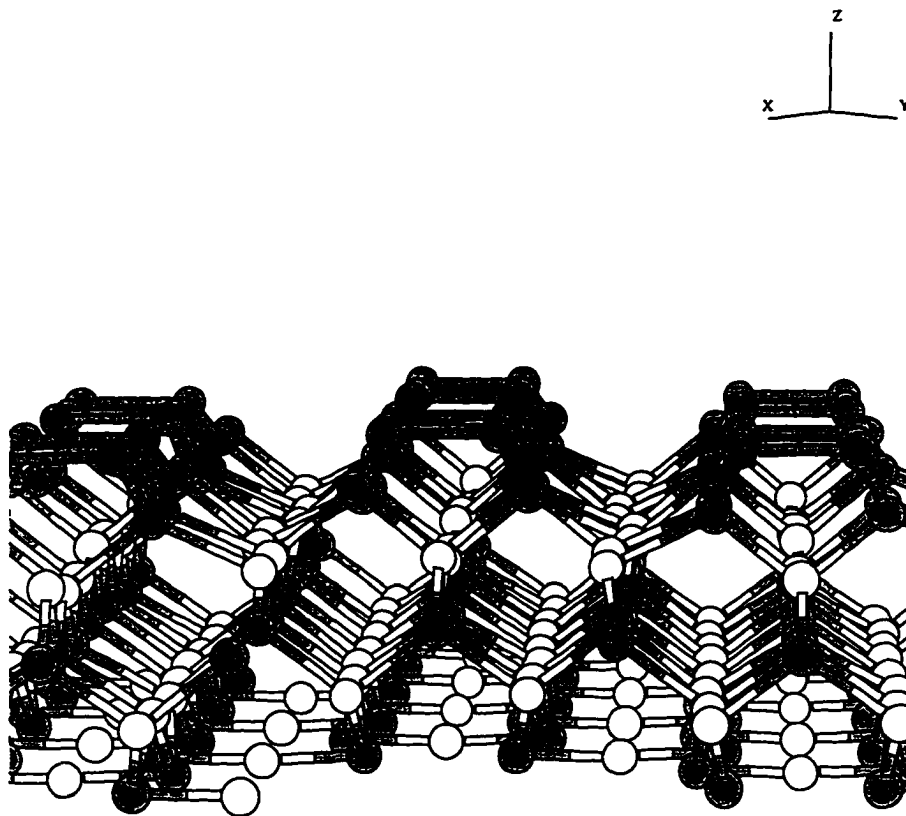


**FIGURE 3.3** Perspective drawing showing the calculated geometry of the GaAs(001)-c(4x4) surface. The slab used for calculations on this surface is terminated on the bottom by the GaAs(001)-c(2x2) reconstructed surface. The As atoms are represented by dark atoms, the Ga atoms by light atoms.

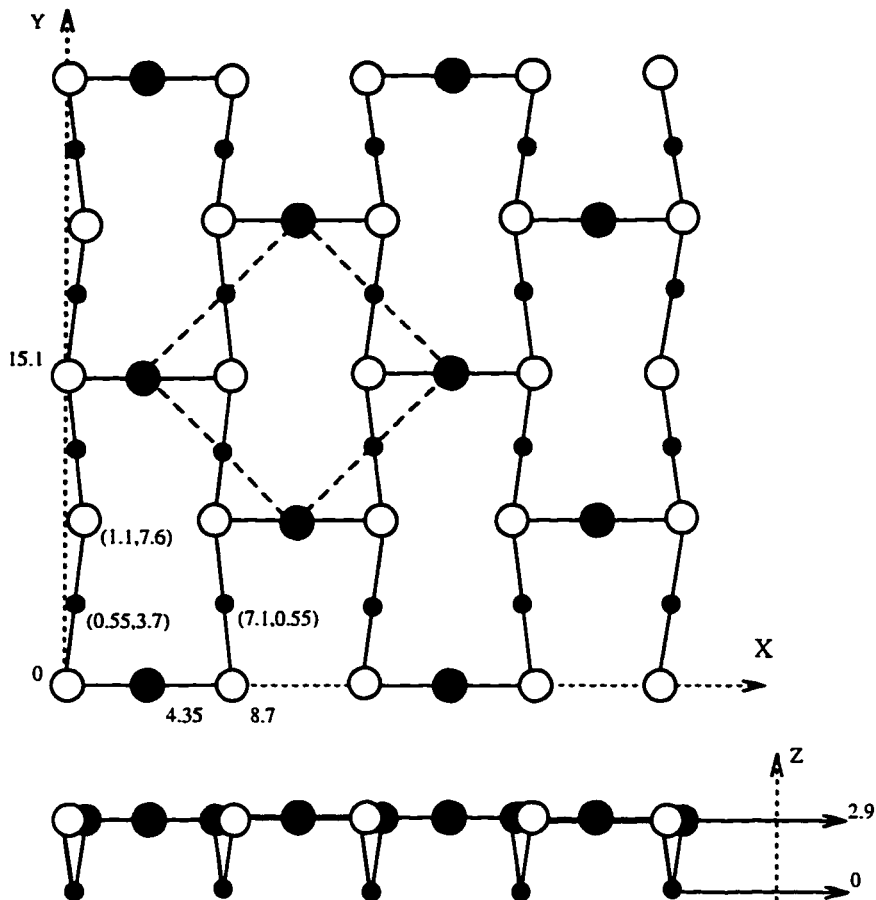


**FIGURE 3.4** Detailed top-view (above) and side-view (below) diagrams showing the calculated geometry of GaAs(001)-c(2x2) reconstruction. This surface was used to terminate the non-interesting side of the GaAs slab. The As atoms are represented by white atoms, the Ga atoms by black atoms. In the side view diagram, As atoms in the background are represented by gray atoms. The coordinates are given in Bohr.

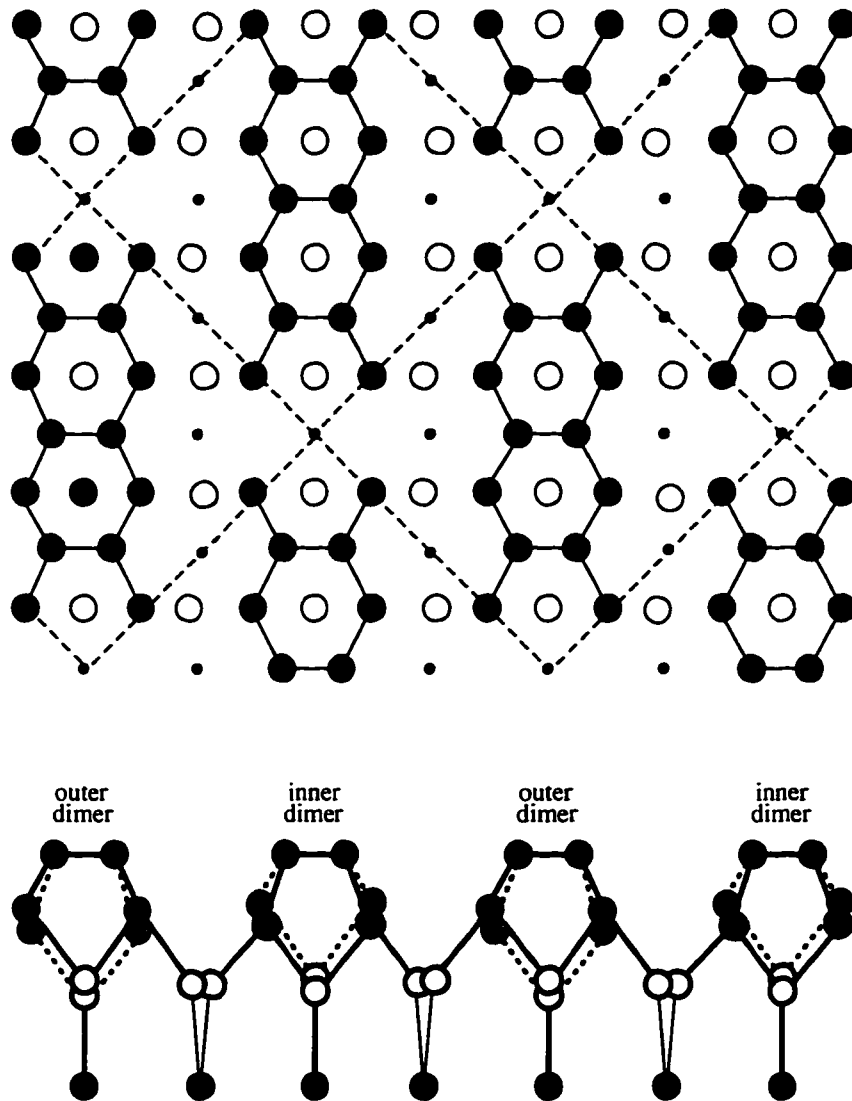


**FIGURE 3.5** Top (above) and side (below) views of the GaAs(001)-c(4x4) reconstructed surface. The As atoms are represented by black atoms, the Ga atoms by white atoms. In the side view, sub-surface As atoms in the background are represented by gray atoms.

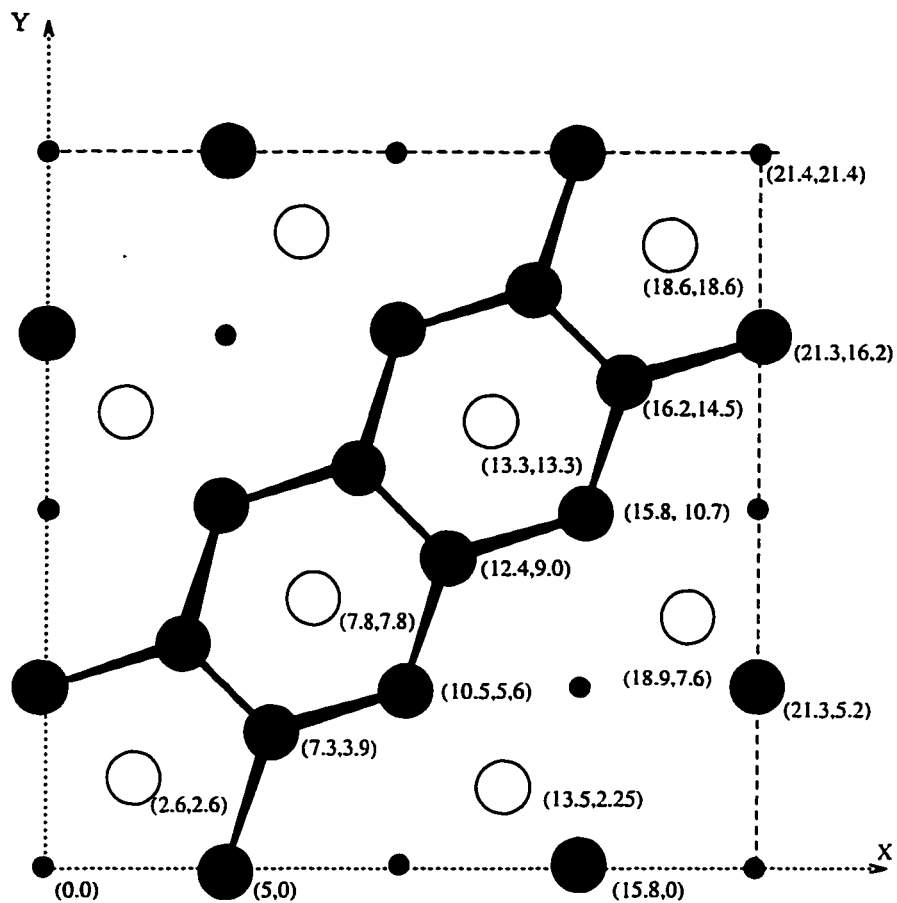


**FIGURE 3.6** Large scale diagram of the GaAs(001)-c(4x4) reconstructed surface (top view). The x-y coordinates are given in Bohrs. The As atoms are represented by black atoms, the Ga atoms by white atoms.

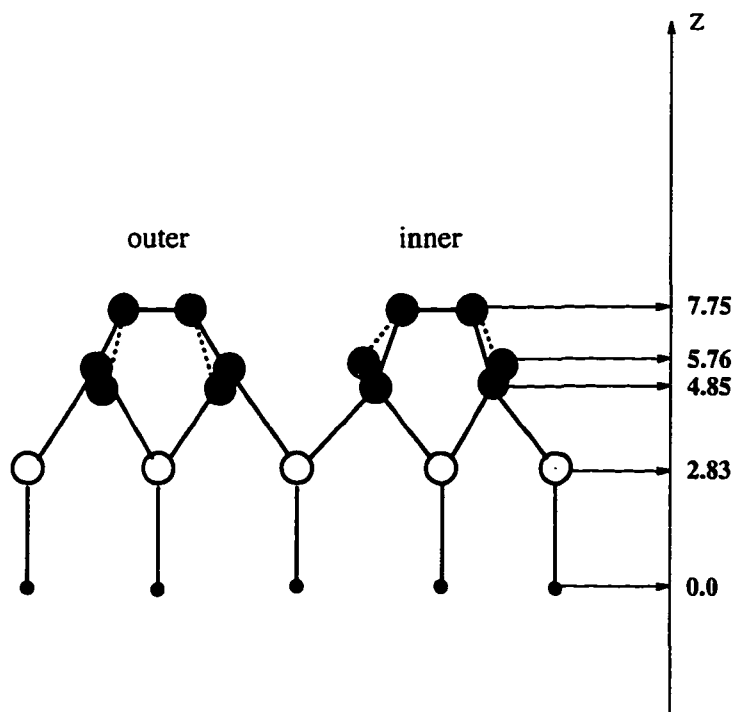


**FIGURE 3.7** Large scale diagram of the GaAs(001)-c(4x4) reconstructed surface (side view). The z-coordinates are given in Bohrs. The As atoms are represented by black atoms, the Ga atoms by white atoms. The subsurface As atoms in the background are represented by gray atoms.

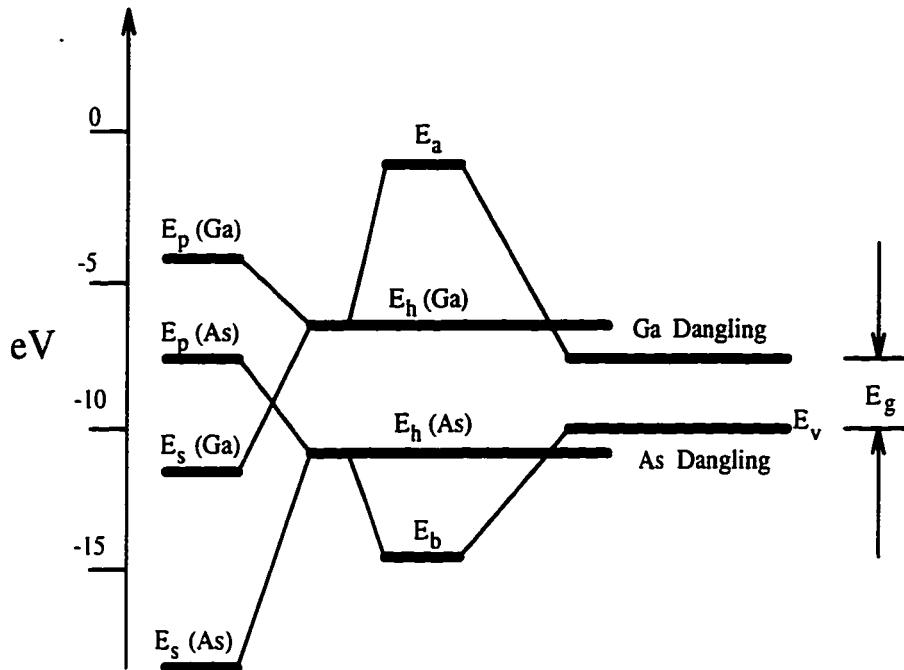


**FIGURE 3.8** Explanation of the electron counting rule. The electron counting model is based on a simple chemical analysis of the bonding in a covalent solid. Inside bulk GaAs, the original single  $s$  and three  $p$  orbitals (levels labeled on the diagram as  $E_p$  and  $E_s$ ) from each Ga and As atom recombine into a set of four hybridized  $sp^3$  orbitals. The levels for these states are labeled as  $E_h$ . A bond is formed when one hybridized  $sp^3$  orbital from a Ga atom combines with a hybridized  $sp^3$  orbital from an As atom. The level of the bonding orbital is labeled as  $E_b$  on the diagram and is in the bulk valence band. In the bulk it is possible to fill completely all the bonding orbitals. However, at the surface some orbitals may be unable to form bonds. The energies of these “dangling” orbitals can be estimated from the energies of the original unhybridized  $s$  and  $p$  orbitals. The final result is that the energy of the Ga  $sp^3$  orbital lies in the conduction band of GaAs. Similar reasoning leads to the conclusion that the energy of the As  $sp^3$  orbital lies in the valence band.



the surface should be semiconducting; partly filled dangling orbitals may lead to a metallic surface.

We can apply these principles to the GaAs(100) surface if we take into account the “numerics” of bonding in GaAs. First, note that, in the bulk, each Ga atom contributes three electrons to a total of four bonds. Therefore, Ga contributes  $\frac{3}{4}$  of an electron to each bond. Likewise, As contributes  $\frac{5}{4}$  of an electron to each bond.

An examination of figure 3.6 shows that the GaAs(100)-c(4x4) obeys the counting model. We begin by noting that the sub-surface Ga atoms (which are denoted by large white circles in figure 3.6) each contribute three electrons to the system. However, only half of these electrons are used in bonds with the surface. Therefore, the eight sub-surface atoms in the surface unit cell contribute a total of  $8 \times \frac{3}{2} = 12$  electrons to the surface. The eight sub-surface As atoms (which are denoted by large black circles in figure 3.5) each contribute five electrons to the system making a total of  $8 \times 5 = 40$  electrons. The six As dimers contribute a total of 30 electrons. The final total is  $12 + 40 + 30 = 82$  electrons involved in bonds on the surface. Next we must count the bonds. There are 16 bonds connecting the sub-surface Ga atoms to the sub-surface As atoms; for the sake of clarity, these bonds were not included in the figure. There are 12 bonds connecting the sub-surface As atoms to the dimer atoms. In addition, each of the sub-surface As atoms adjacent to the missing dimer rows has a dangling orbital. Each of the three dimers accounts for one bond and each of the six atoms that make up the dimers has a dangling orbital. This brings the total of bonds to  $16 + 12 + 4 + 3 + 6 = 41$ , which is just enough absorb the 82 electrons in the system. The conclusion is that the GaAs(100)-c(4x4) should be a stable, semiconducting surface.

## CHAPTER 4

### DIFFUSION OF Ga ADATOMS ON GaAs(100)-c(4x4)

#### 4.0 Introduction

In this chapter we present an *ab-initio* investigation of the diffusion of a single isolated Ga adatom on the GaAs(100)-c(4x4) reconstructed surface.

The GaAs(100)-c(4x4) surface was chosen for this study for several reasons. First of all, since it is difficult to grow smooth films in the c(4x4) regime,<sup>19</sup> this surface is an ideal candidate for this study, which has the stated aim of improving MBE growth techniques. Surfaces growing in the c(4x4) regime typically exhibit rough morphologies and do not produce the RHEED oscillations seen during the growth of smooth epitaxial layers.

Second, this reconstruction has an extremely high As content. In fact, this reconstruction is the most As-rich reconstruction found on the (100) surface.<sup>35</sup> Naturally, given this high As content, the c(4x4) reconstruction is often seen during the growth of GaAs films with excess (1-2%) As. Such films have a couple of interesting properties.<sup>36,37</sup> First, they have very high resistivity, making them ideally suited as a substrate for devices since the high resistance nearly eliminates

interaction between neighboring devices. This allows for much increased device density. Second, As-rich GaAs films have excellent crystallinity and so subsequent GaAs layers of high quality can be grown on top of it.

Third, the  $c(4 \times 4)$  reconstruction is quite large. As a result, the calculations discussed here provide us with an excellent large-scale test of both the theoretical method (PAW) and of the robustness of its computer implementation.

#### **4.1 Computational Strategy: PAW Investigation of Diffusion**

Our strategy for determining the diffusion characteristics of a Ga adatom on the  $c(4 \times 4)$  surface is straightforward. We begin with a simple repeated slab model of the (100) surface of GaAs. The initial unit cell is composed of five atomic layers of GaAs capped on the “non-interesting” side (the bottom) by the GaAs(001)- $c(2 \times 2)$  reconstruction and on the top by 6 As atoms. These 6 As atoms will eventually form the 3 As dimers found in the  $c(4 \times 4)$  reconstruction. The  $c(2 \times 2)$  surface was chosen to terminate the bottom surface; This procedure has been used with considerable success by Froyen *et al.* The initial geometry was taken from experimental data.<sup>38</sup> Next we calculated the correct ground state geometry using PAW. After the initial geometry had relaxed into the correct reconstruction, an adatom was introduced at a position  $(x,y)$  above the surface. (The surface is in the  $x$ - $y$  plane). Within the constraint that the  $(x,y)$  coordinates of the adatom be held fixed, all but the bottom two layers of the slab (actually one full monolayer of As and a half-monolayer of Ga) were allowed to settle into their equilibrium positions. Other researchers have typically ended their simulations when the force on the atoms falls below some

smallness criterion. As explained in greater detail in Chapter 3, we used an alternate method of determining convergence. After an initial geometry is found using an automatic simulated annealing routine, we simply allow the system to run without friction for a minimum of 1000 atomic time units. If, after this zero friction run, the total energy changes by less than 0.001 Hartrees, then convergence is assumed and the simulation is ended. If the system has not converged a further simulation with a small constant friction is run. This cycle repeats until convergence is found.

By repeating this procedure for 41 points within the real-space irreducible zone of the surface, we have mapped out the total energy of the structure as a function of adatom position:  $E_{adatom}(x, y)$ . The 41 sampling points are on a rectangular grid with a spacing of slightly less than 1 Å. The positions of these points are shown on figure 4.1.

After the complete map was produced, the energies of the bonding sites were calculated by allowing adatoms at the positions of the low points of the map to relax without constraint.† These bonding sites are shown on figure 4.1. In principle, the energy surface  $E_{adatom}(x, y)$  contains all the important physics of surface diffusion. A simple analysis of such an energy surface yields the surface diffusion activation energies. This data can then be used as input data for a Monte-Carlo simulation, which in turn can produce effective diffusion coefficients and/or effective migration velocities. The results of a Monte-Carlo analysis (using the *ab-initio* data calculated by the method outlined here) are presented in section 4.4. Alternately, the full surface could be used in a classical molecular dynamics simulation of adatom

---

† The bottom termination layer was held fixed during this simulation and every other simulation of the GaAs(100)-c(4x4) system. All other atoms, including the adatom were allowed to relax without constraint.

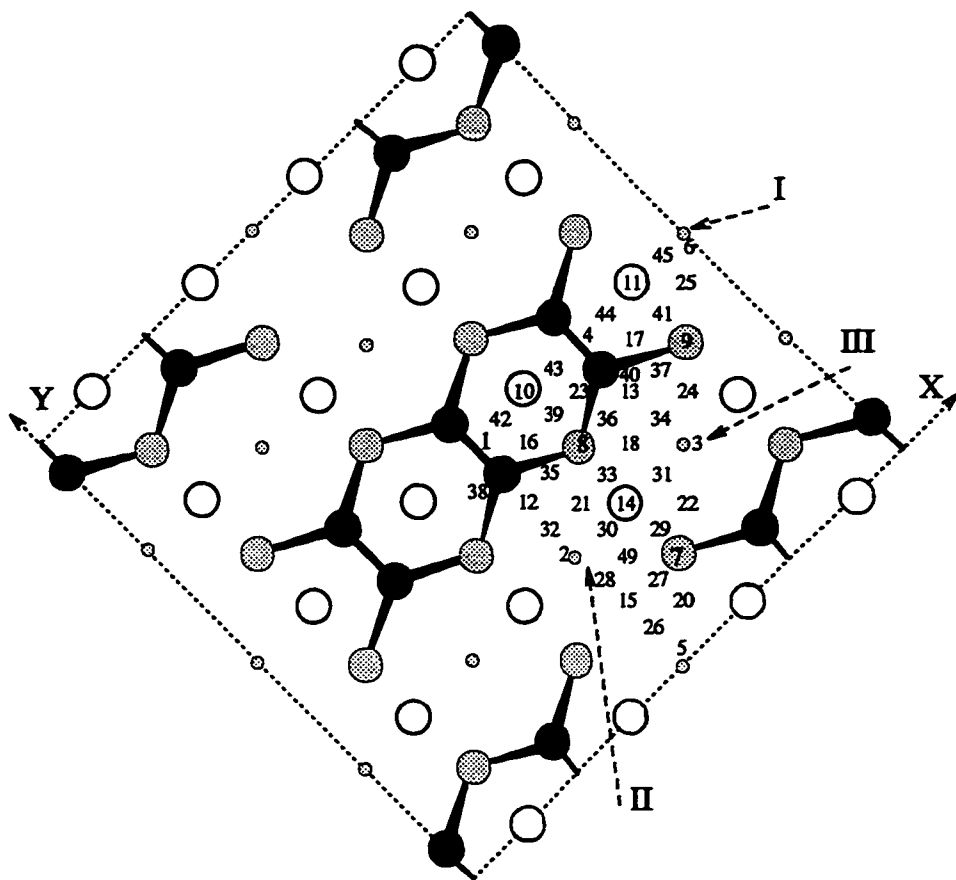


**FIGURE 4.1** Large scale schematic diagram of the GaAs(001)-c(4x4) reconstructed surface (top view) showing the positions of the sampling points (marked by the numbered triangles) at which  $E_{adatom}(x,y)$  was evaluated. The bonding sites (sites I, II, and III) are also shown. The x-y coordinates are given in Bohrs. The As dimer atoms are represented by black atoms, the subsurface As atoms by large light gray atoms, the Ga atoms (which are below the subsurface As atoms) by large white atoms, and the “bulk” As atoms (which are below the Ga atoms) by small light gray atoms. In this figure, the origin is in the center of the figure. The corner of the cell in the lowest part of the figure is at  $x = 15$  Bohr,  $y = 15$  Bohr.

diffusion.

## 4.2 Results: Ga Adatom Energy Surface

The principal results of our *ab-initio* calculations are shown in figures 4.2 and 4.3. The 3-dimensional rendering of the energy surface  $E_{adatom}(x, y)$  is the same in both figures. The energy surface shown is actually a cubic spline fit to the original data. The density of points on the interpolated map is nine times the density of the original map. Coincident (x,y) points on the original and interpolated maps have the same total energy value. In figure 4.2, the positions of the As dimers (in black) and the sub-surface As atoms (in gray) are shown. In figure 4.3, a 2-dimensional contour map rendering of the energy surface is shown below the 3-dimensional map. The contour spacing is 0.002 Hartrees. From the contour map we can identify three relatively stable adsorption sites. In order of increasing energy these sites are (I) the center of the missing dimer position ( $E_{adatom}=-244.044$  Hartrees), (II) between the dimer rows and adjacent to a center dimer ( $E_{adatom}=-244.037$  Hartrees), and (III) between the dimer rows, adjacent to an edge dimer ( $E_{adatom}=-244.026$  Hartrees). These positions are marked on figure 4.1. Perspective drawings of the three bonding geometries are shown in figures 4.4, 4.5, and 4.6.

The energy ordering of the bonding sites can be understood qualitatively by consideration of the bonding geometry at each site. Since Ga requires an additional five electrons to fill its outer shell, a Ga adatom will gravitate towards points on the surface where it can form bonds with a maximal number of nearest neighbors. Site I is an excellent example of this behavior. Here the adatom is in close proximity to four As atoms and can form moderately short bonds with all of them. Naturally

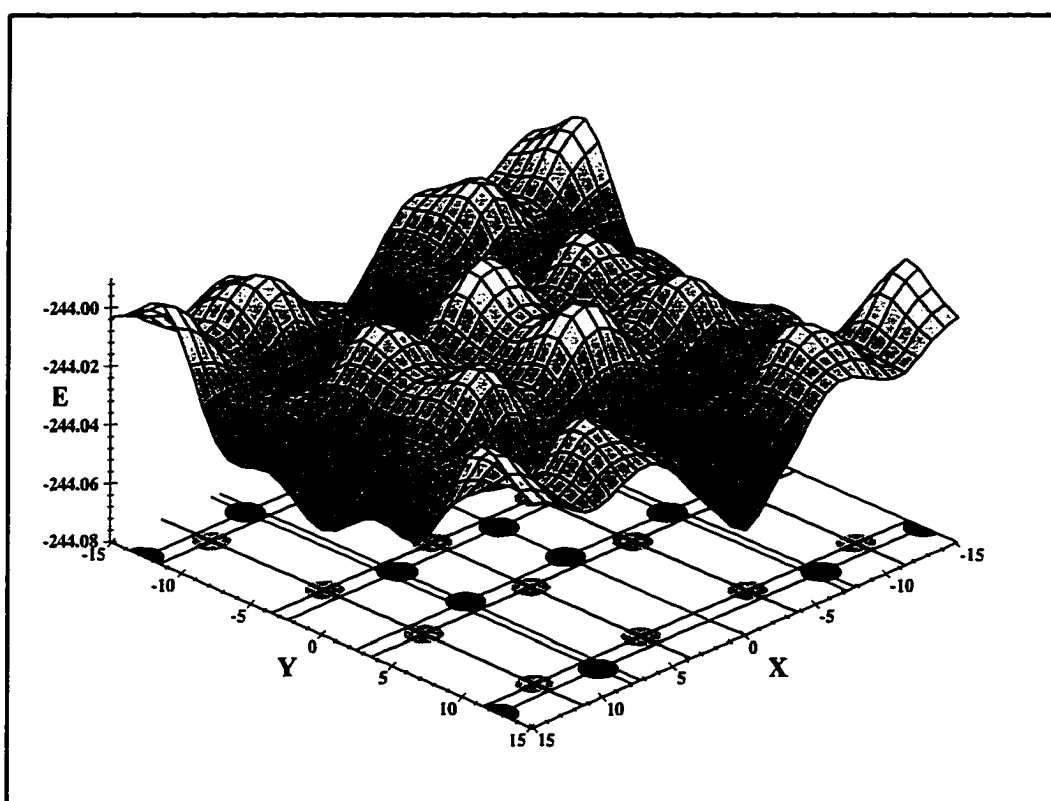


**FIGURE 4.2** The calculated potential energy surface  $E_{adatom}$  for Ga adatom diffusion on the GaAs(001)-c(4x4) surface. The positions of the As dimers are shown as black circles while the sub-surface As atoms appear as gray circles. The coordinate axes are labeled in Bohr. The energy units (vertical axis) are Hartrees.

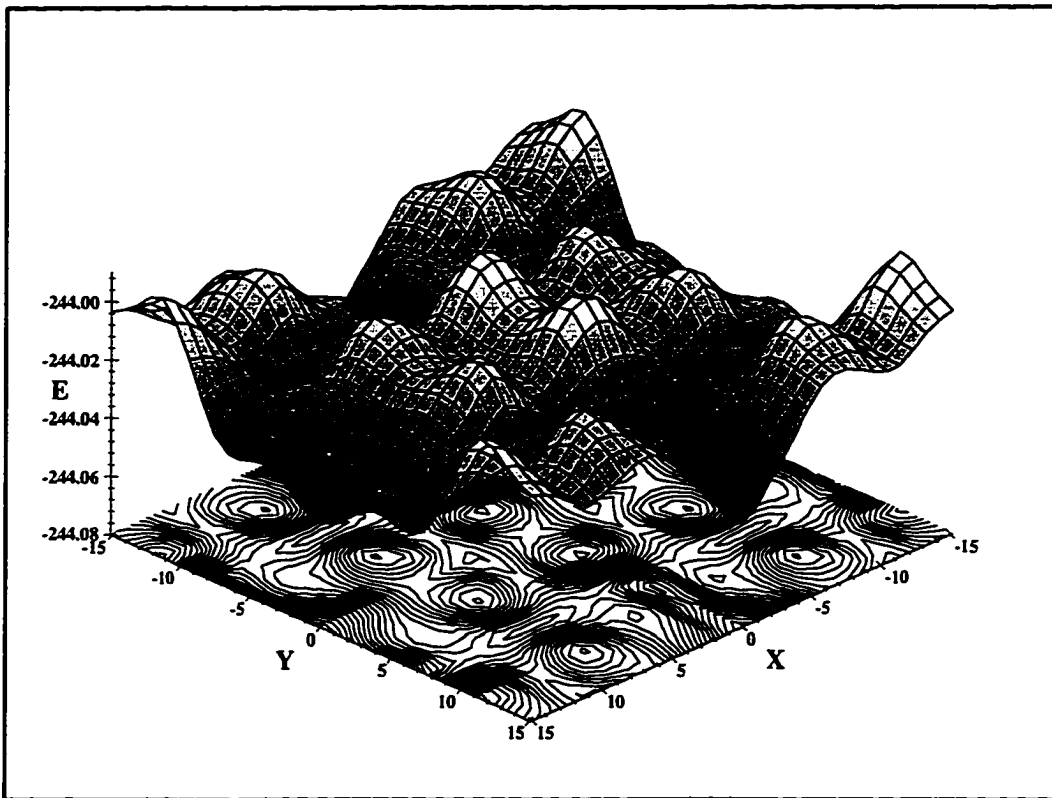


**FIGURE 4.3** The calculated potential energy surface  $E_{adatom}$  for Ga adatom diffusion on the GaAs(001)-c(4x4) surface. A 2-dimensional contour map corresponding to the 3-dimensional surface is shown on the plane below. The coordinate axes are labeled in Bohr. The energy units (vertical axis) are Hartrees. The contour spacing is 0.002 Hartrees.



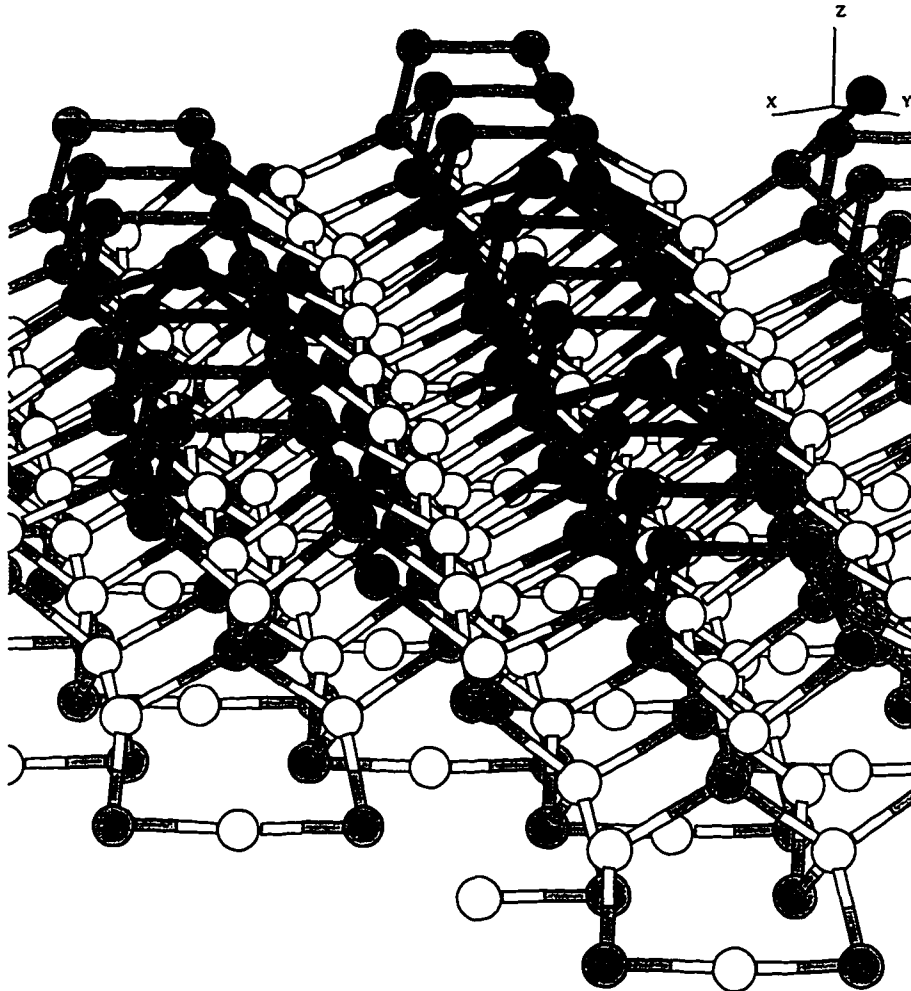


**FIGURE 4.4** Perspective drawing of the GaAs(001)-c(4x4) system with a Ga adatom at bonding site I. The Ga atoms are shown as light colored spheres, the As atoms as light-grey spheres and the Ga adatom as a dark sphere.

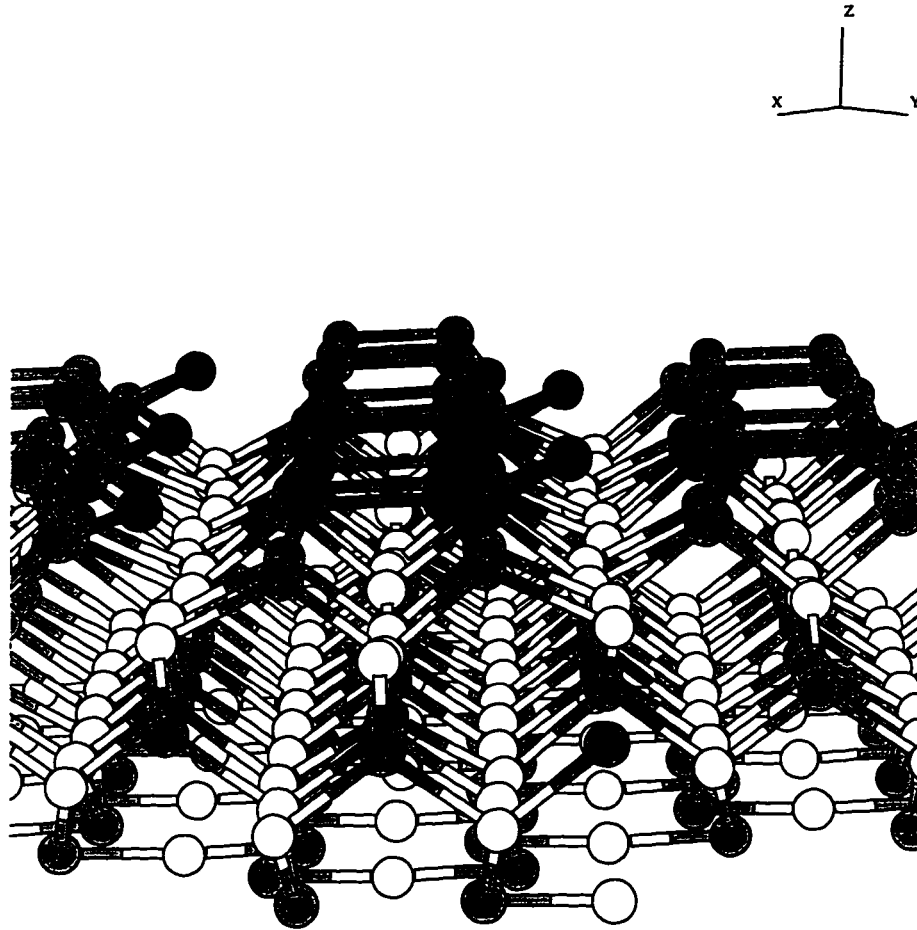


**FIGURE 4.5** Perspective drawing of the GaAs(001)-c(4x4) system with a Ga adatom at bonding site II. The Ga atoms are shown as light colored spheres, the As atoms as light-grey spheres and the Ga adatom as a dark sphere.

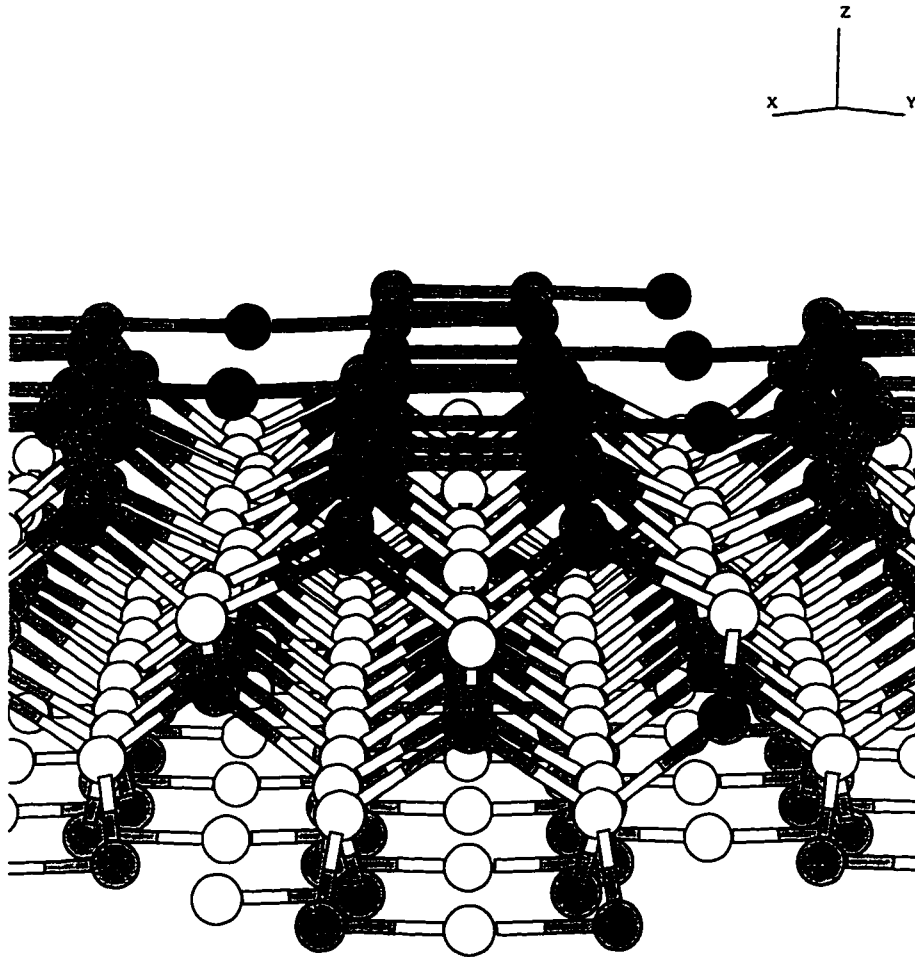


**FIGURE 4.6** Perspective drawing of the GaAs(001)-c(4x4) system with a Ga adatom at bonding site III. The Ga atoms are shown as light colored spheres, the As atoms as light-grey spheres and the Ga adatom as a dark sphere.

enough, this geometry yields the lowest energy. The adatom at site II is able to form bonds with only two neighboring As atoms; this geometry yields a bonding energy which 0.19 eV higher than the bonding energy at site I. Just as at site II, an adatom at site III forms a total of two bonds with neighboring As atoms. However, these bonds are stretched far beyond the normal length and so this site has the highest energy (0.49 eV above the energy at site I).

In order to understand the process of diffusion on this surface, we must first determine the activation energies. These energies are simply defined as the difference between an energy minimum (a bonding energy) and a neighboring saddle point. These can be read off the contour graph in figure 4.3. The activation energies for the transitions from bonding site to bonding site are given in table 4.1.

from site...	to site...	activation energy $E_{i,f}$
I	II	0.33 eV
II	I	0.14 eV
II	III	0.46 eV
III	II	0.16 eV

**TABLE 4.1** The activation energies for the transitions from bonding site to bonding site. An activation energy  $E_{i,f}$  for a hop from a given initial site  $i$  to a given final site  $f$  is defined as the difference in the total energy at the initial site  $E_i$  and the total energy  $E_{saddle}^{i,f}$  at the saddle point between the initial and final sites:  $E_{i,f} = E_{saddle}^{i,f} - E_i$ . Since  $E_i$  is generally not equal to  $E_f$ , the activation energy for a hop from site  $i$  to site  $f$  is generally not equal to the activation energy for the hop going the other way. This explains why  $E_{I-II}$  is not equal to  $E_{II-I}$ . Hops from site I to site III and vice-versa are excluded because these sites are not adjacent; site II is between sites I and III.

### 4.3 Computational Strategy: Monte Carlo Analysis of PAW Data

Given the data listed in table 4.1, it is possible to run a simple Monte Carlo<sup>14</sup> simulation and thereby determine the effective adatom migration rate and diffusivity. The algorithm used here is quite simple. It begins with the assumption that the Ga adatom sits in one of the three sites I, II, or III, as specified above. The adatom can make the following hops (corresponding activation energy given on the right):

$$I \Rightarrow II \quad E_{I-II} = 0.33\text{eV} \quad (4.1)$$

$$II \Rightarrow I \quad E_{II-I} = 0.14\text{eV} \quad (4.2)$$

$$II \Rightarrow III \quad E_{II-III} = 0.46\text{eV} \quad (4.3)$$

$$III \Rightarrow II \quad E_{III-II} = 0.16\text{eV} \quad (4.4)$$

The hopping rate for a given transition is assumed to have the Arrhenius form

$$r = v_0 e^{-E/kT} \quad (4.5)$$

where  $E$  is the relevant activation energy (as given in table 4.1) The hopping attempt frequency  $v_0$  is set equal to the frequency of a 2-dimensional harmonic oscillator:  $v_0 = 2kT/h$  At a simulation temperature of 200° C, the hopping rates are:

$$r_{I-II} = 6 \times 10^9 \text{s}^{-1} \quad (4.6)$$

$$r_{II-I} = 6.35 \times 10^{11} \text{s}^{-1} \quad (4.7)$$

$$r_{II-III} = 2.48 \times 10^8 \text{s}^{-1} \quad (4.8)$$

$$r_{III-II} = 3.89 \times 10^{11} \text{s}^{-1} \quad (4.9)$$

Before we can begin the calculations, we must determine the total hopping rate at each site. This quantity is obtained by adding the rates for all possible hops at each site. An adatom at site I can hop to one of two neighboring sites of type II. Therefore the total hopping rate at site I is

$$T_I = 2r_{I-II} = 12 \times 10^9 \text{s}^{-1}. \quad (4.10)$$

An adatom at site II can either hop to site I or it can hop to one of two sites of type III. Therefore the total hopping rate there is

$$T_{II} = r_{II-I} + 2r_{II-III} = 6.36 \times 10^{11} \text{s}^{-1}. \quad (4.11)$$

Adatoms at site III can hop to one of two sites of type II. Therefore, the total hopping rate is

$$T_{III} = 2r_{III-II} = 7.8 \times 10^{11} \text{s}^{-1}. \quad (4.12)$$

For sites I and III, a random coin flip determines into which of the two equivalent neighboring sites the adatom hops. For site III, the probability that a hop will take the adatom to site II is just

$$p_{III-II} = \frac{r_{III-II}}{T_{III}}. \quad (4.13)$$

The probability that the hop will take the adatom to either of the neighboring sites of type III is

$$p_{III-III} = \frac{2r_{III-III}}{T_{III}}. \quad (4.14)$$

The time that the adatom spends at a particular site  $i$  is given by

$$\Delta t_i = -\frac{\ln(Q)}{T_i}, \quad (4.15)$$

where  $Q$  is simply a random number from 0 to 1.

The algorithm outlined above was implemented and run for a large number of trials. The average displacement and mean square displacement were then determined as a function of time. The slope of these two curves yields the effective adatom migration rate and diffusivity, respectively.

#### 4.4 Results: Monte Carlo Results

Our Monte Carlo simulations predict that Ga adatom diffusion on this surface at 200° C is essentially symmetric with a diffusion coefficient of  $D_x = 8 \times 10^{-5} \text{ cm}^2/\text{s}$  in the x-direction and a diffusion coefficient of  $D_y = 7 \times 10^{-5} \text{ cm}^2/\text{s}$  in the y-direction.†

The apparent symmetry of diffusion is somewhat surprising considering the significant asymmetry of the original Ga adatom potential energy map. A close examination of the Monte Carlo data yields the explanation. At the temperature of the simulation (200° C), the adatom spends 98% of the time in type I sites. Adatoms at site II will make the transition to site I 99.92% of the time as opposed to 0.08% for the transition from II to III. Basically, an adatom cannot proceed very far down the path between the dimer rows without being pulled into the deep well at site I.

If the Ga concentration on the surface increases beyond a certain point, then sites of type I will naturally begin to fill up. Although no *ab-initio* calculations have been performed for this situation, we can perform a Monte Carlo simulation approximating this condition by simply assuming that site I is always occupied.

† To our knowledge, there are no experimental or Monte Carlo based estimates of the hopping rates or diffusion coefficients for this reconstruction.<sup>19</sup>

If this is the case, Ga adatoms can only travel in the trough between the dimer rows and the problem reduces to one-dimension. The diffusion coefficient is then  $D = 3.9 \times 10^{-3} \text{cm}^2/\text{s}$ , which is two orders of magnitude higher than the dilute case discussed in the paragraph above.



## CHAPTER 5

### PAW AND THE LOCAL DENSITY OF STATES

#### 5.0 Introduction

In this chapter we will present the details of a calculation of the local density of states for the Si(001)-(2x1) surface. We will show below that the local density of states can be directly related to experimental results found using scanning tunneling microscopy (STM) and scanning tunneling spectroscopy (STS).

#### 5.1 LDOS, STM, and STS

Within certain approximations, both the STM tunneling current and the scanning tunneling spectroscopy (STS) signal can be simply related to the local density of states. The local density of states is defined as

$$g(E, \vec{r}) = \sum_{\text{states } i} |\Psi_i(\vec{r})|^2 \delta(E - E_i). \quad (5.1)$$

The tunneling current is<sup>39</sup>

$$I_{STM} = 2\pi \sum_{\text{states } ij} f(E_i)[1 - f(E_j + V)] |M_{i,j}|^2 \delta(E_i - E_j), \quad (5.2)$$

where  $f(E_i)$  is the occupation of state  $i$  of the tip, and  $E_i, E_j$  are the energies of states  $i$  and  $j$  of the tip and surface, respectively.  $M_{i,j}$  is the tunneling matrix element given by

$$M_{i,j} = \frac{1}{2} \int d\vec{S} \cdot (\Psi_i^* \nabla \Psi_j - \Psi_j \nabla \Psi_i^*), \quad (5.3)$$

In the limit of small temperature and small voltage, this reduces to

$$I_{STM} = 2\pi V \sum_{\text{states } i,j} |M_{i,j}|^2 \delta(E_i - E_f) \delta(E_j - E_f) \quad (5.4)$$

In the case of a perfectly localized and perfectly non-intrusive probe, this reduces still further:<sup>1</sup>

$$I_{STM} \propto g(E, \vec{r}) \equiv \sum_{\text{states } i} |\Psi_i(\vec{r})|^2 \delta(E_i - E_f). \quad (5.5)$$

Alternately, the local density of states can be related to the scanning tunneling spectroscopy signal. Feenstra<sup>40</sup> has shown that the local density of states is approximated by the measured normalized differential conductance (NDC):

$$g(V_s + E_f) \sim \left. \frac{d \ln I}{d \ln V} \right|_{V=V_s}. \quad (5.6)$$

Where  $V_s$  is the sample voltage and  $E_f$  is the Fermi energy of the sample.

## 5.2 PAW and LDOS

Within the PAW formalism, it is a simple matter to generate the local density of states. First, we must generate the self-consistent potential  $V_{eff}^{(PW)}$ , as well as the terms  $\langle \phi_i^{(at)} | -\frac{1}{2} \nabla^2 + V_{eff}^{(at)} | \phi_j^{(ps-at)} \rangle$  and  $\langle \phi_i^{(ps-at)} | -\frac{1}{2} \nabla^2 + V_{eff}^{(ps-at)} | \phi_j^{(ps-at)} \rangle$ . Together with the kinetic energy operator  $\frac{1}{2} \nabla^2$  these terms can be used to form the PAW Hamiltonian and overlap operator. Once this has been done the generalized

matrix eigenvalue problem is set up and solved. The resultant wave functions are then used to form the density of states according to equation (5.1). The integration over the Brillouin zone was accomplished using the tetrahedron method<sup>41</sup> and 256 k-points in the irreducible Brillouin zone. Due to the low-symmetry of this structure, the irreducible Brillouin zone constitutes half of the complete Brillouin zone. The k-points are on a regular k-space grid which is shifted from  $\Gamma$  by half the grid spacing in each of the  $k_x$ ,  $k_y$ , and  $k_z$  directions. This shift removes possible high-symmetry point degeneracies from the k-space integration.

A plot of an isosurface<sup>†</sup> of the density of states is essentially equivalent (see equation (5.5)) to a constant current topography (CCT) obtained with an STM. In contrast, a plot of the density of states at a constant height above the surface yields a function which is analogous to an STS image.

### 5.3 LDOS: Results

In Figures 5.1 and 5.2, we have plotted the local density of states in a plane at a height of  $1.5\text{\AA}$  above the atomic center of the up-atom of the buckled dimer on the Si(001)-(2x1) surface. Figure 5.1 shows the local density of states evaluated at an energy of 0.82 eV below the highest occupied level. At this energy, a peak occurs in the local density of states above the up-atom in the dimer. At this energy the down-atom in the dimer does not make a significant contribution to the LDOS. Figure 5.2 shows the LDOS evaluated at an energy of 0.4 eV above the highest occupied level. At this energy, two peaks occur in the LDOS; one is above the

---

<sup>†</sup> By “isosurface” we mean a three dimensional plot of the (x,y,z) coordinates such that the local density of states  $g(E, x, y, z)$  is a constant.

down-atom and the other is above the up-atom. As a result, at this energy both atoms in the dimer are plainly visible in the local density of states.

The PAW data shares certain qualitative features with the earlier tight-binding results of Molotkov *et al.*<sup>42</sup>. In both the PAW data and Molotkov's data, there is a valence band peak in the local density of states associated with the up atom in the buckled dimer. PAW puts this peak at an energy 0.82 eV below the highest occupied level while Molotkov's tight-binding model places this peak 1.4 eV below the highest occupied level (0.58 eV lower than PAW). Additionally, both PAW and Molotkov's tight-binding method predict nearly coincident up-atom and down-atom peaks at energies a few tenths of an eV above the valence band maximum. The PAW data gives the energies of both the up-atom and down-atom peaks as 0.4 eV above the highest occupied level while Molotkov's data has these peaks at 0.6 eV (0.2 eV higher than predicted by PAW).

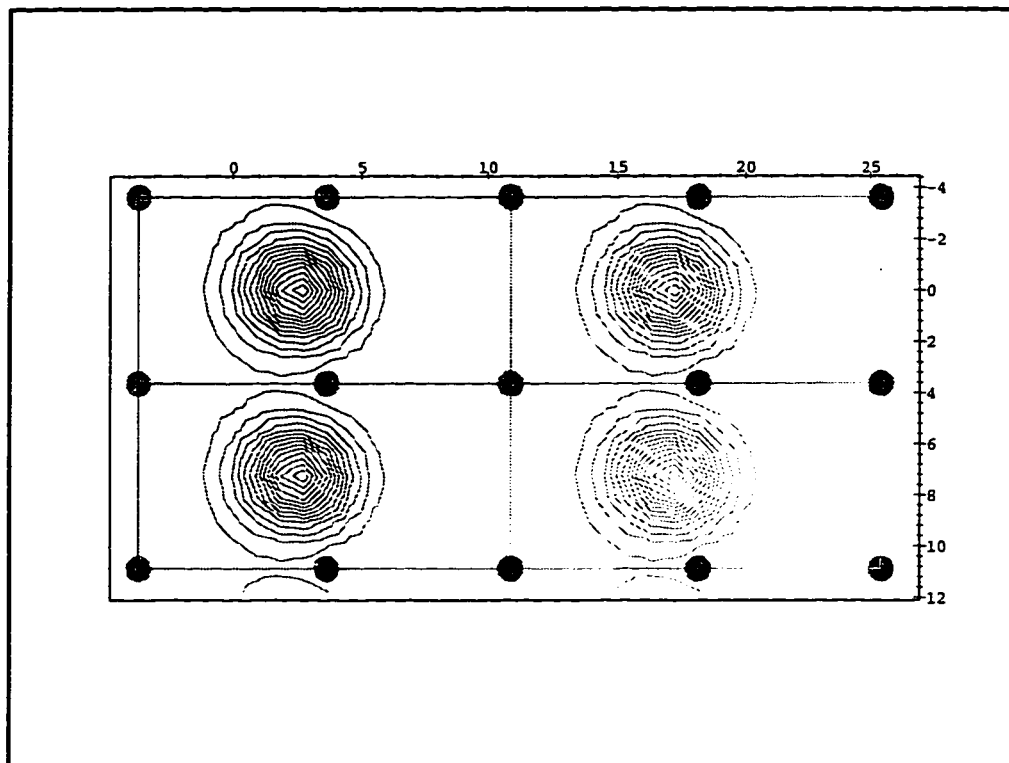


**FIGURE 5.1** Contour plot of the local density of states (LDOS) above the Si(001)-(2x1) surface evaluated at an energy of  $-0.82$  eV with respect to the highest occupied state. At this energy, the up atom in the buckled dimer shows up in the LDOS but the down atom does not. Four unit cells are shown. These unit cells are identical to those shown in Figure 3.2. The positions of the atoms in the layer below the dimer layer are shown as gray circles. The x-y coordinates are given in units of Bohr. The lowest contour line is at  $0.01 a_0^{-3} Ry^{-1}$  and the contour step is  $0.01 a_0^{-3} Ry^{-1}$ . The highest contour (at the center of the concentric rings) is at  $0.14 a_0^{-3} Ry^{-1}$ .

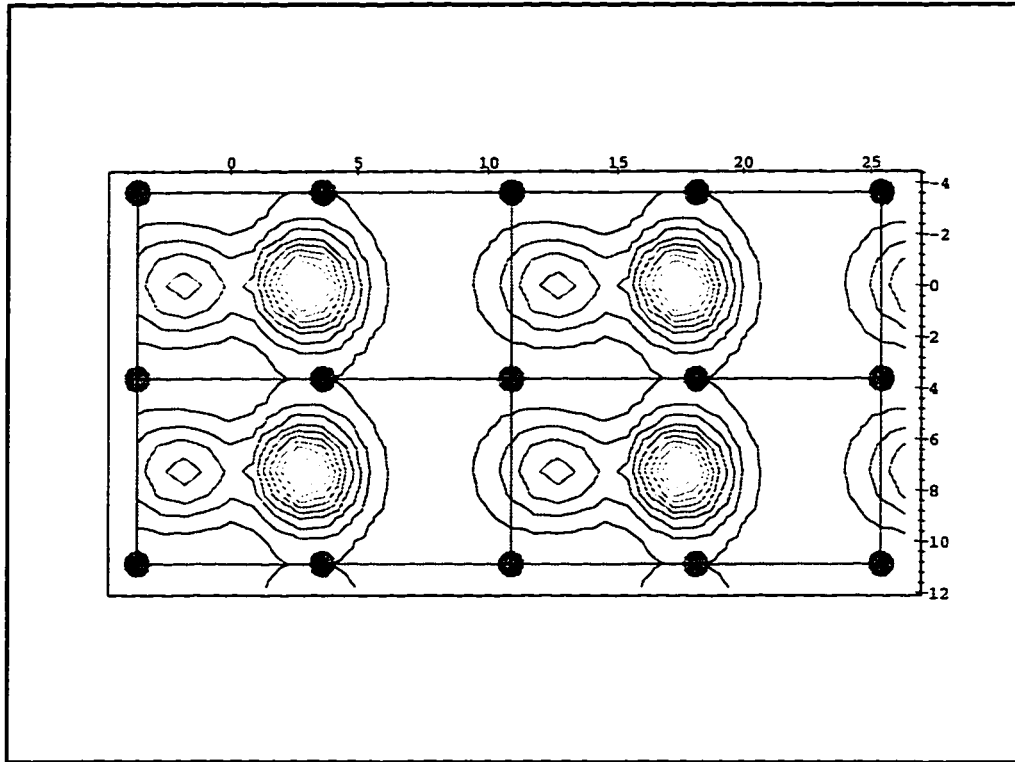


**FIGURE 5.2** Contour plot of the local density of states (LDOS) above the Si(001)-(2x1) surface evaluated at an energy of 0.4 eV with respect to the highest occupied state. At this energy, both up and down atoms in the buckled dimer show up in the LDOS. Four unit cells are shown. These unit cells are identical to those shown in Figure 3.2. The up atom is on the right side of each unit cell. The positions of the atoms in the layer below the dimer layer are shown as gray circles. The x-y coordinates are given in units of Bohr. The lowest contour line is at  $0.002 a_0^{-3} Ry^{-1}$  and the contour step is  $0.002 a_0^{-3} Ry^{-1}$ . The highest contour step (at the center of the concentric rings about the up atom) is at  $0.020 a_0^{-3} Ry^{-1}$ .

## CHAPTER 6

### PAW AND DIELECTRIC FUNCTIONS

#### 6.0 Introduction

In this chapter we present the details of the first ever calculation of optical properties using the PAW formalism. The subject of our calculations will be bulk Si and GaAs. Agreement with experiment and previous theoretical calculations is good, indicating that PAW is capable of a wide variety of calculations.

#### 6.1 PAW OPTICS

Adler and Wiser<sup>43,44</sup> have derived, within the RPA, the following expression for the dielectric response matrix:

$$\begin{aligned}
 \epsilon_{\vec{G}, \vec{G}'}(\vec{q}, \omega) = & \delta_{\vec{G}, \vec{G}'} \\
 & - \frac{4\pi}{\Omega |\vec{q} + \vec{G}| |\vec{q} + \vec{G}'|} \sum_{\vec{k}, n, n'} \frac{f_0[E_{n'}(\vec{k} + \vec{q})] - f_0[E_{n'}(\vec{k})]}{E_{n'}(\vec{k} + \vec{q}) - E_n(\vec{k}) + \omega + i\alpha} \\
 & \times \langle \Psi_{n', \vec{k} + \vec{q}} | \exp[i(\vec{q} + \vec{G}) \cdot \vec{r}] | \Psi_{n, \vec{k}} \rangle \\
 & \times \langle \Psi_{n, \vec{k}} | \exp[-i(\vec{q} + \vec{G}') \cdot \vec{r}] | \Psi_{n', \vec{k} + \vec{q}} \rangle,
 \end{aligned} \tag{6.1}$$

where  $\vec{G}$  and  $\vec{G}'$  are reciprocal lattice vectors,  $n$  is a band index,  $E_n(\vec{k})$  is the energy of the  $n$ th state with wave vector  $\vec{k}$  and  $\Omega$  is the volume of the unit cell. The PAW version of the required matrix element is

$$\begin{aligned}
& \langle \Psi_{n', \vec{k} + \vec{q}} | \exp[i(\vec{q} + \vec{G}) \cdot \vec{r}] | \Psi_{n, \vec{k}} \rangle \\
&= \langle \psi_{n', \vec{k} + \vec{q}}^{(PW)} | \exp[i(\vec{q} + \vec{G}) \cdot \vec{r}] | \psi_{n, \vec{k}}^{(PW)} \rangle \\
&+ \sum_{\vec{R}} \sum_{i, j} \langle \psi_{n', \vec{k} + \vec{q}}^{(PW)} | \tilde{p}_{i, \vec{R}} \rangle \\
&\times \left( \langle \phi_{i, \vec{R}}^{(at)} | \exp[i(\vec{q} + \vec{G}) \cdot \vec{r}] | \phi_{j, \vec{R}}^{(at)} \rangle - \langle \phi_{i, \vec{R}}^{(ps-at)} | \exp[i(\vec{q} + \vec{G}) \cdot \vec{r}] | \phi_{j, \vec{R}}^{(ps-at)} \rangle \right) \\
&\times \langle \tilde{p}_{j, \vec{R}} | \psi_{n, \vec{k}}^{(PW)} \rangle.
\end{aligned} \tag{6.2}$$

If  $\vec{G} = \vec{G}' = 0$  and in the limit that  $\vec{q} \rightarrow 0$ , the imaginary part of equation (6.1) is simply

$$\epsilon_2(\omega) = \frac{1}{3\omega^2\pi} \sum_{n, n'} \int d^3k |\langle \Psi_{n, \vec{k}} | \vec{p} | \Psi_{n', \vec{k}} \rangle|^2 f_{n, \vec{k}} (1 - f_{n', \vec{k}}) \delta(E_{n', \vec{k}} - E_{n, \vec{k}} - \omega). \tag{6.3}$$

In our calculations of the dielectric functions of Si and GaAs we used equation (6.3). The integration over the Brillouin zone was accomplished using the tetrahedron method<sup>41</sup> and 110 k-points in the irreducible Brillouin zone. The k-points are on a regular k-space grid which is shifted from  $\Gamma$  by half the grid spacing in each of the  $k_x$ ,  $k_y$ , and  $k_z$  directions. This shift removes possible high-symmetry point degeneracies from the k-space integration. These degeneracies can cause difficulties because wavefunctions with differing symmetries but the same eigenvalue may be given equal weights in the integration.

To test the accuracy of the calculations the f-sum rule was checked and was found to be 1.035 for Si and 1.03 for GaAs. The results of our calculations are shown in figures 6.1 and 6.2. The PAW results agree well with both the earlier LMTO results<sup>45</sup> and with experiment.<sup>46</sup>



### $\epsilon_2$ of Si with 110 k\_points

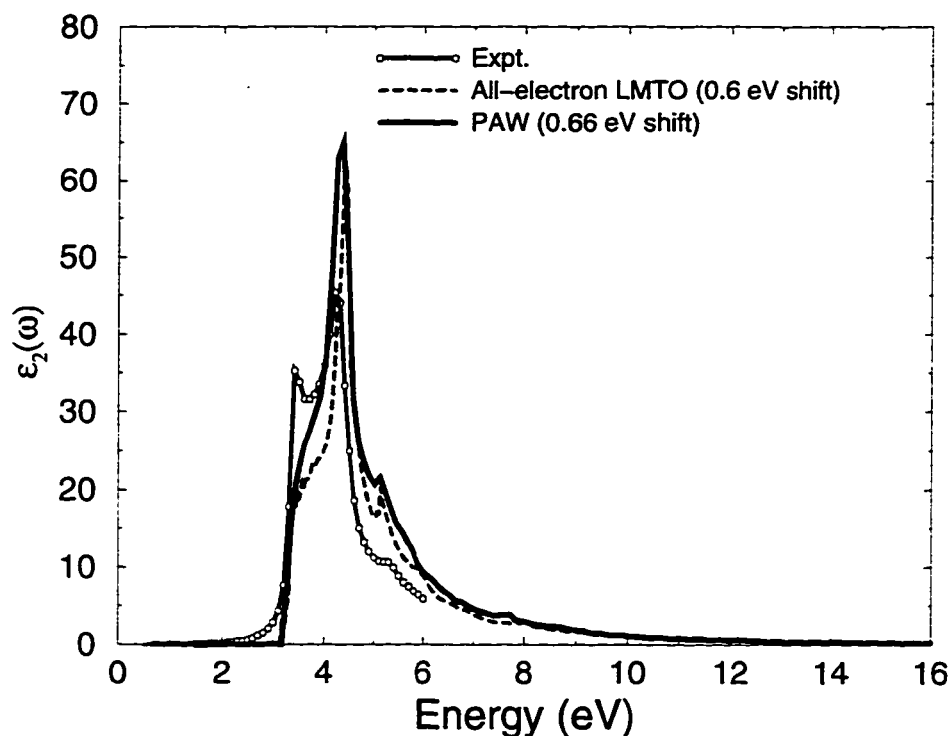


**FIGURE 6.1** The imaginary part of the dielectric function for Si as calculated by PAW, full potential LMTO and as measured by experiment. The experimental data is from reference Ref. 46. The LMTO data is from reference Ref. 45. PAW agrees extremely well with both experiment and LMTO. The calculated PAW band gap is 0.06 smaller than the LMTO calculated band gap. As a result, the PAW dielectric function was shifted 0.06 eV to the right with respect to the LMTO calculated curve. 110 k-points were used in the Brillouin zone integration.

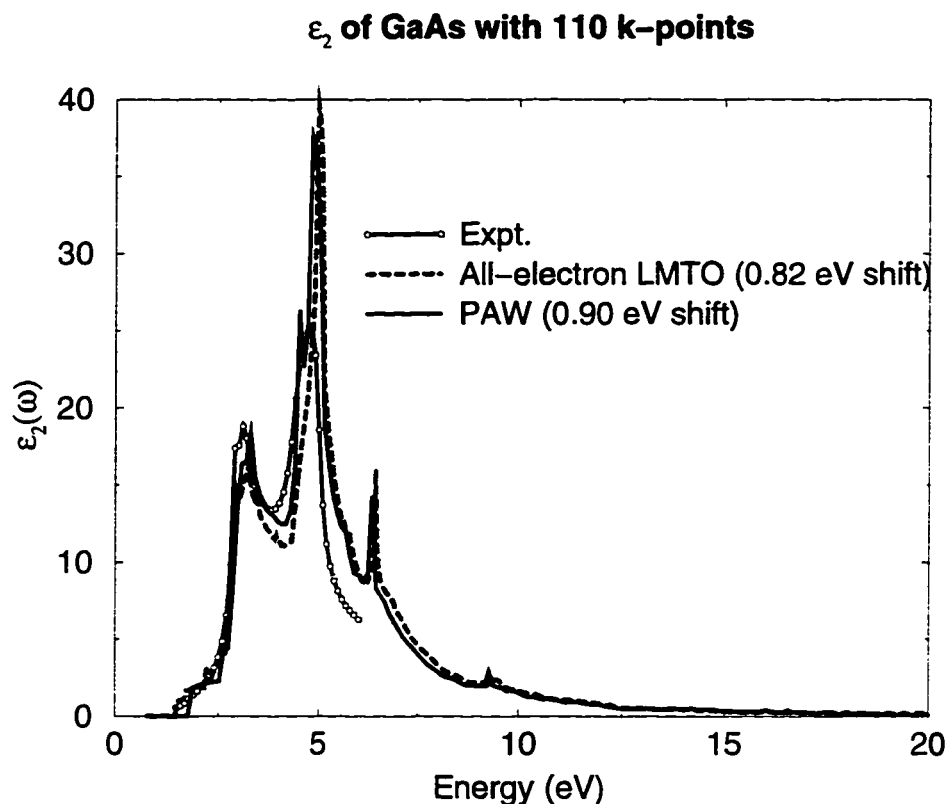


**FIGURE 6.2** The imaginary part of the dielectric function for GaAs as calculated by PAW, full potential LMTO and as measured by experiment. PAW agrees extremely well with both experiment and LMTO. The experimental data is from reference Ref. 46. The LMTO data is from reference Ref. 45. The calculated PAW band gap is 0.08 eV smaller than the LMTO calculated band gap. As a result, the PAW dielectric function was shifted 0.08 eV to the right with respect to the LMTO calculated curve. 110 k-points were used in the Brillouin zone integration.

## CHAPTER 7

### CONCLUSIONS AND FUTURE RESEARCH

#### 7.0 Advertisement

In an effort to advance our knowledge of the physics of GaAs and Si surfaces we have employed a new theoretical formalism, PAW, to investigate the electronic properties, structural details, and diffusion mechanisms of these systems. In this concluding chapter, we will first summarize our results and then move on to a discussion of possible future research.

#### 7.1 Summary of Dissertation Results

We began our study with a determination of the ground state geometries of the GaAs(100)-c(4x4), GaAs(100)-c(2x2), and Si(001)-(2x1) surfaces. All calculated geometries were found to agree well with earlier experimental and theoretical data. In order to give the reader some sense of the detailed physics of bonding on the GaAs surface, Pashley's electron counting rule was introduced and applied to the GaAs(100)-c(4x4) surface.

Next we performed a large *ab-initio* investigation of Ga adatom diffusion on the GaAs(100)-c(4x4) surface. The result of this calculation was a potential energy map for the Ga adatom over the whole surface. At first glance, this surface seemed to indicate that the Ga diffusion should be highly anisotropic, with the Ga adatoms freely traveling in the trough between the dimer rows but being hindered by large potential barriers and deep wells in the pathway through the missing dimer row. However, a Monte Carlo simulation using our calculated data showed that this was not the case. In actuality, the Ga adatom can usually only travel a short distance along the trough between the dimer rows before falling into the well at site I. As a result, Ga adatom diffusion on this surface is surprisingly isotropic.

Next we calculated the local density of states for the surface of Si(001)-c(2x1). The results were found to agree fairly well with the available published data in at least one important respect: the down dimer only shows up at high energies.

Finally, we calculated the bulk GaAs and Si dielectric functions. These calculations were the first ever optical calculations done using PAW. Agreement with experiment and other theoretical methods was excellent. These calculations indicate that PAW, which previously had been used exclusively for ground state and molecular dynamics calculations, is fully capable of handling optics calculations.

## 1.2 Possible Future Research: Molecular Dynamics

In this work we have used Monte Carlo techniques to calculate diffusion data based on our Ga adatom potential energy surface. One other possibility is to use the calculated potential in a molecular dynamics simulation. One significant difference between Monte Carlo simulations and Molecular Dynamics is that there is no

conservation of momentum in standard Monte Carlo. In a full molecular dynamics simulation, atoms move according to the laws of classical dynamics and are subject to a position-dependent potential  $V(\vec{R})$ . In this sort of simulation, each atom has a well-defined position and momentum which evolve in time. Naturally, the behavior of an atom upon encountering a bonding site is a function of its initial momentum. On the other hand, in standard Monte Carlo simulations, atoms merely make transitions from state to state. As a result, each subsequent hop is independent of all previous hops. It would be very interesting to see what the hopping statistics predicted by Molecular Dynamics are compared to those predicted by Monte Carlo.

### **1.3 Possible Future Research: Multiple Adatoms**

Now that the diffusion of a single adatom on the GaAs(100)-c(4x4) surface has been properly characterized, it may be time to move on to more complicated systems. The simplest extension would be to occupy the most likely bonding site (site I) with a Ga atom. Based on the data we already have, the occupation of this site should induce some fairly high anisotropy in the diffusion data.

### **1.4 Possible Future Research: Surface Optics**

In principle, once an optics code has been created, the calculation of surface optics should be a simple matter. In practice, the large size of the unit cell forces the size of the Hamiltonian matrix to extraordinary size. In fact, for the GaAs(100)-c(4x4) unit cell used here the Hamiltonian would occupy over a gigabyte in computer memory. As a result, the simple techniques we have used for the bulk must be

abandoned and more intelligent (and memory conserving) algorithms must be used. The amount of programming for such a project would be great, but the final result would be worth the effort.

## APPENDIX

### Convergence Data

Convergence with respect to the number of iterations was checked by a two-step process. In the first step, the system is “cooled” by running a molecular dynamics simulation which incorporated a frictional force. This run is followed by a zero friction run. If the Kohn-Sham total energy is seen to vary by less than 0.001 Hartrees during the zero friction run, then it can safely be assumed that the system has converged with respect to the number of iterations. If the observed variation in the total energy is found to be greater than 0.001 Hartrees then another run **with** friction is done, followed by yet another run **without** friction. The process is repeated until the ground state is found.

In a series of test, the convergence of the calculated energies of our model systems was checked with respect to plane wave cutoff, number of k-points used in the Brillouin zone integration, and vacuum interface thickness. The quantity of interest in convergence data analysis is the not the total energy but instead the difference  $\Delta_{a,b}(p)$  between the total energies of two different structures  $a$  and  $b$ :

$$\Delta_{a,b}(p) = E_{total,a}(p) - E_{total,b}(p). \quad (8.1)$$

The argument  $p$  is just some parameter of the calculation like plane wave cutoff,

number of k-points, or vacuum interface thickness. If this difference does not change appreciably as a given calculational parameter  $p$  is increased, then convergence can reasonably be assumed. The standard rule is that if a substantial change in  $p$  results in a change in  $\Delta_{a,b}(p)$  of 25meV or less then the system has almost certainly converged. This criterion is met in our tests.

In the tables that follow the total energies of the {GaAs(100)-c(4x4) + Ga adatom} system are given for a variety of plane wave cutoffs, vacuum interface thicknesses and Brillouin zone integration schemes. These values are listed along with the changes  $\delta_a(p, p')$  in the total energy that result when the parameter  $p$  is changed:

$$\delta_a(p, p') = E_{total,a}(p) - E_{total,a}(p'). \quad (8.2)$$

The “difference of the differences”

$$\Delta_{\Delta}^{a,b}(p, p') = (\delta_a(p, p') - \delta_b(p, p')), \quad (8.3)$$

between the changes in the total energy for two separate systems  $a$  and  $b$  gives a measure of the convergence. If this value is below 25meV then the system is converged to chemical accuracy.



# adatom position	$E_{total} = E_{surf.} + E_{adatom}$ (1 k-point) (Hartrees)	(4 k-point) (Hartrees)	$E_{1k} - E_{4k}$ Difference (eV)
1		-244.03289	
2	-243.97313	-244.02992	1.545
3	-243.97520	-244.02584	1.378
4	-243.95036	-244.00769	1.560
5	-243.99853	-244.04406	1.239
7	-243.95962	-244.01629	1.542
8	-243.95665	-244.01165	1.497
10	-243.95724	-244.01423	1.551
11	-243.96949	-244.02213	1.432
12	-243.93373	-243.99123	1.565
13	-243.94212	-243.99749	1.507
14	-243.96839	-244.02106	1.433
15	-243.98048	-244.03220	1.407
16	-243.94376	-244.00251	1.599
17	-243.95032	-244.00726	1.549
18	-243.95959	-244.01466	1.499
19	-243.96796	-244.01961	1.405
20	-243.97360	-244.02537	1.409
21	-243.95491	-244.01107	1.528
22	-243.96328	-244.01627	1.442
23	-243.95005	-244.00451	1.482

**TABLE A.1a** Raw data for the GaAs(100)-c(4x4) system at a plane wave cutoff of 5 Hartrees. The first column is the adatom position label (see figure 4.1 to find the x-y positions in the unit cell to which these labels refer). The second column is the total energy calculated using only the  $\Gamma$  point in the Brillouin zone integration. The third column is the total energy calculated using a Brillouin zone integration with four special points. The final column is the difference  $\delta_a(\Gamma, 4k)$  of the energies between the  $\Gamma$ -point and 4k-point calculations (see the beginning of this appendix for an explanation of the notation). The data in the third column (plane wave cutoff of 5 Hartrees, 4 k-point integration routine) served as the primary data set for this study. This table is continued on the next page. An analysis this data appears in tables A.2a, A.2b, A.2c, and A.2d.

# adatom position	$E_{total} = E_{surf.} + E_{adatom}$ (1 k-point) (Hartrees)	(4 k-point) (Hartrees)	$E_{1k} - E_{4k}$ Difference (eV)
25	-243.97422	-244.02601	1.409
26	-243.98902	-244.03864	1.350
27	-243.96537	-244.01879	1.454
28	-243.98367	-244.03443	1.381
29	-243.96220	-244.01716	1.496
30	-243.97086	-244.02231	1.400
31	-243.97389	-244.02421	1.369
32		-244.00793	
33		-244.01720	
34		-244.00837	
35		-243.99883	
36	-243.94996	-244.00523	1.504
37		-244.00739	
38		-243.99712	
39		-243.01318	
40		-244.00206	
41		-244.01713	
42		-244.00726	
43		-244.01256	
44		-244.00958	
45		-244.03431	

**TABLE A.1b** Raw data for the GaAs(100)-c(4x4) system at a plane wave cutoff of 5 Hartrees. The first column is the adatom position label (see figure 4.1 to find the x-y positions in the unit cell to which these labels refer). The second column is the total energy calculated using only the  $\Gamma$  point in the Brillouin zone integration. The third column is the total energy calculated using a Brillouin zone integration with four special points. The final column is the difference of the energies between the  $\Gamma$ -point and 4k-point calculations (see the beginning of this appendix for an explanation of the notation). The data in the third column (plane wave cutoff of 5 Hartrees, 4 k-point integration routine) served as the primary data set for this study. This table is continued from the previous page. An analysis this data appears in tables A.2a, A.2b, A.2c, A.2d.

---

	2	3	4	5	7	8	10	11
2	0.000	-0.167	0.015	-0.306	-0.003	-0.049	0.005	-0.113
3	0.167	0.000	0.182	-0.139	0.164	0.119	0.173	0.054
4	-0.015	-0.182	0.000	-0.321	-0.018	-0.063	-0.009	-0.128
5	0.306	0.139	0.321	0.000	0.303	0.258	0.312	0.193
7	0.003	-0.164	0.018	-0.303	0.000	-0.045	0.009	-0.110
8	0.049	-0.119	0.063	-0.258	0.045	0.000	0.054	-0.064
10	-0.005	-0.173	0.009	-0.312	-0.009	-0.054	0.000	-0.118
11	0.113	-0.054	0.128	-0.193	0.110	0.064	0.118	0.000
12	-0.019	-0.187	-0.005	-0.326	-0.023	-0.068	-0.014	-0.132
13	0.039	-0.129	0.053	-0.268	0.035	-0.010	0.044	-0.074
14	0.112	-0.055	0.127	-0.194	0.109	0.063	0.118	-0.001
15	0.138	-0.029	0.153	-0.168	0.135	0.089	0.143	0.025
16	-0.053	-0.221	-0.039	-0.360	-0.057	-0.102	-0.048	-0.166
17	-0.004	-0.171	0.011	-0.310	-0.007	-0.053	0.001	-0.117
18	0.047	-0.121	0.062	-0.260	0.044	-0.002	0.052	-0.066
19	0.140	-0.027	0.155	-0.167	0.137	0.091	0.145	0.027
20	0.137	-0.031	0.151	-0.170	0.133	0.088	0.142	0.024
21	0.017	-0.150	0.032	-0.289	0.014	-0.032	0.023	-0.096
22	0.103	-0.064	0.118	-0.203	0.100	0.055	0.109	-0.010
23	0.063	-0.104	0.078	-0.243	0.060	0.015	0.069	-0.050
25	0.136	-0.031	0.151	-0.170	0.133	0.087	0.141	0.023
26	0.195	0.028	0.210	-0.111	0.192	0.146	0.201	0.082
27	0.092	-0.076	0.106	-0.215	0.088	0.043	0.097	-0.021
28	0.164	-0.003	0.179	-0.142	0.161	0.115	0.170	0.051
29	0.050	-0.118	0.064	-0.257	0.047	0.001	0.055	-0.063
30	0.145	-0.022	0.160	-0.161	0.142	0.097	0.151	0.032
31	0.176	0.009	0.191	-0.130	0.173	0.127	0.182	0.063
36	0.041	-0.126	0.056	-0.265	0.038	-0.007	0.047	-0.072

---

**TABLE A.2a** Table of  $\Delta_{a,b}(\Gamma, 4k)$  for the GaAs(100)-c(4x4) system. The “difference of the differences”  $\Delta_{\Delta}^{a,b}(\Gamma, 4k) = (\delta_a(\Gamma, 4k) - \delta_b(\Gamma, 4k))$  for a given set of adatom positions  $a$  and  $b$  is found at the  $a$ th row and  $b$ th column.  $\Delta_{\Delta}^{a,b}(\Gamma, 4k)$  is given in eV. A quick glance at this table indicates that convergence has not been reached using a  $\Gamma$ -point Brillouin zone integration. In light of this data, we performed all of our calculations using a 4 special k-points. See figure 4.1 to find the x-y positions in the unit cell to which these labels refer). This table is continued on the next page.

	12	13	14	15	16	17	18	19
2	0.019	-0.039	-0.112	-0.138	0.053	0.004	-0.047	-0.140
3	0.187	0.129	0.055	0.029	0.221	0.171	0.121	0.027
4	0.005	-0.053	-0.127	-0.153	0.039	-0.011	-0.062	-0.155
5	0.326	0.268	0.194	0.168	0.360	0.310	0.260	0.167
7	0.023	-0.035	-0.109	-0.135	0.057	0.007	-0.044	-0.137
8	0.068	0.010	-0.063	-0.089	0.102	0.053	0.002	-0.091
10	0.014	-0.044	-0.118	-0.143	0.048	-0.001	-0.052	-0.145
11	0.132	0.074	0.001	-0.025	0.166	0.117	0.066	-0.027
12	0.000	-0.058	-0.131	-0.157	0.034	-0.015	-0.066	-0.159
13	0.058	0.000	-0.073	-0.099	0.092	0.043	-0.008	-0.101
14	0.131	0.073	0.000	-0.026	0.165	0.116	0.065	-0.028
15	0.157	0.099	0.026	0.000	0.191	0.142	0.091	-0.002
16	-0.034	-0.092	-0.165	-0.191	0.000	-0.049	-0.100	-0.193
17	0.015	-0.043	-0.116	-0.142	0.049	0.000	-0.051	-0.144
18	0.066	0.008	-0.065	-0.091	0.100	0.051	0.000	-0.093
19	0.159	0.101	0.028	0.002	0.193	0.144	0.093	0.000
20	0.156	0.098	0.024	-0.001	0.190	0.141	0.090	-0.003
21	0.036	-0.021	-0.095	-0.121	0.070	0.021	-0.030	-0.123
22	0.123	0.065	-0.009	-0.035	0.157	0.107	0.057	-0.036
23	0.083	0.025	-0.049	-0.075	0.117	0.067	0.017	-0.076
25	0.155	0.097	0.024	-0.002	0.189	0.140	0.089	-0.004
26	0.214	0.156	0.083	0.057	0.248	0.199	0.148	0.055
27	0.111	0.053	-0.020	-0.046	0.145	0.096	0.045	-0.048
28	0.183	0.125	0.052	0.026	0.217	0.168	0.117	0.024
29	0.069	0.011	-0.062	-0.088	0.103	0.054	0.003	-0.090
30	0.165	0.107	0.033	0.007	0.199	0.149	0.099	0.005
31	0.195	0.137	0.064	0.038	0.229	0.180	0.129	0.036
36	0.061	0.003	-0.071	-0.097	0.095	0.045	-0.005	-0.099

**TABLE A.2b** Table of  $\Delta_{a,b}(\Gamma, 4k)$  for the GaAs(100)-c(4x4) system. The “difference of the differences”  $\Delta_{\Delta}^{a,b}(\Gamma, 4k) = (\delta_a(\Gamma, 4k) - \delta_b(\Gamma, 4k))$  for a given set of adatom positions  $a$  and  $b$  is found at the  $a$ th row and  $b$ th column.  $\Delta_{\Delta}^{a,b}(\Gamma, 4k)$  is given in eV. A quick glance at this table indicates that convergence has not been reached using a  $\Gamma$ -point Brillouin zone integration. In light of this data, we performed all of our calculations using a 4 special  $k$ -points. See figure 4.1 to find the  $x$ - $y$  positions in the unit cell to which these labels refer). This table is continued from the previous page.

	20	21	22	23	25	26	27	28
2	-0.137	-0.017	-0.103	-0.063	-0.136	-0.195	-0.092	-0.164
3	0.031	0.150	0.064	0.104	0.031	-0.028	0.076	0.003
4	-0.151	-0.032	-0.118	-0.078	-0.151	-0.210	-0.106	-0.179
5	0.170	0.289	0.203	0.243	0.170	0.111	0.215	0.142
7	-0.133	-0.014	-0.100	-0.060	-0.133	-0.192	-0.088	-0.161
8	-0.088	0.032	-0.055	-0.015	-0.087	-0.146	-0.043	-0.115
10	-0.142	-0.023	-0.109	-0.069	-0.141	-0.201	-0.097	-0.170
11	-0.024	0.096	0.010	0.050	-0.023	-0.082	0.021	-0.051
12	-0.156	-0.036	-0.123	-0.083	-0.155	-0.214	-0.111	-0.183
13	-0.098	0.021	-0.065	-0.025	-0.097	-0.156	-0.053	-0.125
14	-0.024	0.095	0.009	0.049	-0.024	-0.083	0.020	-0.052
15	0.001	0.121	0.035	0.075	0.002	-0.057	0.046	-0.026
16	-0.190	-0.070	-0.157	-0.117	-0.189	-0.248	-0.145	-0.217
17	-0.141	-0.021	-0.107	-0.067	-0.140	-0.199	-0.096	-0.168
18	-0.090	0.030	-0.057	-0.017	-0.089	-0.148	-0.045	-0.117
19	0.003	0.123	0.036	0.076	0.004	-0.055	0.048	-0.024
20	0.000	0.119	0.033	0.073	0.001	-0.059	0.045	-0.027
21	-0.119	0.000	-0.086	-0.046	-0.119	-0.178	-0.075	-0.147
22	-0.033	0.086	0.000	0.040	-0.033	-0.092	0.012	-0.061
23	-0.073	0.046	-0.040	0.000	-0.073	-0.132	-0.028	-0.101
25	-0.001	0.119	0.033	0.073	0.000	-0.059	0.044	-0.028
26	0.059	0.178	0.092	0.132	0.059	0.000	0.103	0.031
27	-0.045	0.075	-0.012	0.028	-0.044	-0.103	0.000	-0.072
28	0.027	0.147	0.061	0.101	0.028	-0.031	0.072	0.000
29	-0.087	0.033	-0.054	-0.014	-0.086	-0.145	-0.042	-0.114
30	0.009	0.128	0.042	0.082	0.009	-0.050	0.054	-0.019
31	0.039	0.159	0.073	0.113	0.040	-0.019	0.084	0.012
36	-0.095	0.024	-0.062	-0.022	-0.095	-0.154	-0.050	-0.123

**TABLE A.2c** Table of  $\Delta_{a,b}(\Gamma, 4k)$  for the GaAs(100)-c(4x4) system. The “difference of the differences”  $\Delta_{\Delta}^{a,b}(\Gamma, 4k) = (\delta_a(\Gamma, 4k) - \delta_b(\Gamma, 4k))$  for a given set of adatom positions  $a$  and  $b$  is found at the  $a$ th row and  $b$ th column.  $\Delta_{\Delta}^{a,b}(\Gamma, 4k)$  is given in eV. A quick glance at this table indicates that convergence has not been reached using a  $\Gamma$ -point Brillouin zone integration. In light of this data, we performed all of our calculations using a 4 special k-points. See figure 4.1 to find the x-y positions in the unit cell to which these labels refer). This table is continued from the previous page.

	29	30	31	32	33	34	35	36
2	-0.050	-0.145	-0.176					-0.041
3	0.118	0.022	-0.009					0.126
4	-0.064	-0.160	-0.191					-0.056
5	0.257	0.161	0.130					0.265
7	-0.047	-0.142	-0.173					-0.038
8	-0.001	-0.097	-0.127					0.007
10	-0.055	-0.151	-0.182					-0.047
11	0.063	-0.032	-0.063					0.072
12	-0.069	-0.165	-0.195					-0.061
13	-0.011	-0.107	-0.137					-0.003
14	0.062	-0.033	-0.064					0.071
15	0.088	-0.007	-0.038					0.097
16	-0.103	-0.199	-0.229					-0.095
17	-0.054	-0.149	-0.180					-0.045
18	-0.003	-0.099	-0.129					0.005
19	0.090	-0.005	-0.036					0.099
20	0.087	-0.009	-0.039					0.095
21	-0.033	-0.128	-0.159					-0.024
22	0.054	-0.042	-0.073					0.062
23	0.014	-0.082	-0.113					0.022
25	0.086	-0.009	-0.040					0.095
26	0.145	0.050	0.019					0.154
27	0.042	-0.054	-0.084					0.050
28	0.114	0.019	-0.012					0.123
29	0.000	-0.096	-0.126					0.008
30	0.096	0.000	-0.031					0.104
31	0.126	0.031	0.000					0.135
32								
33								
34								
35								
36	-0.008	-0.104	-0.135					0.000

**TABLE A.2d** Table of  $\Delta_{a,b}(\Gamma, 4k)$  for the GaAs(100)-c(4x4) system. The “difference of the differences”  $\Delta_{\Delta}^{a,b}(\Gamma, 4k) = (\delta_a(\Gamma, 4k) - \delta_b(\Gamma, 4k))$  for a given set of adatom positions  $a$  and  $b$  is found at the  $a$ th row and  $b$ th column.  $\Delta_{\Delta}^{a,b}(\Gamma, 4k)$  is given in eV. A quick glance at this table indicates that convergence has not been reached using a  $\Gamma$ -point Brillouin zone integration. In light of this data, we performed all of our calculations using a 4 special k-points. See figure 4.1 to find the x-y positions in the unit cell to which these labels refer). This table is continued from the previous page.

# adatom position	$E_{total}$ (7Ry - $\Gamma$ ) (Hartrees)	$= E_{surf.}$ (7Ry - 4k) (Hartrees)	$+ E_{adatom}$ (7Ry - 16k) (Hartrees)	$E_{7Ry-4k} - E_{7Ry-16k}$ Difference (eV)
29	-243.58019	-243.64602	-243.65420	0.218
30	-243.58838	-243.65052	-243.65840	0.214

**TABLE A.3** The total energies of the {GaAs(100)-c(4x4) + Ga adatom} system for Brillouin zone integration schemes using  $\Gamma$ -point, 4 special k-points, and 16 special k-points. The same atomic positions were used for the data points at 4 k-points and 16 k-points. The difference  $\delta_a(4k, 16k)$  is shown in the column on the extreme right. The “difference of the differences”

$$\Delta_{\Delta}^{a=29,b=30}(4k, 16k) = (\delta_{a=29}(4k, 16k) - \delta_{b=30}(4k, 16k)) = 0.004 \text{ eV},$$

indicating excellent convergence. See figure 4.1 to find the x-y positions in the unit cell to which these labels refer.

# adatom position	$E_{total} = E_{surf.} + E_{adatom}$ (10Ry - $\Gamma$ ) (Hartrees)	(20Ry - $\Gamma$ ) (Hartrees)	$E_{5E_H} - E_{10E_H}$ Difference (eV)
2	-243.97313	-244.08184	2.958
3	-243.97520	-244.08418	2.966
4	-243.95036	-244.05938	2.967
5	-243.99853	-244.10801	2.979
7	-243.95962	-244.06877	2.970
9	-243.95924	-244.06841	2.971
10	-243.95725	-244.06658	2.975
11	-243.96949	-244.07867	2.971
12	-243.93373	-244.04255	2.961
13	-243.94213	-244.05096	2.961
14	-243.96839	-244.07713	2.959
15	-243.98048	-244.08959	2.969
16	-243.94376	-244.05266	2.963
17	-243.95032	-244.05944	2.969
18	-243.95959	-244.06875	2.970
19	-243.96796	-244.07703	2.968
20	-243.97360	-244.08263	2.967
23	-243.95005	-244.05907	2.967
29	-243.96220	-244.07113	2.964
30	-243.97086	-244.07956	2.958
31	-243.97389	-244.08259	2.958
32	-243.94598	-244.05493	2.965
33	-243.96377	-244.07269	2.964

**TABLE A.4** Raw data for the GaAs(100)-c(4x4) system at plane wave cutoffs of 5 and 10 Hartrees. This data was calculated using  $\Gamma$ -point sampling of the Brillouin zone. The first column is the adatom position label (see figure 4.1 to find the x-y positions in the unit cell to which these labels refer). The second column is the total energy calculated using a plane wave cutoff of 5 Hartrees. The third column is the total energy calculated using a plane wave cutoff of 10 Hartrees. The final column is the difference  $\delta_a(5, 10)$  of the energies between the 5 Hartree and 10 Hartree calculations (see the beginning of this appendix for an explanation of the notation). An analysis this data appears in tables A.4a, A.4b, A.4c.



	2	3	4	5	7	9	10	11
2	0.000	0.007	0.008	0.021	0.012	0.013	0.017	0.013
3	-0.007	0.000	0.001	0.014	0.005	0.005	0.010	0.005
4	-0.008	-0.001	0.000	0.013	0.004	0.004	0.008	0.004
5	-0.021	-0.014	-0.013	0.000	-0.009	-0.008	-0.004	-0.008
7	-0.012	-0.005	-0.004	0.009	0.000	0.001	0.005	0.001
9	-0.013	-0.005	-0.004	0.008	-0.001	0.000	0.004	0.000
10	-0.017	-0.010	-0.008	0.004	-0.005	-0.004	0.000	-0.004
11	-0.013	-0.005	-0.004	0.008	-0.001	-0.000	0.004	0.000
12	-0.003	0.004	0.005	0.018	0.009	0.010	0.014	0.010
13	-0.003	0.004	0.005	0.018	0.009	0.009	0.014	0.010
14	-0.001	0.007	0.008	0.020	0.011	0.012	0.016	0.012
15	-0.011	-0.004	-0.002	0.010	0.001	0.002	0.006	0.002
16	-0.005	0.002	0.003	0.016	0.007	0.007	0.012	0.008
17	-0.011	-0.004	-0.003	0.010	0.001	0.001	0.006	0.002
18	-0.012	-0.005	-0.004	0.009	-0.000	0.000	0.005	0.001
19	-0.010	-0.002	-0.001	0.011	0.002	0.003	0.007	0.003
20	-0.009	-0.001	-0.000	0.012	0.003	0.004	0.008	0.004
23	-0.008	-0.001	0.000	0.013	0.004	0.004	0.008	0.004
29	-0.006	0.001	0.002	0.015	0.006	0.007	0.011	0.007
30	0.000	0.008	0.009	0.021	0.012	0.013	0.017	0.013
31	0.000	0.008	0.009	0.021	0.012	0.013	0.017	0.013
32	-0.007	0.001	0.002	0.014	0.005	0.006	0.010	0.006
33	-0.006	0.002	0.003	0.015	0.006	0.007	0.011	0.007

**TABLE A.5a** Table of the “difference of the differences”  $\Delta_{a,b}(5E_H, 10E_H)$  in units of eV for the {GaAs(100)-c(4x4) + Ga adatom} system. The “difference of the differences”  $\Delta_{\Delta}^{a,b}(5E_H, 10E_H) = (\delta_a(5E_H, 10E_H) - \delta_b(5E_H, 10E_H))$  for a given set of adatom positions  $a$  and  $b$  is found at the  $a$ th row and  $b$ th column.  $\Delta_{\Delta}^{a,b}(5E_H, 10E_H)$  is given in eV. A quick glance at this table indicates that convergence has been reached using 5 Hartrees. In light of this data, we performed all of our calculations using a plane wave cutoff of 5 Hartrees. See figure 4.1 to find the x-y positions in the unit cell to which these labels refer). This table is continued on the next page.

	12	13	14	15	16	17	18	19
2	0.003	0.003	0.001	0.011	0.005	0.011	0.012	0.010
3	-0.004	-0.004	-0.007	0.004	-0.002	0.004	0.005	0.002
4	-0.005	-0.005	-0.008	0.002	-0.003	0.003	0.004	0.001
5	-0.018	-0.018	-0.020	-0.010	-0.016	-0.010	-0.009	-0.011
7	-0.009	-0.009	-0.011	-0.001	-0.007	-0.001	0.000	-0.002
9	-0.010	-0.009	-0.012	-0.002	-0.007	-0.001	-0.000	-0.003
10	-0.014	-0.014	-0.016	-0.006	-0.012	-0.006	-0.005	-0.007
11	-0.010	-0.010	-0.012	-0.002	-0.008	-0.002	-0.001	-0.003
12	0.000	0.000	-0.002	0.008	0.002	0.008	0.009	0.007
13	-0.000	0.000	-0.002	0.008	0.002	0.008	0.009	0.007
14	0.002	0.002	0.000	0.010	0.004	0.010	0.011	0.009
15	-0.008	-0.008	-0.010	0.000	-0.006	0.000	0.001	-0.001
16	-0.002	-0.002	-0.004	0.006	0.000	0.006	0.007	0.005
17	-0.008	-0.008	-0.010	-0.000	-0.006	0.000	0.001	-0.001
18	-0.009	-0.009	-0.011	-0.001	-0.007	-0.001	0.000	-0.002
19	-0.007	-0.007	-0.009	0.001	-0.005	0.001	0.002	0.000
20	-0.006	-0.005	-0.008	0.002	-0.004	0.002	0.004	0.001
23	-0.005	-0.005	-0.008	0.002	-0.003	0.003	0.004	0.001
29	-0.003	-0.003	-0.005	0.005	-0.001	0.005	0.006	0.004
30	0.003	0.004	0.001	0.011	0.005	0.011	0.013	0.010
31	0.003	0.004	0.001	0.011	0.005	0.011	0.013	0.010
32	-0.004	-0.003	-0.006	0.004	-0.001	0.005	0.006	0.003
33	-0.003	-0.002	-0.005	0.005	-0.001	0.005	0.007	0.004

**TABLE A.5b** Table of the “difference of the differences”  $\Delta_{a,b}(5E_H, 10E_H)$  in units of eV for the  $\{\text{GaAs}(100)\text{-c}(4\times 4) + \text{Ga adatom}\}$  system. The “difference of the differences”  $\Delta_{\Delta}^{a,b}(5E_H, 10E_H) = (\delta_a(5E_H, 10E_H) - \delta_b(5E_H, 10E_H))$  for a given set of adatom positions  $a$  and  $b$  is found at the  $a$ th row and  $b$ th column.  $\Delta_{\Delta}^{a,b}(5E_H, 10E_H)$  is given in eV. A quick glance at this table indicates that convergence has been reached using 5 Hartrees. In light of this data, we performed all of our calculations using a plane wave cutoff of 5 Hartrees. See figure 4.1 to find the x-y positions in the unit cell to which these labels refer). This table is continued from the previous page.

	20	23	29	30	31	32	33
2	0.009	0.008	0.006	-0.000	-0.000	0.007	0.006
3	0.001	0.001	-0.001	-0.008	-0.008	-0.001	-0.002
4	0.000	0.000	-0.002	-0.009	-0.009	-0.002	-0.003
5	-0.012	-0.013	-0.015	-0.021	-0.021	-0.014	-0.015
7	-0.003	-0.004	-0.006	-0.012	-0.012	-0.005	-0.006
9	-0.004	-0.004	-0.007	-0.013	-0.013	-0.006	-0.007
10	-0.008	-0.008	-0.011	-0.017	-0.017	-0.010	-0.011
11	-0.004	-0.004	-0.007	-0.013	-0.013	-0.006	-0.007
12	0.006	0.005	0.003	-0.003	-0.003	0.004	0.003
13	0.005	0.005	0.003	-0.004	-0.004	0.003	0.002
14	0.008	0.008	0.005	-0.001	-0.001	0.006	0.005
15	-0.002	-0.002	-0.005	-0.011	-0.011	-0.004	-0.005
16	0.004	0.003	0.001	-0.005	-0.005	0.001	0.001
17	-0.002	-0.003	-0.005	-0.011	-0.011	-0.005	-0.005
18	-0.004	-0.004	-0.006	-0.013	-0.013	-0.006	-0.007
19	-0.001	-0.001	-0.004	-0.010	-0.010	-0.003	-0.004
20	0.000	-0.000	-0.003	-0.009	-0.009	-0.002	-0.003
23	0.000	0.000	-0.002	-0.009	-0.009	-0.002	-0.003
29	0.003	0.002	0.000	-0.006	-0.006	0.001	-0.000
30	0.009	0.009	0.006	0.000	0.000	0.007	0.006
31	0.009	0.009	0.006	0.000	0.000	0.007	0.006
32	0.002	0.002	-0.001	-0.007	-0.007	0.000	-0.001
33	0.003	0.003	0.000	-0.006	-0.006	0.001	0.000

**TABLE A.5c** Table of the “difference of the differences”  $\Delta_{a,b}(5E_H, 10E_H)$  in units of eV for the {GaAs(100)-c(4x4) + Ga adatom} system. The “difference of the differences”  $\Delta_{\Delta}^{a,b}(5E_H, 10E_H) = (\delta_a(5E_H, 10E_H) - \delta_b(5E_H, 10E_H))$  for a given set of adatom positions  $a$  and  $b$  is found at the  $a$ th row and  $b$ th column.  $\Delta_{\Delta}^{a,b}(5E_H, 10E_H)$  is given in eV. A quick glance at this table indicates that convergence has been reached using 5 Hartrees. In light of this data, we performed all of our calculations using a plane wave cutoff of 5 Hartrees. See figure 4.1 to find the x-y positions in the unit cell to which these labels refer). This table is continued from the previous page.

# adatom position	$E_{total} = E_{surf.} + E_{adatom}$ (10Ry - 4k) (Hartrees)	(20Ry - 4k) (Hartrees)	$E_{10Ry-4k} - E_{20Ry-4k}$ Difference (eV)
3	-244.02584	-244.13197	2.888
7	-244.01629	-244.12258	2.892

**TABLE A.6** Raw data for the GaAs(100)-c(4x4) system at plane wave cutoffs of 5 and 10 Hartrees. This data was calculated using 4 k-point sampling of the Brillouin zone. The first column is the adatom position label (see figure 4.1 to find the x-y positions in the unit cell to which these labels refer). The second column is the total energy calculated using a plane wave cutoff of 5 Hartrees. The third column is the total energy calculated using a plane wave cutoff of 10 Hartrees. The final column is the difference  $\delta_a(5, 10)$  of the energies between the 5 Hartree and 10 Hartree calculations (see the beginning of this appendix for an explanation of the notation). the “difference of the differences”  $\Delta_{\Delta}^{a=3, b=7}(5E_H, 10E_H) = (\delta_{a=3}(5E_H, 10E_H) - \delta_{b=7}(5E_H, 10E_H))$  is just 0.004 eV, indicating convergence has been reached.

# adatom position	$E_{total} = E_{surf.} + E_{adatom}$ (10Ry - 4k) (18 $a_o$ ) (Hartrees)	(10Ry - 4k) (13 $a_o$ ) (Hartrees)	$E_{18a_o} - E_{13a_o}$ Difference (eV)
29	-244.01716	-244.01681	0.010
30	-244.02231	-244.02154	0.021

**TABLE A.7** Raw data for the GaAs(100)-c(4x4) system for vacuum interface thicknesses of 13  $a_o$  and 18  $a_o$ . This data was calculated using 4 k-point sampling of the Brillouin zone and a plane wave cutoff of 5 Hartrees. The first column is the adatom position label (see figure 4.1 to find the x-y positions in the unit cell to which these labels refer). The second column is the total energy calculated using a vacuum interface thickness of 18  $a_o$ . The second column is the total energy calculated using a vacuum interface thickness of 13  $a_o$ . The final column is the difference  $\delta_a(13 a_o, 18 a_o)$  of the energies between the 13  $a_o$  and 18  $a_o$  calculations (see the beginning of this appendix for an explanation of the notation). the “difference of the differences”  $\Delta_{\Delta}^{a=29,b=30}(13 a_o, 18 a_o) = (\delta_{a=29}(13 a_o, 18 a_o) - \delta_{b=30}(13 a_o, 18 a_o))$  is just 0.011 eV, indicating convergence has been reached. Despite this convergence, we performed all calculations, except some of the convergence tests, using a vacuum interface thickness of 18  $a_o$ .

# adatom position	$E_{total} = E_{surf.} + E_{adatom}$ (7Ry - $\Gamma$ ) (4 layers) (Hartrees)	(7Ry - $\Gamma$ ) (8 layers) (Hartrees)	$E_{4layers} - E_{8layers}$ Difference (Hartrees)
29	-244.58019	-385.05244	140.47225
30	-244.58838	-385.06048	140.47210

**TABLE A.8** Raw data for the GaAs(100)-c(4x4) system for different slab thicknesses. The thinner slab (the one used for most of the calculations in this study) consisted of a terminating GaAs(001)-c(2x2) reconstruction, four “bulk” layers, and a dimer layer of As. The thicker slab had eight “bulk” layers. This data was calculated using  $\Gamma$  point sampling of the Brillouin zone and a plane wave cutoff of 3.5 Hartrees (7 Rydbergs). The first column is the adatom position label (see figure 4.1 to find the x-y positions in the unit cell to which these labels refer). The second column is the total energy calculated using the thin slab. The second column is the total energy calculated using the thick slab. The final column is the difference  $\delta_a(4layer, 8layer)$  of the energies between the thin slab and thick slab calculations (see the beginning of this appendix for an explanation of the notation). The “difference of the differences”  $\Delta_{\Delta}^{a=29, a=30}(4layer, 8layer) = (\delta_{a=29}(4layer, 8layer) - \delta_{b=30}(4layer, 8layer))$  is just 0.00015 Hartrees = 4.08 meV, indicating convergence has been reached.

## **BIBLIOGRAPHY**

1. J. Tersoff and D.R. Hamann, *Phys. Rev. B*, **31**, 805 (1985).
2. P.E. Blöchl, *Phys. Rev. B*, **50**, 17953 (1994).
3. G.B. Bachelet, D.R. Hamann and M. Schlüter, *Phys. Rev. B*, **26**, 4199 (1982).
4. E. Wimmer, H. Krakauer, M. Weinert, A. J. Freeman, *Phys. Rev. B*, **24**, 864 (1981).
5. D. R. Hamann, L. F. Mattheiss, H. S. Greenside, *Phys. Rev. B*, **24**, 6151 (1981).
6. R. Car and M. Parrinello, *Phys. Rev. Lett.* **55** 2741 (1985).
7. D. Remler and P. Madden, *Mol. Physics*, **70**, 921 (1990).
8. R.O. Jones and O. Gunnarsson, *Reviews of Mod. Phys.*, **61**, 689 (1989).
9. D.M. Ceperley and B.J. Alder, *Phys. Rev. Lett.*, **45**, 566 (1980).
10. J.P. Perdew and A. Zunger, *Phys. Rev. B*, **23**, 5048 (1981).
11. G. Brocks, P.J. Kelly and R. Car, *Phys. Rev. Lett.*, **66**, 1729 (1991).
12. Kenji Shiraishi, *Appl. Phys. Lett.*, **60**, 1363 (1992).
13. K. Shiraishi, T. Ito and T. Ohno, *Sol. State Electr.*, **37**, 601 (1994).
14. A. Madhukar and S.V. Ghaisis, *CRC Crit. Rev. in Solid State and Mat. Sci.*, **14**, 1 (1986).
15. A. J. Fisher and P. Blöchl, *Phys. Rev. Lett.*, **70**, 3263 (1993).
16. P. Margl, K. Schwarz, and P. E. Blöchl, *J. Chem. Phys.*, **100**, 8617 (1994).
17. T. Irisawa, Y. Arima and T. Kuroda, *J. Crystal Growth*, **99**, 491 (1990).
18. J.M. McCoy and J.P. LaFemina, *Phys. Rev. B*, **50**, 17127 (1994).
19. Private communication from Donald Dorsey, Wright Laboratory.
20. Private communication from Mebarek Alouani, The Ohio State University.
21. S. Yu. Savrasov and D. Yu. Savrasov, *Phys. Rev. B*, **46**, 12181 (1992) and references therein.
22. M.C. Payne, M.P. Teter, D.C. Allan, T.A. Arias and J.D. Joannopoulos, *Reviews of Mod. Phys.*, **64**, 1045 (1992).
23. G. Pastore, E. Smargiassi and F. Buda, *Phys. Rev. A*, **44**, 6334 (1991).
24. L. Kleinman and D.M. Bylander, *Phys. Rev. Lett.*, **48**, 1425 (1982).

25. O.K. Andersen, O. Jepsen and D. Glötzel, in Highlights of Condensed Matter Theory, editors: F. Bassani, F. Fumi, and M. Tosi, North Holland 1985, p.59
26. Private communication from Peter Blöchl, IBM, Zürich.
27. M.D. Pashley, Phys. Rev. B, **40**, 10481 (1989).
28. John P. LaFemina, Surface science reports, **16**, 138 (1992).
29. Kenji Shiraishi, Appl. Phys. Lett., **39**, 3455 (1990).
30. E. Kaxiras, Y. Bar-Yam, J.D. Joannopoulos and K.C. Pandey, Phys. Rev. B. **35**, 9636 (1987).
31. S. Froyen, J.E. Bernard, R. Osório and A. Zunger, Physica Scripta, **T45**, 272 (1992).
32. D.J. Chadi, J. Vac. Sci. Technol. A, **5**, 834 (1987).
33. Private communication from Sverre Froyen, National Renewable Energy Lab.
34. D.K. Biegelsen, R.D. Bringans, J.E. Northrup and L.-E. Swartz, Phys. Rev. B, **41**, 5701 (1990).
35. J.E. Northrup and S. Froyen, Phys. Rev. Lett., **71**, 2276 (1993).
36. A.C. Warren, J.M. Woodall, P.D. Kirchner, X. Yin, F. Pollak, M.R. Melloch, N. Otsuka and K. Mahalingam, Phys. Rev. B, **46**, 4617 (1992).
37. M.R. Melloch, D.C. Miller and B. Das, Appl. Phys. Lett., **54**, 943 (1989).
38. D.K. Biegelsen, R.D. Bringans, J.E. Northrup and L.-E. Swartz, Phys. Rev. Lett., **65**, 452 (1990).
39. J. Bardeen, Phys. Rev. Lett. **6**, 57 (1961).
40. R.M. Feenstra, J. A. Stroscio, and A.P. Fein, Surf. Sci. **181**, 295 (1987).
41. A.H. MacDonald, S.H. Vosko and P.T. Coleridge, J. Phys. C, **12**, 2991 (1979).
42. S.N. Molotkov, S.S. Nazin, I.S. Smirnova and V.V. Tatarskii, Surface Science, **259**, 339 (1991).
43. S.L. Adler, Phys. Rev. **126**, 413 (1962).
44. N. Wiser, Phys. Rev. **129**, 62 (1963).
45. M. Alouani and J.M. Wills, Phys. Rev. B **54**, 2480 (1996).
46. D.E. Aspnes and A.A. Studna, Phys. Rev. B **27**, 985 (1983).
47. Private communication from A. Zunger, National Renewable Energy Lab.
48. Private communication from Kurt Einyk, Wright Laboratory.
49. Masaru Tsukada, Katsuyoshi Kobayashi, Nobuyuki Isshiki and Hiroyuki Kageshima, Surface Science Reports, **13**, 265 (1991).



50. M.D. Pashley and D. Li, *Mater. Sci. and Eng. B*, **30**, 73 (1995).
51. J.P. Pelz, *Phys. Rev. B*, **43**, 6746 (1991).
52. G. Doyen, D. Drakova and M. Scheffler, *Phys. Rev. B*, **47**, 9778 (1993).
53. H. Kim and J.R. Chelikowsky, U. Minnesota Supercomputer Institute Research Report, UMSI 96/107 (1996).
54. J.P. Pelz and R.H. Koch, *Phys. Rev. B*, **42**, 3761 (1990).
55. D.M. Bird, L.J. Clarke, R.D. King-Smith, M.C. Payne, I. Štich and A.P. Sutton, *Phys. Rev. Lett.*, **69**, 3785 (1992).
56. A. De Vita, I. Štich, M.J. Gillan, M.C. Payne and L.J. Clarke, *Phys. Rev. Lett.*, **71**, 1276 (1993).
57. Guo-Xin Qian and D.J. Chadi, *Phys. Rev. B*, **35**, 1288 (1986).
58. J.E. Northrup, *Phys. Rev. B*, **47**, 10032 (1993).
59. T. Yasuda, L. Mantese, U. Rossow and D.E. Aspnes, *Phys. Rev. Lett.*, **74**, 3431 (1995).
60. K. Laasonen, A. Pasquarello, R. Car, Changyol Lee, D. Vanderbilt, *Phys. Rev. B*, **47**, 10142 (1993).
61. N.A.W. Holzwarth, G.E. Matthews, R.B. Dunning, A.R. Tacket and Y. Zeng, *Phys. Rev. B*, in press.
62. S.-F. Ren and Y.-C. Chang, *Phys. Rev. B*, **44**, 13573 (1991).
63. D.J. Singh, H. Krakauer, C. Haas and A.Y. Liu, *Phys. Rev. B*, **46**, 13065 (1992).
64. D.J. Chadi, C. Tanner and J. Ihm, *Surface Science*, **120**, L425-L430 (1982).
65. B.W. Liang and C.W. Tu, *J. Appl. Phys.*, **72**, 2806 (1992).
66. C. Godreche, *J. Magn. Magn. Mat.*, **29**, 262 (1982).
67. I.A. Abrikosov and H.L. Skriver, *Phys. Rev. B*, **47**, 16532 (1993).
68. H.L. Skriver and N.M. Rosengaard, *Phys. Rev. B*, **43**, 9538 (1991).
69. M. Methfessel and M. Scheffler, *Physica B*, **172**, 175 (1991).
70. M. Methfessel and M. van Schilfgaarde, *Phys. Rev. B*, **48**, 4937 (1993).
71. R.W. Godby, M. Schlüter and L.J. Sham, *Phys. Rev. B*, **37**, 10159 (1988).
72. O. Gunnarsson and B.I. Lundqvist, *Phys. Rev. B*, **13**, 4274 (1976).
73. P.A. Sterne and J.C. Inkson, *J. Phys. C*, **17**, 1497 (1984).
74. J.E. Northrup and S. Froyen, *Phys. Rev. B*, **50**, 2015 (1994).

75. Guo-Xin Qian, R.M. Martin and D.J. Chadi, *Phys. Rev. Lett.*, **60**, 1962 (1988).
76. M.S. Hybertsen and S.G. Louie, *Phys. Rev. Lett.*, **55**, 1418 (1985).
77. H. Jorke, H.-J. Herzog and H. Kibbel, *Phys. Rev. B*, **40**, 2005 (1989).
78. Takahisa Ohno, *Phys. Rev. Lett.*, **70**, 631 (1993).
79. W.G. Schmidt and G.P. Srivastava, *Sol. State Commun.*, **89**, 345 (1994).
80. G.P. Srivastava, *Phys. Rev. B*, **47**, 16616 (1993).
81. M. Kaminska, E.R. Weber, Z. Liliental-Weber and R. Leon, *J. Vac. Sci. Technol. B*, **7**, 710 (1989).
82. A.N. Alekseev, S.Yu. Karpov, V.E. Myachin, Yu.V. Pogorel'skii, I.Yu. Rusanovich, I.A. Sokolov and G.A. Fokin, *Phys. Sol. State*, **36**, 1232 (1993).
83. Guo-Xin Qian, R.M. Martin and D.J. Chadi, *Phys. Rev. B*, **38**, 7649 (1988).
84. M.P. Teter, M.C. Payne and D.C. Allan, *Phys. Rev. B*, **40**, 12255 (1989).
85. I. Štich, R. Car, M. Parrinello and S. Baroni, *Phys. Rev. B*, **39**, 4997 (1989).
86. C.M. Wijers, G.P.M. Poppe, P.L. de Boeij, H.G. Bekker and D.J. Wentink, *Thin Solid Films*, **233**, 29 (1993).
87. M. Alouani and J.M. Wills, *Phys. Rev. B*, **54**, 2480 (1996).
88. R. Del Sole, *Sol. State Comm.*, **37**, 537 (1981).
89. A. Selloni, P. Marsella and R. Del Sole, **33**, 8885 (1986).
90. A.I. Shkrebtii and R. Del Sole, *Phys. Rev. Lett.*, **70**, 2645 (1993).
91. J.D.E. McIntyre and D.E. Aspnes, *Surface Science*, **24**, 417 (1971).
92. A. Kahn, *Surface Science*, **299**, 469 (1994).
93. D.J. Chadi, *Phys. Rev. B*, **19**, 2074 (1979).
94. E. Kaxiras, K.C. Pandey, Y. Bar-Yam and J.D. Joannopoulos, *Phys. Rev. Lett.*, **56**, 2819 (1986).
95. E. Kaxiras, Y. Bar-Yam, J.D. Joannopoulos and K.C. Pandey, *Phys. Rev. Lett.*, **57**, 106 (1986).
96. P.E. Blöchl, O. Jepsen and O.K. Andersen, *Phys. Rev. B*, **49**, 16223 (1994).